McKelvey School of Engineering Theses & Dissertations

McKelvey School of Engineering

Winter 12-15-2018

Basis Vector Model Method for Proton Stopping Power Estimation using Dual-Energy Computed Tomography

Shuangyue Zhang
Washington University in St. Louis

WASHINGTON UNIVERSITY IN ST. LOUIS

School of Engineering and Applied Science

Department of Electrical & Systems Engineering

Dissertation Examination Committee:
Joseph A. O'Sullivan, Chair
Mark A. Anastasio
R. Martin Arthur
David G. Politte
Tianyu Zhao

Basis Vector Model Method for Proton Stopping Power Estimation using Dual-Energy

Computed Tomography

by

Shuangyue Zhang

A dissertation presented to
The Graduate School
of Washington University in
partial fulfillment of the
requirements for the degree
of Doctor of Philosophy

December 2018
Saint Louis, Missouri

Contents

List of Figures

vi

List of Tables

Acknowledgments

First of all, my deepest thanks go to my parents, Caikun Zhang and Ningyu Yao, and my fiancé, Zhen Ren, for every reason and for no reason.

I would like to thank my advisor, Dr. Joseph A. O'Sullivan, for his guidance over these past years. His knowledge, experience, and insight helped and inspired me a lot during my doctoral research. I would also like to express my great thanks to his trust and appreciation of my work.

I would like to thank my committee members, Dr. Mark A. Anastasio, Dr. R. Martin Arthur, Dr. David G. Politte, and Dr. Tianyu Zhao, for their time and suggestions that help me improve this work.

I would like to thank my collaborators, Dr. Dong Han, Dr. Ruirui Liu, Dr. David G. Politte, Dr. Tianyu Zhao, Dr. Bruce R. Whiting, and Dr. Jeffrey F. Williamson, for their support during the research project.

I would like to thank my labmates and friends, including but not limit to Jingwei Lu, Linyun He, Dr. Mianzhi Wang, Zhenqi Lu, Yijian Xiang, Hui Wang, Dr. Soysal Degirmenci, Dr. Ayan Mitra, Dr. Jianyong Jiang, Dr. Homayoon Ranjbar, Tao Ge, Maria J. Medrano, and Tyler B. Webb, for their helpful ideas and suggestions for my study.

Shuangyue Zhang

Washington University in Saint Louis

December 2018

Dedicated to my parents and my fiancé.

ABSTRACT OF THE DISSERTATION

Basis Vector Model Method for Proton Stopping Power Estimation using Dual-Energy

Computed Tomography

by

Shuangyue Zhang

Doctor of Philosophy in Electrical Engineering

Washington University in St. Louis, 2018

Professor Joseph A. O'Sullivan, Chair

Accurate estimation of the proton stopping power ratio (SPR) is important for treatment planning and dose prediction for proton beam therapy. The state-of-the-art clinical practice for estimating patient-specific SPR distributions is the stoichiometric calibration method using single-energy computed tomography (SECT) images, which in principle may introduce large intrinsic uncertainties into estimation results. One major factor that limits the performance of SECT-based methods is the Hounsfield unit (HU) degeneracy in the presence of tissue composition variations. Dual-energy computed tomography (DECT) has shown the potential of reducing uncertainties in proton SPR prediction via scanning the patient with two different source energy spectra. Numerous methods have been studied to estimate the SPR by dual-energy CT DECT techniques using either image-domain or sinogram-domain decomposition approaches.

In this work, we implement and evaluate a novel DECT approach for proton SPR mapping, which integrates image reconstruction and material characterization using a joint statistical image reconstruction (JSIR) method based on a linear basis vector model (BVM). This method reconstructs two images of material parameters simultaneously from the DECT measurement data and then uses them to predict the electron densities and the mean excitation energies, which are required by the Bethe equation for computing proton SPR.

The proposed JSIR-BVM method is first compared with image-domain and sinogram-domain decomposition approaches based on three available SPR models including the BVM in a well controlled simulation framework that is representative of major uncertainty sources existing in practice. The intrinsic SPR modeling accuracy of the three DECT-SPR models is validated via theoretical computed radiological quantities for various reference human tissues. The achievable performances of the investigated methods in the presence of image formation uncertainties are evaluated using synthetic DECT transmission sinograms of virtual cylindrical phantoms and virtual patients, which consist of reference human tissues with known densities and compositions. The JSIR-BVM method is then experimentally commissioned using the DECT measurement data acquired on a Philips Brilliance Big Bore CT scanner at $90\,\mathrm{kVp}$ and $140\,\mathrm{kVp}$ for two phantoms of different sizes, each of which contains 12 different soft and bony tissue surrogates. An image-domain decomposition method that utilizes the two HU images reconstructed via the scanner's software is implemented for comparison.

The JSIR-BVM method outperforms the other investigated methods in both the simulation and experimental settings. Although all investigated DECT-SPR models support low intrinsic modeling errors (i.e., less than 0.2% RMS errors for reference human tissues), the achievable accuracy of the image- and sinogram-domain methods is limited by the image formation uncertainties introduced by the reconstruction and decomposition processes. In contrast, by taking advantage of an accurate polychromatic CT data model and a joint

DECT statistical reconstruction algorithm, the JSIR-BVM method accounts for both systematic bias and random noise in the acquired DECT measurement data. Therefore, the JSIR-BVM method achieves much better accuracy and precision on proton SPR estimation compared to the image- and sinogram-domain methods for various materials and object sizes, with an overall RMS-of-mean error of 0.4% and a maximum absolute-mean error of 0.7% for test samples in the experimental setting. The JSIR-BVM method also reduces the pixel-wise random variation by 4-fold to 6-fold within homogeneous regions compared to the image- and sinogram-domain methods while exhibiting relatively higher spatial resolution. The results suggest that the JSIR-BVM method has the potential for better SPR prediction in clinical settings.

Chapter 1

Introduction

1.1 Motivation

The clinical effectiveness of proton-beam therapy has been demonstrated in several treatment sites due to its highly conformal dose distributions [1–7]. To realize the full potential of proton therapy, the range of the proton beam needs to be accurately determined. However, in current clinical practice, a safety margin of $2 - 3.5\%$ of the proton range, which converts into $2 - 7$ mm according to the depth of the treatment site, is added to the distal boundary of the clinical target volume (CTV) in order to ensure CTV coverage due to the proton range uncertainties [8–10], limiting dose-sparing of surrounding healthy tissue. One of the dominant sources of proton range uncertainty is the limited accuracy with which proton stopping power ratios (SPRs) along the beam path are estimated using the state-of-the-art single-energy computed tomography (SECT) method [11–13].

Dual-energy computed tomography (DECT) techniques have been shown to have the potential to achieve much better accuracy and robustness for SPR estimation compared to the SECT stoichiometric calibration method [11, 14–25]. By scanning the patient with two

different x-ray spectra, DECT approaches are able to extract two independent material properties from the CT measurements in order to more accurately resolve the variations of tissue density and tissue composition. These DECT-SPR models are theoretically highly accurate. However, most currently proposed DECT methods are based on the two separately reconstructed SECT images, i.e., those from the scanner's default reconstruction process. Random noise and systematic errors in the separately reconstructed CT images may cause the accuracy of SPR estimates to deteriorate in the clinical setting [13, 21, 26].

The dual-energy joint statistical image reconstruction (JSIR) approach, which depends on a physically realistic signal formation model and an effective statistical reconstruction algorithm, has the potential to reconstruct more quantitatively accurate and artifact-free images and therefore to improve the proton SPR estimation accuracy.

1.2 Background

1.2.1 X-ray computed tomography (CT)

The x-ray CT technique uses an external x-ray source to image the anatomy and characterize tissue inside the patient's body. There exist various specifications of CT systems for different applications. In this dissertation, we focus on the fan-beam, energy-integrating whole-body CT scanners.

The x-ray beam from the source is collimated into a fan shape that expands within the XY-plane and forms a very thin layer in the Z-direction. A detector array is placed on the opposite side to measure the survival probability of x-ray photons penetrating the scanned object. The source and detector array rotate around the iso-center in the XY-plane to acquire
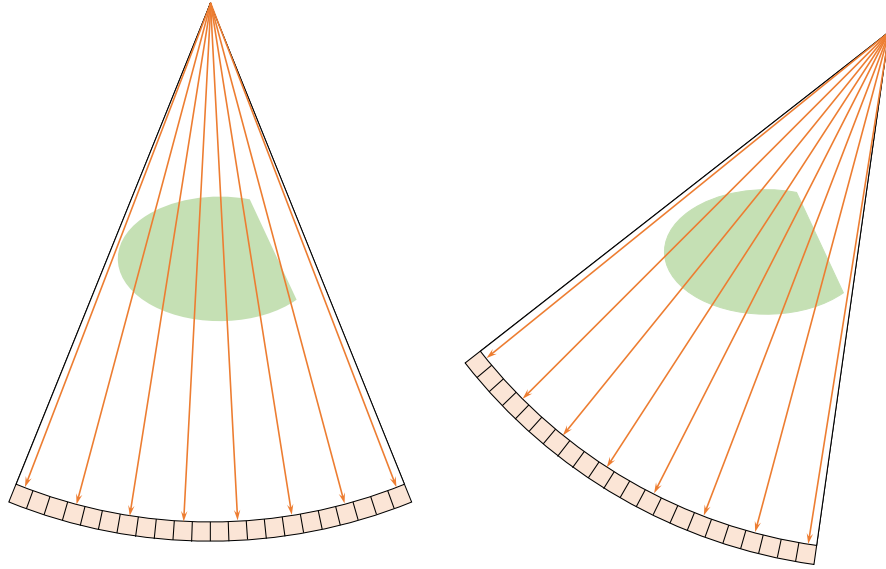
Figure 1.1: Illustration of single-slice CT data acquisition.

data from gantry angles (i.e., views) uniformly spaced on the circle. The acquired data, called a sinogram, is indexed by the gantry angle and detector index. Figure 1.1 illustrates the fan-beam geometry (single-slice, 3rd generation scanner) at two different gantry angles.

For a 3D volume, the data acquisition can be performed in either axial or helical mode. In the axial mode, the patient bed remains at a fixed position during a full rotation of data acquisition and then moves to a new position in the Z-direction. In the helical mode, the patient bed continuously moves along the Z-direction while the gantry is rotating. Modern CT scanners usually have multiple detector rows, which enables acquisition of multiple slices simultaneously.

Data formation

When an x-ray beam penetrates through a homogeneous medium, the survival probability of x-ray photons at a given energy E follows Beer's law,

$$\frac{\Phi_{\text{out}}(E)}{\Phi_{\text{in}}(E)} = \exp\left(-l\,\mu(E)\right), \tag{1.1}$$

where $\Phi_{\text{in}}(E)$ and $\Phi_{\text{out}}(E)$ are the counts of incident photons and survived photons, respectively, $\mu(E)$ is the photon linear attenuation coefficient of the medium, and l is the length of the x-ray beam passing through the medium.

The x-ray photons emitted from the tube are polychromatic with a peak energy E_{max}. Figure 1.2 shows typical incident x-ray spectra $\Phi_0(E)$ of an x-ray source with a tungsten target for different peak energies.

Within the typical energy range of patient CT scanners, the photons with lower energies are more likely to be attenuated than those with higher energies. Therefore, the mean energy of the x-ray beam becomes larger when the beam passes through more medium, which is called the beam-hardening effect. Figure 1.3 shows the spectrum changes when penetrating different widths of water. The mean energy of the beam increases from $66.2\,\text{keV}$ to $78.8\,\text{keV}$ with the increased water filtration from $0\,\text{mm}$ to $300\,\text{mm}$, respectively.

In conventional fan-beam CT scanners, the source spectra are generally beam path-dependent because the fan beams are pre-balanced by a compensation filter, which is usually bow-tie shaped, placed between the source and the scanned patients in order to reduce the required
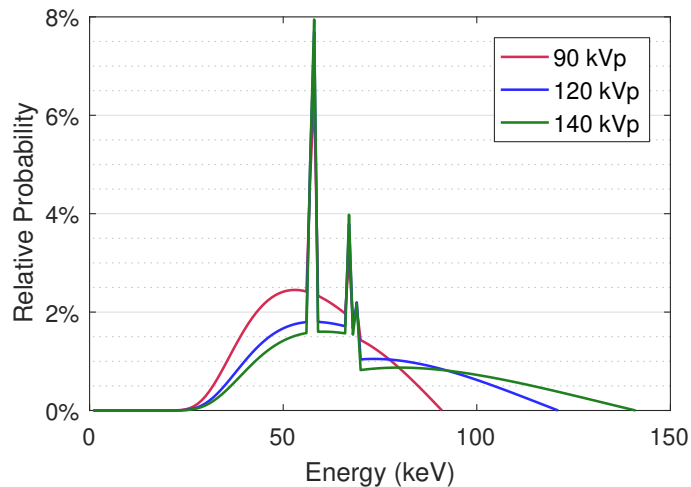
Figure 1.2: Normalized incident x-ray source spectra of a typical x-ray tube with a tungsten target, which is expressed by the fractions of photon counts as a function of photon energy.
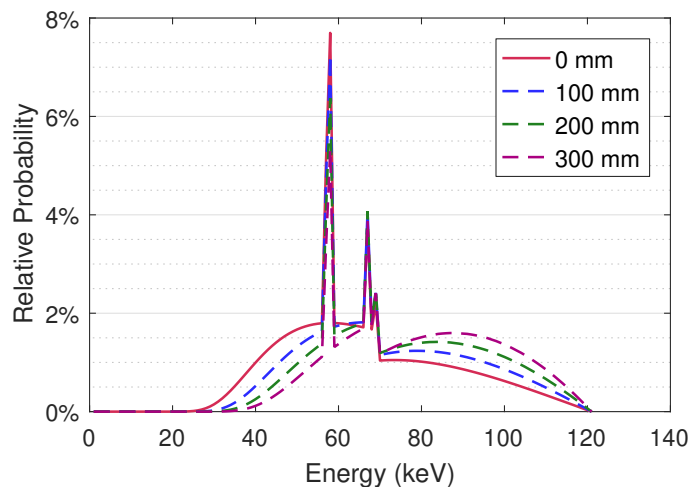
Figure 1.3: Normalized 120 kVp spectra (photon counts) after penetrating water with different thicknesses.

dynamic range of the detectors. The down-stream source spectrum is mathematically formulated as

$$\Phi(y, E) = \Phi_0(E) \exp\left(-l_{\mathrm{F}}(y)\,\mu_{\mathrm{F}}(E)\right), \tag{1.2}$$

where y is the index of the ray path (i.e., source-detector pair), $\mu_{\mathrm{F}}(E)$ is the attenuation coefficient of the filter material, and $l_{\mathrm{F}}(y)$ is the filter thickness corresponding to the ray path y.

In modern CT scanners, the detectors can be energy-integrating or photon-counting. Most clinical scanners are equipped with energy-integrating detectors, which measure the total energy flux of received photons over the whole spectrum. The ideal air-normalized transmission signal of a given path y penetrating through an object (i.e., the measured signal of an object relative to that of air-scan) is modeled as

$$\left[\frac{I_d}{I_0}\right](y) = \frac{\int_E \Phi(y, E) D(E) \exp\left(-\int_y \mu(\mathbf{r}, E)\,\mathrm{d}\mathbf{r}\right)\mathrm{d}E}{\int_E \Phi(y, E) D(E)\,\mathrm{d}E}, \tag{1.3}$$

where $D(E)$ is the detector-response function and $\mu(\mathbf{r}, E)$ is the photon linear attenuation coefficient at spatial location $\mathbf{r}$. Thus, $\int_y \mu(\mathbf{r}, E)\,\mathrm{d}\mathbf{r}$ represents the integral of the attenuation coefficients along the ray path y, which is called the line integral or projection data.

By defining the normalized energy-fluence spectrum as

$$\Psi(y, E) = \frac{\Phi(y, E) D(E)}{\int_{E'} \Phi(y, E') D(E')\,\mathrm{d}E'}, \tag{1.4}$$

the transmission signal is rewritten as

$$\left[\frac{I_d}{I_0}\right](y) = \int_E \Psi(y, E) \exp\left(-\int_y \mu(\mathbf{r}, E)\,\mathrm{d}\mathbf{r}\right)\mathrm{d}E. \tag{1.5}$$

For computational purposes, the data model is discretized as

$$\left[\frac{I_d}{I_0}\right](y) = \sum_E \Psi(y, E) \exp\left(-\sum_x h(y|x)\mu(x, E)\right) ,$$ (1.6)

where x is the index of discretized image pixel,[1] E is now an index of a discretized energy spectrum,[2] $\mu(x, E)$ is the photon linear attenuation coefficient at image pixel x and energy E, and $h(y|x)$ is the point-spread function of the scanner system that represents the effective length of the intersection between the ray path y and image pixel x.[3]

Image reconstruction

In most conventional single-energy CT reconstruction approaches, the concept of effective energy, $\bar{E}$, is employed to simplify the inverse problem. A pre-reconstruction process called the beam-hardening correction, which attempts to transform the acquired polychromatic sinogram into an equivalent monochromatic sinogram at the effective energy, is applied before image reconstruction. Mathematically, we write

$$\exp\left(-\sum_x h(y|x)\mu(x, \bar{E})\right) \approx \mathcal{BH}\left(\left[\frac{I_d}{I_0}\right](y)\right) ,$$ (1.7)

---

[1]The image space is discretized into pixels in the 2D case and voxels in the 3D case. Without loss of generality, throughout this dissertation we describe all problems in 2D.

[2]Throughout this dissertation, the photon energy E is discretized at $1\,\mathrm{keV}$ intervals. The maximum energy $E_{\max}$ is determined by the tube potential and the minimum energy $E_{\min}$ is set to $20\,\mathrm{keV}$.

[3]In this dissertation, the computation of system matrix is done with the object-constrained computed tomography (OCCT) software package developed by Dr. David G. Politte at Washington University School of Medicine.

where $\mathcal{BH}(\cdot)$ is the operator of the beam-hardening correction.[4] Therefore,

$$\sum_{x} h(y|x)\mu(x,\bar{E}) \approx -\ln\left(\mathcal{BH}\left(\left[\frac{I_d}{I_0}\right](y)\right)\right). \tag{1.8}$$

Analytical reconstruction methods, including the filtered back-projection (FBP) algorithm that is widely used for 2D applications, solve the linear inverse problem (1.8), i.e.,

$$\mu(x,\bar{E}) \approx \langle\mu\rangle(x) = \mathcal{FBP}\left(-\ln\left(\mathcal{BH}\left(\left[\frac{\mathbf{I}_d}{\mathbf{I}_0}\right]\right)\right)\right), \tag{1.9}$$

where $\mathcal{FBP}(\cdot)$ is the FBP operator and $\langle\mu\rangle(x)$ is the reconstructed spectrally-averaged attenuation coefficient, which is assumed to be an approximation of $\mu(x,\bar{E})$.

The reconstructed image is further re-scaled into CT numbers in Hounsfiled units (HU),

$$\mathrm{HU}(x) = 1000\frac{\langle\mu\rangle(x)}{\mu_{\mathrm{w}}(\bar{E})} - 1000. \tag{1.10}$$

where $\mu_{\mathrm{w}}(\bar{E})$ is the linear attenuation coefficient of water at the effective energy. Therefore, in the ideal case $\mathrm{HU} = 0$ for water and $\mathrm{HU} = -1000$ for air.

---

[4]In practice, the beam-hardening correction operation is more commonly applied to the attenuation data, $-\ln\left(\left[\mathbf{I}_d/\mathbf{I}_0\right]\right)$, rather than the transmission data, $\left[\mathbf{I}_d/\mathbf{I}_0\right]$. However, the two representations $-\ln\left(\mathcal{BH}\left(\left[\mathbf{I}_d/\mathbf{I}_0\right]\right)\right)$ and $\mathcal{BH}^*\left(-\ln\left(\left[\mathbf{I}_d/\mathbf{I}_0\right]\right)\right)$ are mathematically transferable. In this dissertation, we choose the first way because some reconstruction algorithms operate on the corrected transmission data.

Beam-hardening artifact

The single-energy CT image reconstruction discussed above is based on the monochromatic assumption, i.e., the beam-hardening correction transforms the raw data into a monochromatic projection. One of the most commonly used methods is the water-based beam-hardening correction that builds a one-to-one look-up-table or polynomial function between the measured polychromatic attenuation and the corrected monochromatic attenuation based on water attenuation [27–30]. The water-based methods are in principle based on the assumption that all scanned subjects are water equivalent with varying densities. Thus, residual errors are presented in the reconstructed images if the scanned object deviates from water. Additional bone-based correction, which is based upon prior assumptions about the bone compositions, has been used to further remove bone-introduced artifacts [31–33]. However, in principle, the beam-hardening correction is not able to achieve the "true" monochromatic projection for a heterogeneous object that is composed of various media.

It is well known that the residual beam-hardening effect may cause cupping artifacts and streak artifacts in the reconstructed images. Besides the visible artifacts, the residual beam-hardening effect also causes size- and location-dependence of the reconstructed HUs, especially for those media with relatively high atomic numbers (e.g., bones). The HU non-uniformity is an inherent issue for most single-energy CT reconstructions.

Advanced image reconstruction

Besides the most widely used FBP algorithm, more advanced iterative reconstruction algorithms and statistical image reconstruction (SIR) algorithms have also been employed to solve the inverse problem, (1.7) or (1.8). In one common approach, SIR algorithms assume

the measurement data follow a known distribution parameterized by the ground truth signal and formulate the reconstruction problem as a maximum-likelihood estimation problem.

For energy integrating detectors used in clinical CT scanners, the signal statistics of energy integrating detectors theoretically follow a compound Poisson model, of which the modified Poisson model is an accurate approximation [34–36]. Several reconstruction algorithms have been proposed to minimize the negative Poisson log-likelihood function [36–42]. Another widely used approach is to minimize a weighted-least-squares cost function of the post-log data (i.e., attenuation data); the weighting may be derived from a series expansion of the Poisson log-likelihood function [43–46].

Additionally, due to the ill-conditioned nature of the reconstruction problem itself, regularization should be incorporated to achieve more physically feasible reconstruction results. Spatial penalty functions, which penalize the difference between image intensities of nearby pixels, are commonly used to enforce image smoothness.

These SIR algorithms tend to dramatically improve the signal-to-noise ratio (SNR) and image contrast as well as to reduce image artifacts. However, most proposed methods are based on the monochromatic assumption of the linearized data (i.e., the data after beam-hardening correction) and therefore do not handle the data modeling errors including residual beam-hardening effects.

1.2.2 Dual-energy x-ray CT

Dual-energy x-ray CT techniques scan the patient with two different x-ray spectra, which provides additional information about the properties of the tissue in the patient.

There are various technical approaches to implement dual-energy CT [47, 48]. Sequential scanning is the simplest way to acquire dual-energy data, which scans the patient twice using different tube potentials (i.e., kVp's). The dual-source technique uses two sets of sources and detector arrays that are arranged at an angular offset and operate at the same time to acquire two sets of independent data corresponding to different tube potentials. The fast kVp switching technique rapidly changes the tube potential between low- and high-energy levels on a view-by-view basis during the gantry rotation. Splitting beam and layered detectors are other ways to implement DECT scanning. These techniques can also be extended to multi-energy CT (or spectral CT), which acquires data for more than two energy spectra. Another way to implement multi-energy CT is the use of the energy-resolving photon-counting detector, which counts the received photons and measures the associated energy of each photon. The measurement data are commonly separated into several energy bins according to energy level.

Because two or more sets of data are acquired at different energies, the DECT (or multi-energy CT approach) is able to estimate two independent material parameters that are insensitive to the source spectra, instead of the spectrally-averaged attenuation coefficient. Thus, the DECT approach has the potential to provide more accurate material characterization than the SECT approach.

1.2.3 Proton beam radiotherapy

Proton beam radiotherapy uses beams of high energy protons to irradiate cancerous tissues. When a proton penetrates through media, the energy deposition generally increases when the energy of the proton decreases. Therefore, a proton deposits the maximum energy close the distal end of the beam path, which is known as the Bragg peak. In treatments, proton

beams with different initial energies are applied to form a spread-out Bragg peak (SOBP) in order to cover the entire treatment site.

In treatment planning and dose prediction, to determine the proton range (i.e., the position of the Bragg peak) inside the patient body for a given initial proton energy, it is required to know the proton stopping powers of media along the beam path. Proton stopping power is defined as the proton energy loss per unit distance traveled in the medium. Accurate estimation of proton stopping power is crucial for dose calculation and geometric targeting in proton therapy planning.

The ratio of proton stopping power of a medium to that of water, SPR, is commonly used in current clinical practice. The SPR is often assumed to be constant for different proton energies. The water equivalent path length (WEPL) of a given beam path inside the patient body is computed by integrating the SPR along the beam path.

In current clinical practice, patient-specific SPR information is obtained via the SECT sto-ichiometric calibration method that was proposed by Schneider *et al.* [49]. The parametric model of photon cross-section proposed by Rutherford *et al.* [50], which links the measured CT number and material parameters (i.e., density and composition), is first calibrated via scanning a tissue-surrogate phantom. The parametric model is given as

$$\frac{\mathrm{HU}}{1000} + 1 = \rho_e \left(K_{\mathrm{ph}} \tilde{Z}^{3.62} + K_{\mathrm{coh}} \breve{Z}^{1.86} + K_{\mathrm{KN}} \right), \tag{1.11}$$

where ρ_e is the electron density of the medium, $\tilde{Z}$ and $\breve{Z}$ are the effective atomic number of the medium defined by the Mayneord's equation (see (1.22) in Section 1.2.4) for $n = 3.62$ and $n = 1.86$, respectively. K_{ph}, K_{coh}, and K_{KN} are the calibration parameters that mainly characterize the cross-sections for photoelectric effect, coherent scattering, and incoherent

scattering, respectively, and are assumed to be constant for each different material under the same scan protocol.

After phantom calibration (i.e., solving the protocol-specific constants K_{ph}, K_{coh}, and K_{KN} via a phantom scan), the theoretical CT numbers of a series of reference human tissues are computed from the calibrated photon cross-section model. A piecewise linear calibration curve between CT number and proton SPR is then fit using the computed CT numbers and known SPRs of the reference human tissues. As an illustration, Figure 1.4 shows an example of the calibration curve for a 120 kVp CT scan protocol.[5]

The SECT method builds a one-to-one relationship between CT numbers and SPRs. Because there is only one measurement per image pixel, SECT analysis is unable to disambiguate the dependency of CT number on density and elemental composition [12,13]. Tissues with different SPRs may have very similar CT numbers under a given tube potential. The patient-specific tissue compositions and densities may deviate significantly from the reference ones recommended by the International Commission on Radiation Units and Measurement (ICRU) or the International Commission on Radiological Protection (ICRP) and therefore deviate from the stoichiometric calibration curve derived by the reference tissues [12]. To compensate for the proton range uncertainties due to the estimation uncertainties of SPR, safety margins of $2-3.5\%$ of the proton ranges are added to CTVs during treatment planning. Since the margin is a fraction of the total proton range, the uncertainties of the delivered dose distribution become larger when the treatment site is deeper inside the patient body.

---

[5]To derive the calibration curve shown in Figure 1.4, the measurement data of the Gammex RMI 467 phantom (Gammex, Middleton, WI) were simulated using the 120 kVp spectrum shown in Figure 1.2 and the FBP-reconstructed image was used to calibrate the parametric photon cross-section model. The same reference human tissues as in the original work by Schneider *et al.* [49] and similar segmentation of the CT number range (i.e., three linear fits for lung, various organs, and bony tissues, and two more line segments to account for the adipose tissue) were used for the curve fitting. Different reference tissues or criteria of CT number segmentation may be used in clinical practice.
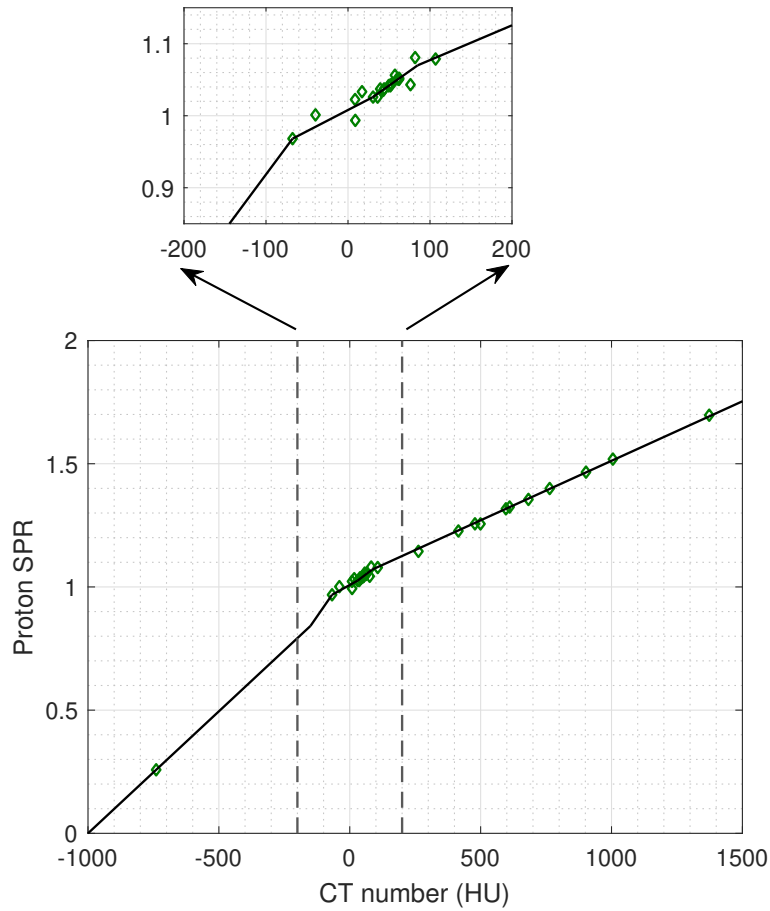
Figure 1.4: The SECT stoichiometric calibration curve for a 120 kVp CT scan protocol. The reference human tissues are indicated by the green diamonds.

One promising alternative methodology for more quantitative tissue characterization is the DECT technique. By acquiring two independent measurements under different source spectra, the DECT approaches are able to resolve the HU dependence on density and composition. More details of DECT-based SPR estimation methods are introduced in Chapter 2.

1.2.4 Derived radiological quantities

Proton stopping power

Within the energy range typically used in proton therapy (i.e., up to a few hundreds of MeV), the proton stopping power S_p at a given energy E_p can be approximated by the Bethe equation [51],

$$S_p(E_p) = -\frac{\mathrm{d}E_p}{\mathrm{d}x} = \rho_e \frac{k_0}{\beta^2} \left[\frac{1}{2} \ln \frac{2m_e c^2 \beta^2 T_{\mathrm{max}}}{I^2 (1 - \beta^2)} - \beta^2 - \frac{\delta(\beta)}{2} - \frac{C(\beta)}{Z} \right], \tag{1.12}$$

where k_0 is the product of physical constants, c is the speed of light, and

$$\beta = \frac{v_p}{c} = \sqrt{1 - \left(\frac{m_p c^2}{E_p + m_p c^2} \right)^2} \tag{1.13}$$

is the proton speed relative to that of light,

$$T_{\mathrm{max}} = \frac{2m_e c^2 \beta^2}{1 - \beta^2} \left(1 + 2\frac{m_e}{m_p} \frac{1}{\sqrt{1 - \beta^2}} + \left(\frac{m_e}{m_p} \right)^2 \right)^{-1} \tag{1.14}$$

is the maximum energy transferred from a proton to a single electron, m_e and m_p are the invariant mass of electron and proton, respectively, and ρ_e and I are the electron density and mean excitation energy of the medium, respectively.

In (1.12), the density correction $\delta(\beta)$ is significant only when the kinetic energy of the proton is of the same order as or larger than the rest energy of a proton. The shell correction $C(\beta)/Z$ is significant only when the proton velocity is comparable to that of atomic electrons. These two corrections were ignored in our implementation because they are negligible for the typical proton energies used in proton therapy [52]. Therefore, the proton stopping power is

calculated as

$$S_p(E_p) = \rho_e \frac{k_0}{\beta^2} \left[\frac{1}{2} \ln \frac{2m_e c^2 \beta^2 T_{\max}}{I^2(1-\beta^2)} - \beta^2 \right] , \qquad (1.15)$$

which can be equivalently rewritten as

$$S_p(E_p) = \rho_e k_1(E_p) \left[k_2(E_p) - \ln \left(I/\text{eV} \right) \right] , \qquad (1.16)$$

where $k_1(E_p)$ and $k_2(E_p)$ are functions of the proton energy, E_p, and do not change for different media.

The SPR is then computed as,

$$\frac{S_p}{S_{p,\text{w}}}(E_p) = \frac{\rho_e}{\rho_{e,\text{w}}} \cdot \frac{k_2(E_p) - \ln \left(I/\text{eV} \right)}{k_2(E_p) - \ln \left(I_\text{w}/\text{eV} \right)} , \qquad (1.17)$$

where $\rho_{e,\text{w}}$, I_w, and $S_{p,\text{w}}$ are the electron density, mean excitation energy, and proton stopping power of the reference water, respectively.

For all evaluations in this dissertation, E_p is set to 200 MeV, which results in

$$k_1(200\,\text{MeV}) = 1.5907 \times 10^{-24}\,\text{MeV cm}^3 ,$$

$$k_2(200\,\text{MeV}) = 12.76 .$$

In this dissertation, all reference SPRs are computed via the Bethe equation. Because the approximation error of the Bethe equation is independent of any CT-based approach as long as the reference SPR is computed via the Bethe equation, such approximation error is not discussed in this study.

Electron density

The electron density is defined as the number of electrons per unit volume. For a medium with known density and elemental composition, the electron density is computed by the atomic mixture rule as

$$\rho_e = \rho N_A \sum_k \omega_k \left(\frac{Z_k}{A_k} \right),$$

(1.18)

where ρ is the mass density of the medium, N_A is the Avogadro constant, and ω_k, Z_k, and A_k are the mass fraction, atomic number, and atomic weight of the k-th element in the medium, respectively. Moreover, for a given elemental composition, the electron-to-mass density ratio can be defined as

$$\frac{\rho_e}{\rho} = N_A \sum_k \omega_k \left(\frac{Z_k}{A_k} \right).$$

(1.19)

Mean excitation energy

The mean excitation energy (i.e., I-value) in the Bethe equation is a geometric average of the excitation energies of the medium weighted by the oscillator strengths. The accurate calculation of mean excitation energy is only achievable for simple atomic gases [53]. For compounds and mixtures, the reference value of the mean excitation energy is approximated by the Bragg additivity rule [53],

$$\ln I = \frac{\sum_k \omega_k \left(\frac{Z_k}{A_k} \right) \ln I_k}{\sum_k \omega_k \left(\frac{Z_k}{A_k} \right)},$$

(1.20)

where I_k is the mean excitation energy of the k-th element in the medium, including the ICRU-recommended solid/liquid phase to gaseous phase correction.

Similar to that of the Bethe equation, the approximatiion error of the Bragg additivity rule is not included in the scope of this dissertation.

Photon attenuation coefficient

For a medium with known density and elemental composition, the mass attenuation coefficients can be approximated by the atomic mixture rule as

$$\left(\frac{\boldsymbol{\mu}}{\rho}\right) = \sum_k \omega_k \left(\frac{\boldsymbol{\mu}}{\rho}\right)_k \tag{1.21}$$

where $\left(\boldsymbol{\mu}/\rho\right)_k$ is the mass attenuation coefficients of the k-th element in the medium.

All reference mass attenuation coefficients used in this dissertion are obtained from the National Institute of Standards and Technology (NIST) XCOM database [54] and the linear attenuation coefficients are then computed as $\boldsymbol{\mu} = \rho \left(\boldsymbol{\mu}/\rho\right)$.

Effective atomic number

The effective atomic number, Z_{eff} or Z^*, is a commonly used concept for modeling photon cross-sections. Various parametric fitting models have been proposed to model the energy-dependent photon linear attenuation coefficient as a function of effective atomic number and electron density, such as the Spiers model [55], the Alvarez-Macovski model [56], and the Torikoshi model [57].

A classical definition of Z_{eff} was first proposed by Mayneord [58] as

$$Z_{\text{eff}} = \left(\frac{\sum_k \omega_k \left(\frac{Z_k}{A_k} \right) Z_k{}^n}{\sum_k \omega_k \left(\frac{Z_k}{A_k} \right)} \right)^{\frac{1}{n}}, \tag{1.22}$$

where $n = 2.94$. Note that this model was originally derived for a particular $140\,\text{kVp}$ x-ray spectrum.

Modifications of Mayneord's equation with different n's, as well as other definitions of Z_{eff}, are also proposed in the literature.

The effective atomic number Z_{eff} does not have exact physical meaning, but can be considered as an indicator of the composition of the medium. It should be noted that Z_{eff} is an energy-dependent quantity for most ρ_e-Z_{eff} photon cross-section models [15, 59]. Therefore, the spectrally-averaged effective atomic number is considered in CT-based material characterization models.

1.3 Notation

This section summarizes the main notation that is used throughout this dissertation. Unless otherwise specified, a variable in non-italic, bold style denotes the column vector that corresponds to the scalar variable in italic, non-bold style.

E	Energy of an x-ray photon
E_p	Energy of a proton
μ	Photon linear attenuation coefficient

ρ	Mass density
ρ_e	Electron density
I	Mean excitation energy
Z	Atomic number
Z_{eff}	Effective atomic number
S_p	Proton stopping power
HU	CT number in Hounsfield units
u	Modified Hounsfield units, $u = \mathrm{HU}/1000 + 1$
i	Index of BVM basis, $i \in \{1, 2\}$
j	Index of scan energy, $j \in \{\mathrm{L}, \mathrm{H}\}$
x	Index of image pixels
y	Index of source-detector pairs (i.e., ray path)
$h(y\|x)$	An element of CT system matrix that represents the effective length of the intersection between the ray path y and image pixel x
Φ_0	Normalized x-ray CT source spectrum without bow-tie filter (up-stream)
Φ	Normalized x-ray CT source spectrum with bow-tie filter (down-stream)
Ψ	Normalized x-ray CT energy-fluence spectrum
D	Detector response function
I_d/I_0	Measured transmission sinogram relative to the air-scan
I_0	Unattenuated source intensity (i.e., air-scan)
d	Measured transmission sinogram

Q	Estimated/expected transmission sinogram
γ	Background event
c	BVM component weight
L	Projection (line integral) of BVM component weight

1.4 Contributions of the dissertation

The main contributions of this dissertation are as follows.

- Proposed a method for estimating SPR images from DECT measurement data. The method is built on a BVM for material characterization and a JSIR algorithm that integrates image reconstruction and material decomposition.

- Derived the mathematical model for mapping proton SPR of biological tissues and tissue-like materials from their photon linear attenuation coefficients.

- Investigated the reasons for the slow convergence of the alternating minimization (AM) algorithm for the joint DECT image reconstruction that is based on the polychromatic CT data model.

- Proposed acceleration strategies for the joint DECT image reconstruction problem, which achieves a convergence speed comparable to the SECT monochromatic image reconstruction.

- Evaluated the intrinsic modeling error of the BVM for predicting proton SPR from photon cross-section for both reference human tissues and tissues with reasonable composition variations.

- Evaluated the impact of several sources of data acquisition and image formation uncertainties on SPR estimation accuracy achievable by the proposed JSIR-BVM method as well as previously described image- and sinogram-decomposition approaches in a well-controlled simulation framework.

- Developed the pre-processing procedure of the raw data extracted from a specific commercial CT scanner and experimentally estimated the equivalent source spectra of the CT scanner in order to support the implementation of the proposed JSIR-BVM method in the clinical setting.

- Evaluated the accuracy of the proposed JSIR-BVM method on the commercial CT scanner via phantom study.

- Investigated the impact of the SPR modeling uncertainty and the DECT image formation uncertainty, which are the two major contributors to the overall SPR estimation uncertainty, in both a simulation and an experimental study.

1.5   Organization of the dissertation

Chapter 2 reviews the previously published DECT approaches for SPR estimation: the image-domain and sinogram-domain decomposition approaches. Different DECT-SPR models implemented in this dissertation are briefly summarized.

The framework of the proposed JSIR-BVM method for mapping DECT measurements into proton SPR is introduced in Chapter 3, including the mathematical modeling for material characterization and the image reconstruction problem. Chapter 4 discusses the implementation and improvement of the image reconstruction algorithm.

In Chapter 5, the proposed JSIR-BVM method is evaluated in a well-controlled simulation framework, which realistically models several major sources of uncertainties encountered in clinical practice. The proposed JSIR-BVM method is compared to existing image- and sinogram-domain decomposition methods. Different sources of estimation uncertainties are investigated in detail.

The proposed JSIR-BVM method is experimentally commissioned in Chapter 6 using raw DECT data exported from a commercial CT scanner. Two phantoms of different sizes containing tissue surrogates of known densities and elemental compositions were analyzed by the JSIR-BVM method and an image-domain decomposition method that is applied to the scanner-reconstructed CT images.

Chapter 2

DECT method for proton stopping power ratio (SPR) estimation

By employing the Bethe equation (1.15), the estimation of proton stopping power can be achieved by estimating electron density (ρ_e) and mean excitation energy (I-value). Several models have been proposed in the literature to link DECT image intensities with ρ_e and I-value [11, 14–21]. Most DECT-SPR models assume that I-value can be approximated by a function of effective atomic number, Z_{eff}, for a constrained set of materials such as those normally occurring human tissues. The two independent material properties, ρ_e and Z_{eff}, are extracted for each image pixel and then used to computed SPRs. Theoretically, these two-parameter DECT-SPR models are highly accurate with as low as 0.2% root-mean-square (RMS) errors for standard human tissues [13]. Other DECT-SPR models that do not require explicit estimation of ρ_e or Z_{eff} [22–25] have also been developed and show comparable theoretical accuracy. These methods either build a one-to-one relationship between proton SPRs and predicted electron densities [22,23,25], or directly fit a parametrical model between proton SPRs and DECT image intensities [24].

Most proposed DECT methods for SPR estimation are post-reconstruction, image-domain analyses of two separately reconstructed CT images acquired with different source spectra. These methods are easy to implement because one can directly use the scanner's SECT image reconstruction process. However, random noise as well as residual systematic errors in the separately reconstructed CT images (e.g., HU nonuniformity and dependence on patient size, which are due to residual beam-hardening and scatter artifacts) may cause the accuracy of SPR estimates derived from image-domain analyses to deteriorate in the clinical setting [13, 21, 26].

To compensate for the polychromatic nature of CT x-ray beams, several approaches for decomposing dual-energy and transmission sinograms into energy-invariant component projections before image reconstruction have been proposed [16, 25, 56, 60–65]. Joint decomposition and reconstruction techniques, which simultaneously reconstruct two energy-invariant component images, have also been investigated for dual-energy and multi-energy CT [17, 66–70]. However, only a few studies have adopted the sinogram-domain method for application of SPR estimation, while the potential of joint reconstruction techniques for SPR estimation has not yet been explored.

2.1 Image-domain decomposition approach

The image-domain decomposition approach uses two single-energy images that are reconstructed separately from acquired low- and high-energy CT measurements using a conventional SECT reconstruction algorithm (e.g., the FBP algorithm). In the SECT reconstruction, a beam-hardening correction process is applied to the acquired sinograms before reconstruction in order to transform the raw sinograms into approximately monochromatic ones. After image reconstruction, two material properties, which are commonly electron density

ρ_e and effective atomic number Z_{eff}, can be determined for each image pixel via a calibration model and then used for computing the SPR map.

In this dissertation, we investigated two of these image-domain decomposition methods in the literature.

2.1.1 Hünemohr method and Hünemohr-Saito method

The Alvarez-Macovski photon cross-section model [56] decomposes the energy-dependent photon linear attenuation coefficient of an known material within the typical photon energy range of x-ray CT scans into a virtual photoelectric absorption contribution and a virtual Compton scattering contribution as

$$\mu(E) = \rho_e \left(a_{\text{AM}} \frac{Z_{\text{eff}}^n}{E^3} + b_{\text{AM}} f_{\text{KN}}(E) \right) , \tag{2.1}$$

where $f_{\text{KN}}(E)$ is the Klein-Nishina formula. The two proportionality factors, a_{AM} and b_{AM}, are approximately material-independent.

In this model, the effective atomic number Z_{eff} is defined using a modified Mayneord's equation (1.22) with $n = 3.2$, which yields the best fit for the elemental attenuation coefficients within the range $Z = 2 - 20$ for our CT spectra.

Based on the Alvarez-Macovski model described above, Hünemohr *et al.* [71] developed the mathematical relationship between two spectrum-averaged CT numbers and the material

properties (i.e., ρ_e and Z_{eff}) as

$$\frac{\rho_e}{\rho_{e,\text{w}}} = \tilde{\alpha} u_{\text{L}} + (1 - \tilde{\alpha}) u_{\text{H}} \,, \tag{2.2}$$

$$\frac{Z_{\text{eff}}}{Z_{\text{eff,w}}} = \left[\left(\frac{\rho_e}{\rho_{e,\text{w}}} \right)^{-1} \left(\tilde{\beta} u_{\text{L}} + (1 - \tilde{\beta}) u_{\text{H}} \right) \right]^{\frac{1}{n}} \,, \tag{2.3}$$

where $\rho_{e,\text{w}}$ and $Z_{\text{eff,w}}$ are the electron density and effective atomic number of water, respectively, u_{L} and u_{H} are the modified HU of low- and high-energy CT images, respectively. The modified HU is defined as

$$u = \frac{\text{HU}}{1000} + 1 \,, \tag{2.4}$$

which is proportional to the spectrally-averaged attenuation coefficient.

The two calibration parameters, $\tilde{\alpha}$ and $\tilde{\beta}$, depend on the specific dual-energy scanning protocol and can be determined via scanning a single calibration material other than water. However, the performance relies on the choice of the calibration material [21].

Additionally, in the derivation of the Hünemohr method, the CT numbers for water and air are assumed to be exactly $0\,\text{HU}$ and $-1000\,\text{HU}$, respectively. However, in practice, their CT numbers may be slightly different from the ideal ones. To account for the inaccuracy of CT numbers and to improve the performance of the original Hünemohr method, Li *et al.* [21] adapted the Saito method for ρ_e estimation [26] and generalized the calibration model as

$$\frac{\rho_e}{\rho_{e,\text{w}}} = \tilde{\alpha}_1 \left(u_{\text{H}} + \tilde{\alpha}_0 \left(u_{\text{H}} - u_{\text{L}} \right) \right) + \tilde{\alpha}_2 \,, \tag{2.5}$$

$$\frac{Z_{\text{eff}}}{Z_{\text{eff,w}}} = \left[\left(\frac{\rho_e}{\rho_{e,\text{w}}} \right)^{-1} \left(\tilde{\beta}_1 \left(u_{\text{H}} + \tilde{\beta}_0 \left(u_{\text{H}} - u_{\text{L}} \right) \right) + \tilde{\beta}_2 \right) \right]^{\frac{1}{n}} \,. \tag{2.6}$$

The calibration parameters $\tilde{\alpha}_k$ and $\tilde{\beta}_k$ are determined via scanning a selected calibration phantom with tissue-substitutes of known densities and compositions.[1] The modified method was shown to achieve performance improvement in the original work by Li *et al.* [21] and in our experiments, while it achieves performance similar to the original Hünemohr method in idealized simulations. In this dissertation, the original Hünemohr method is used for simulations and is referred to as the *Hünemohr method*. The modified method is used for experiments and is referred to as the *Hünemohr-Saito method*.

When applying this method for proton stopping power estimation via the Bethe Equation, the I-value is inferred from Z_{eff} using the empirical linear-relationship that was first introduced by Yang *et al.* [11],

$$\ln I = a_Z Z_{\text{eff}} + b_Z \,, \tag{2.7}$$

where the parameters a_Z and b_Z are predetermined for different material groups with highly similar compositions, e.g., soft and bony tissues, separately. Figure 2.1 shows the linear-relationship for selected reference human tissues (see Appendix A). The I-value parameterization function is given by

$$\ln\left(I/\text{eV}\right) = \begin{cases} 0.1227\, Z_{\text{eff}} + 3.3909 & \text{for soft tissues,} \\ 0.0984\, Z_{\text{eff}} + 3.3607 & \text{for bony tissues.} \end{cases} \tag{2.8}$$

---

[1]Different calibration phantoms have been used in the literature for calibrating either the SECT stoichiometric calibration method or DECT-based methods. In this dissertation, the conventional Gammex RMI 467 phantom (Gammex, Middleton, WI), which contains 13 tissue surrogates, is used for all calibration purposes.
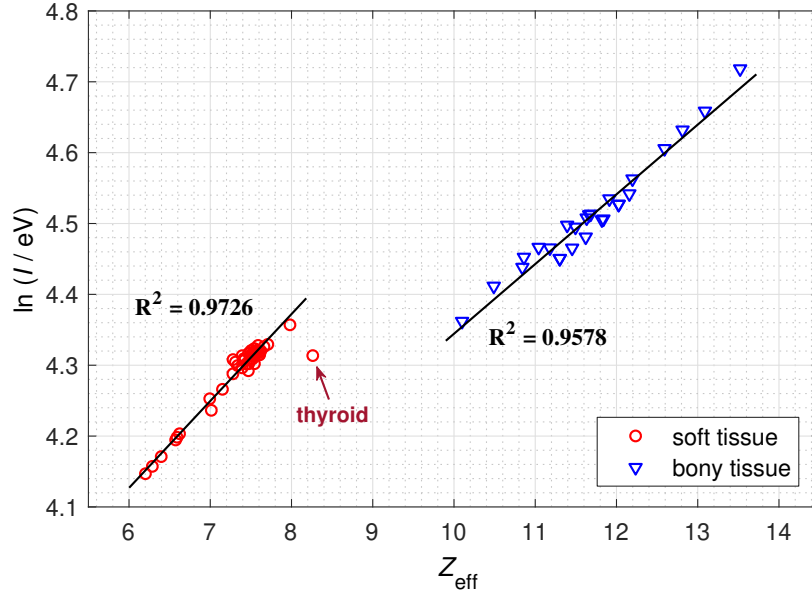
Figure 2.1: The linear fit between the logarithm of mean excitation energies and effective atomic number for reference human tissues, which is used as the I-value parameterization in the Hünemohr method.

2.1.2 Bourque method

Bourque *et al.* [15] developed a dual-energy stoichiometric calibration process to convert u_L and u_H into electron density and effective atomic number. In their method, spectrally-averaged electronic cross-sections are fit to a polynomial function of their atomic numbers Z as

$$\int \Psi_j(E)\sigma_{e,Z}(E)\,\mathrm{d}E = \langle\hat{\sigma}_e\rangle_j(Z) = \sum_{k=1}^{K} \breve{a}_{j,k} Z^{k-1}\,, j \in \{\mathrm{L},\mathrm{H}\}\,, \tag{2.9}$$

where $\Psi_j(E)$ is the known source spectra. Then, given a specific DECT scan protocol, the effective atomic number for an arbitrary mixture is defined as

$$Z_{\mathrm{eff},x} = \frac{1}{2}\left[\langle\hat{\sigma}_e\rangle_\mathrm{L}^{-1}\left(\int \Psi_\mathrm{L}(E)\sigma_{e,x}(E)\,\mathrm{d}E\right) + \langle\hat{\sigma}_e\rangle_\mathrm{H}^{-1}\left(\int \Psi_\mathrm{H}(E)\sigma_{e,x}(E)\,\mathrm{d}E\right)\right]\,. \tag{2.10}$$

The calibration model for converting DECT image intensities into material characteristics is given in the form of polynomial functions as

$$
Z_{\text{eff}} = \sum_{k=1}^{K} \breve{\beta}_k \left(\frac{u_{\text{L}} - u_{\text{H}}}{u_{\text{L}} + u_{\text{H}}} \right)^{(k-1)} , \tag{2.11}
$$

$$
\frac{\rho_e}{\rho_{e,\text{w}}} = \frac{u_{\text{L/H}}}{\sum_{m=1}^{M} \breve{\alpha}_{\text{L/H},m} Z_{\text{eff}}^{(m-1)}} , \tag{2.12}
$$

where $\breve{\beta}_k$, $\breve{\alpha}_{\text{L},m}$, and $\breve{\alpha}_{\text{H},m}$ are scan-specific parameters, which need to be determined from a calibration phantom scan just as in the Hünemohr-Saito method. Consistent with the original work, the orders of polynomial fitting are set to $K = M = 6$.

When applying this model for proton stoppinng power estimation, Z_{eff} is first calculated for each image location. Two separate estimates of ρ_e are calculated from images of low and high energies, respectively, and then averaged to obtain the final estimate of ρ_e. The I-value is parameterized as a piecewise polynomial function of Z_{eff} for the reference human tissue compositions (as shown in Figure 2.2). For the simulated spectra used in this dissertation (see Figure 5.1), the parameterization function is given by

$$
I/\text{eV} = \begin{cases} 13.50\, Z_{\text{eff}} - 21.18 & \text{for } Z_{\text{eff}} < 6.17 , \\[2mm] -0.006952\, Z_{\text{eff}}^5 + 0.3047\, Z_{\text{eff}}^4 - 4.833\, Z_{\text{eff}}^3 + 32.87\, Z_{\text{eff}}^2 - 75.96\, Z_{\text{eff}} + 35.39 \\[1mm] \qquad\qquad\qquad\qquad\qquad\qquad\qquad\qquad\qquad \text{for } 6.17 \leq Z_{\text{eff}} \leq 13.54 , \\[2mm] 12.82\, Z_{\text{eff}} - 61.75 & \text{for } Z_{\text{eff}} > 13.54 . \end{cases}
\tag{2.13}
$$
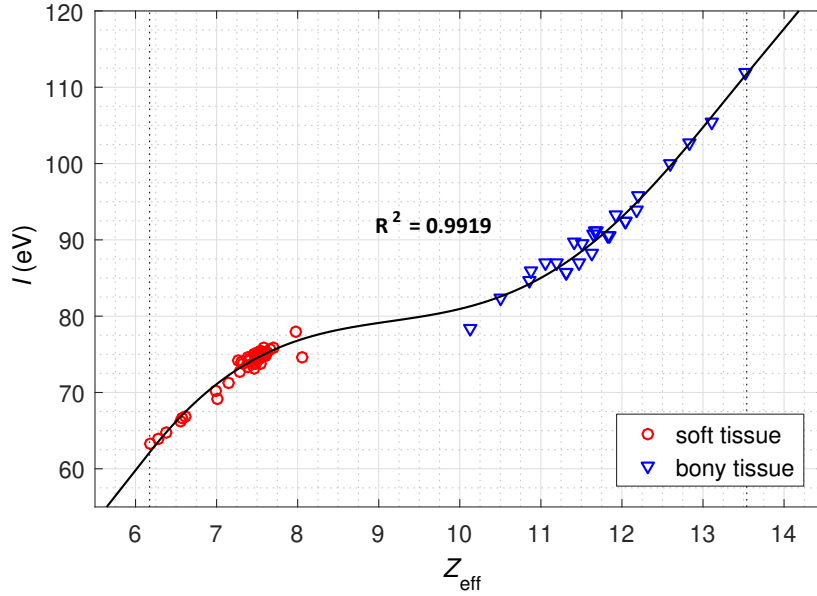
Figure 2.2: The polynomial fit between mean excitation energies and effective atomic number for the reference human tissues, which is used as the I-value parameterization in the Bourque method.

2.2 Sinogram-domain decomposition approach

The sinogram-domain decomposition approach attempts to extract two component line-integrals (i.e., projections) that are invariant to the spectra before the image reconstruction process. After the decomposition, the two corresponding component images are then reconstructed via the FBP algorithm.

Let $\Psi_j(y, E)$, $j \in \{L, H\}$ be the energy-fluence spectrum of the low- and high-energy scans for photon energy E and source-detector pair y, and $\left[\frac{I_d}{I_0}\right]_j(y)$ be the air-normalized transmission measurement. The measurement can be modeled as

$$\left[\frac{I_d}{I_0}\right]_j(y) = \sum_E \Psi_j(y, E) \exp\left(-\sum_x h(y|x)\mu(x, E)\right), \tag{2.14}$$

31

where $\mu(x, E)$ is the photon linear attenuation coefficient at image pixel x and photon energy E, and $h(y|x)$ is the point-spread function of the scanner system.

Consider a general linear decomposition model of the photon linear attenuation,

$$\mu(x, E) = \nu_1(x)\eta_1(E) + \nu_2(x)\eta_2(E) \,, \tag{2.15}$$

where $\eta_i(E)$ are two corresponding basis functions that are independent of materials and $\nu_i(x)$ are the two energy-invariant, material-specific basis coefficients. Note that the Alvarez-Macovski photon cross-section model (2.1) as well as the BVM, which will be introduced in Chapter 3, are two examples of the linear decomposition model. For the Alvarez-Macovski photon cross-section model, the two basis functions are defined as

$$\begin{cases} \eta_1(E) = a_{\text{AM}}\dfrac{1}{E^3} \,, \\ \eta_2(E) = b_{\text{AM}}f_{\text{KN}}(E) \,, \end{cases} \tag{2.16}$$

and the two corresponding material-specific parameters are defined as

$$\begin{cases} \nu_1(x) = \rho_e(x)\big[Z_{\text{eff}}(x)\big]^n \,, \\ \nu_2(x) = \rho_e(x) \,. \end{cases} \tag{2.17}$$

Therefore, ρ_e and Z_{eff} images can be uniquely determined once $\nu_i(x)$ are known and then be used to compute the proton stopping power for each image pixel [16].

Based on a selected decomposition model, two corresponding line integrals are defined as

$$L_{\nu,i}(y) = \sum_x h(y|x)\nu_i(x) \,, \tag{2.18}$$

implying that

$$\left[\frac{I_d}{I_0}\right]_j (y) = \sum_E \Psi_j(y, E) \exp\left(-L_{\nu,1}(y)\eta_1(E) - L_{\nu,2}(y)\eta_2(E)\right). \tag{2.19}$$

The two line integrals $L_{\nu,i}(y)$ can be numerically solved from (2.19) for each source-detector pair y independently with the known spectra $\Psi_j(y, E)$. Note that the beam-hardening correction is embedded in the poly-energetic sinogram decomposition. Thus, no separate beam-hardening correction is needed in this process.

After the decomposition, the two corresponding images of material-specific parameters, $\nu_i(x)$, can be obtained from $L_{\nu,i}(y)$ using any conventional SECT reconstruction algorithm, which is the FBP algorithm in our implementation.

On the other hand, the calibration-based image-domain ρ_e-Z_{eff} methods in Section 2.1 can also been extended into the sinogram-domain approach [16]. Once the two material parameters $\nu_i(x)$ are reconstructed, two monochromatic HU images can be computed via (2.15) for both the calibration phantom and the test object. The calibration-based ρ_e-Z_{eff} models can then be applied to the monochromatic HU images.

Chapter 3

Basis vector model (BVM) for DECT-based proton SPR estimation

The BVM was first investigated by Han *et al.* [52, 59, 72] to link photon cross-section and proton stopping power. In this chapter, we extend and improve their methodology and build the BVM-based framework for mapping proton stopping power from polychromatic DECT data.

3.1 BVM for photon linear attenuation coefficients

The BVM assumes that within the typical energy range of CT scans,[1] the energy-dependent linear attenuation coefficients of biological media can be approximated by linear combinations of those of two dissimilar basis materials, i.e.,

$$\mu(x, E) = c_1(x)\mu_1(E) + c_2(x)\mu_2(E) \,, \tag{3.1}$$

---

[1] For clinical whole-body scanners, the maximum photon energy $E_{\max}$ (i.e., the x-ray tube potential) is within the range from $70\,\mathrm{keV}$ to $150\,\mathrm{keV}$. The minimum photon energy $E_{\min}$ is set to $20\,\mathrm{keV}$ throughout this dissertation, because for all considered spectra, photons below $20\,\mathrm{keV}$ comprise less than 10^{-7} of the total source energy.

Table 3.1: Physical densities, electron densities, and elemental composition of the two basis materials.

Basis material	ρ (g/mL)	$\rho_e/\rho_{e,w}$	Elemental Mass Fraction (%)				
			H	C	O	Cl	Ca
Polystyrene	1.061	1.028	7.74	92.26			
23% CaCl$_2$ solution	1.221	1.186	8.62		68.38	14.69	8.31
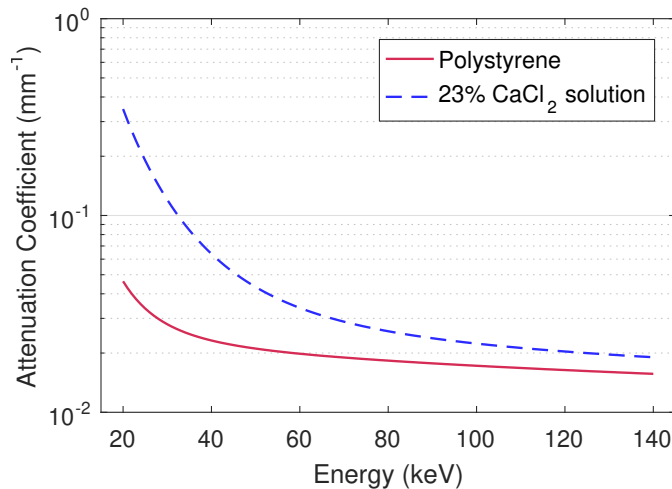
Figure 3.1: The linear attenuation coefficient curves of the two basis materials between 20 keV and 140 keV.

where $\mu_i(E)$ are the linear attenuation coefficients of the two basis materials at photon energy E and $c_i(x)$ are the corresponding *BVM component weights* for the unknown material at image location x. In this dissertation, polystyrene and CaCl$_2$ aqueous solution (23% by mass), which bracket the range of naturally occurring biological media, are used as the basis materials for all typical human tissues and tissue surrogates. Table 3.1 summarizes the physical properties of the two basis material. Figure 3.1 shows the linear attenuation coefficient curves of the two basis materials.

The selection of the basis materials was previously discussed in [73]. It was demonstrated that this model is able to parameterize linear attenuation coefficients with $1 - 2\%$ accuracy in an energy range from 20 keV to 1 MeV and in an effective atomic number range from 2

to 20. This model can also be used for estimating other radiological quantities including partial cross-sections, mass-energy absorption coefficients, and differential cross-sections. In this dissertation, we focus on applying this model for proton stopping power mapping from DECT data.

3.2 BVM for proton stopping power

To compute the proton stopping power map via the Bethe equation (1.15), the electron density ρ_e and mean excitation energy I are predicted for each pixel from two BVM component images reconstruced from DECT data. The electron density of a biological medium can be accurately estimated by the linear combination [52]:

$$\rho_e(x) = c_1(x)\rho_{e,1} + c_2(x)\rho_{e,2}\,, \tag{3.2}$$

where $\rho_{e,i}$ are the electron densities of the two basis materials. As an extension, this approximation can also be applied to non-biological, tissue-surrogate materials composed of elements similar to tissues.

On the other hand, I-value can not be directly determined from CT image intensities. Thus, a common way to estimate the I-value is to employ an empirical relationship between I-value and some quantity that is related to the elemental composition and can be determined from CT data (i.e., most commonly the effective atomic number Z_{eff} as shown in Figure 2.1 and Figure 2.2) [11, 15, 18, 71]. To adopt the BVM for proton stopping power estimation, we hypothesized that for a constrained group of materials with highly similar compositions, the

logarithm of the I-value closely follows a linear relationship with the weighted-component-ratio defined as

$$r_c(x) = \frac{c_1(x)\rho_{e,1}}{c_1(x)\rho_{e,1} + c_2(x)\rho_{e,2}} \,, \tag{3.3}$$

and the estimate of I-value is given as

$$I(x) = \exp\left(a_r r_c(x) + b_r\right), \tag{3.4}$$

where a_r and b_r are pre-determined fitting parameters.

The empirical I-value parameterization model is fit using reference human tissues (see Appendix A). The theoretical BVM component weights were computed via the spectrum-weighted least-squares fitting as described in Section 3.4, which ensures that the computed weights agree with those derived from idealized image reconstruction. As shown in Figure 3.2, there exists a good linear relationship between $\ln I$ and r_c for the reference human tissues. It can also be seen that the soft tissues and bony tissues follow different linear relationships due to the dissimilarity between their compositions, i.e., soft tissues are mostly composed of hydrogen, carbon, nitrogen, and oxygen, while bony tissues contain a large fraction of calcium and phosphorous.

The empirical parameterization function is generated separately for soft and bony tissues by finding the best linear fit for the reference tissues as

$$\ln\left(I/\mathrm{eV}\right) = \begin{cases} -1.3308\, r_c + 5.4525 & \text{for soft tissues,} \\ -0.3299\, r_c + 4.5228 & \text{for bony tissues,} \end{cases} \tag{3.5}$$
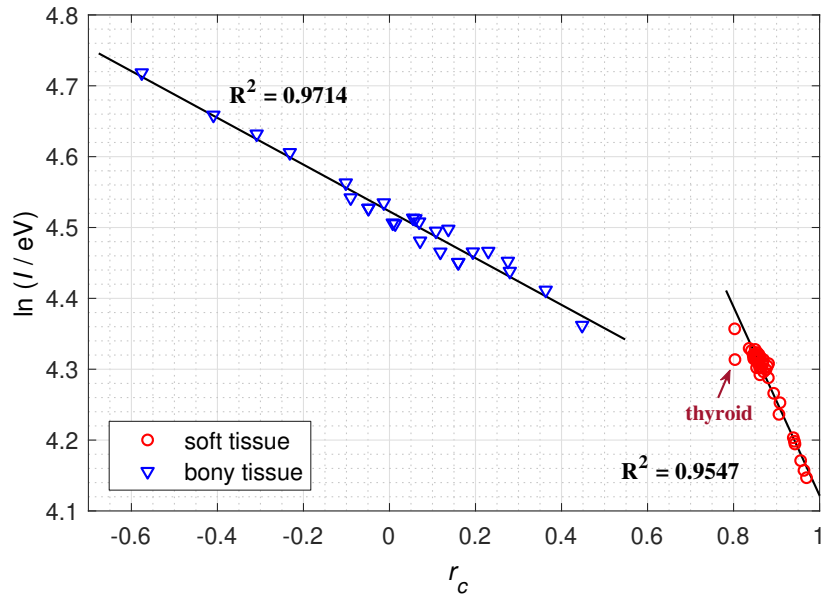
Figure 3.2: The linear relationship between the logarithm of mean excitation energies and the BVM weighted-component-ratio for the reference human tissues.

and then can be applied to patient data. Thyroid tissue is excluded in the linear fitting between $\ln I$ and r_c because it is an outlier to other soft tissues due to the existence of iodine ($Z = 53$). The residual I-value modeling errors for the reference human tissues are all within $\pm 3\%$ (except for thyroid tissue).

The proposed I-value parameterization model, as is the case for all such models, can only approximate I-values for materials with compositions similar to those used to derive the model. In another word, the I-value parameterization functions (2.8), (2.13), and (3.5) only apply to biological tissues. If the composition of a scanned object deviates from those of biological tissues, such as the tissue surrogates used in our experiments, a modified fitting that better reflects the prior knowledge about the composition of the scanned object should be adapted for all I-value parameterization models to reduce the underlying SPR modeling error (see Chapter 6).

Note that the I-value parameterization introduced here is slightly different from the alternative one introduced in the previous work by Han *et al.* [52, 59], which uses an unweighted component ratio defined as $c_1/(c_1 + c_2)$. Following is the derivation of the I-value parameterization using the weighted-component-ratio.

Assume that substance x consists of two component media A and B. Let $\boldsymbol{\mu}_A$ and $\boldsymbol{\mu}_B$ be the column vector of the linear attenuation coefficients of the two component media, and w_A and w_B be the corresponding mass fractions of the two components in substance x. The linear attenuation coefficients of substance x can be approximated via the mixture rule as

$$\left(\frac{\boldsymbol{\mu}}{\rho}\right)_x = w_A \left(\frac{\boldsymbol{\mu}}{\rho}\right)_A + w_B \left(\frac{\boldsymbol{\mu}}{\rho}\right)_B. \tag{3.6}$$

By the result from Section 3.4, the expected BVM component weights of substance x are given by

$$\begin{bmatrix} c_1 \\ c_2 \end{bmatrix} = P\boldsymbol{\mu}_x = \rho_x P \begin{bmatrix} \left(\dfrac{\boldsymbol{\mu}}{\rho}\right)_A & \left(\dfrac{\boldsymbol{\mu}}{\rho}\right)_B \end{bmatrix} \begin{bmatrix} w_A \\ w_B \end{bmatrix}, \tag{3.7}$$

where the transform matrix P is defined in (3.27).

By the Bragg additivity rule, the I-value of substance x is formulated as

$$
\begin{aligned}
\ln I_x &= \frac{w_A \left(\frac{\rho_e}{\rho}\right)_A \ln I_A + w_B \left(\frac{\rho_e}{\rho}\right)_B \ln I_B}{w_A \left(\frac{\rho_e}{\rho}\right)_A + w_B \left(\frac{\rho_e}{\rho}\right)_B} \\[2em]
&= \frac{\left[\left(\frac{\rho_e}{\rho}\right)_A \ln I_A \quad \left(\frac{\rho_e}{\rho}\right)_B \ln I_B\right] \begin{bmatrix} w_A \\ w_B \end{bmatrix}}{\left(\frac{\rho_e}{\rho}\right)_x} \\[2em]
&\approx \frac{\left[\left(\frac{\rho_e}{\rho}\right)_A \ln I_A \quad \left(\frac{\rho_e}{\rho}\right)_B \ln I_B\right] \begin{bmatrix} w_A \\ w_B \end{bmatrix}}{\frac{1}{\rho_x}\left[\rho_{e,1} \quad \rho_{e,2}\right] \begin{bmatrix} c_1 \\ c_2 \end{bmatrix}} \\[2em]
&= \frac{\left[\left(\frac{\rho_e}{\rho}\right)_A \ln I_A \quad \left(\frac{\rho_e}{\rho}\right)_B \ln I_B\right] \left(\rho_x P \left[\left(\frac{\boldsymbol{\mu}}{\rho}\right)_A \quad \left(\frac{\boldsymbol{\mu}}{\rho}\right)_B\right]\right)^{-1} \begin{bmatrix} c_1 \\ c_2 \end{bmatrix}}{\frac{1}{\rho_x}\left[\rho_{e,1} \quad \rho_{e,2}\right] \begin{bmatrix} c_1 \\ c_2 \end{bmatrix}} \\[2em]
&= \frac{\left[\left(\frac{\rho_e}{\rho}\right)_A \ln I_A \quad \left(\frac{\rho_e}{\rho}\right)_B \ln I_B\right] \left(P \left[\left(\frac{\boldsymbol{\mu}}{\rho}\right)_A \quad \left(\frac{\boldsymbol{\mu}}{\rho}\right)_B\right]\right)^{-1} \begin{bmatrix} c_1 \\ c_2 \end{bmatrix}}{\left[\rho_{e,1} \quad \rho_{e,2}\right] \begin{bmatrix} c_1 \\ c_2 \end{bmatrix}} .
\end{aligned}
\tag{3.8}
$$

Then

$$
\ln I_x = a_{r,0} \frac{c_1 \rho_{e,1}}{c_1 \rho_{e,1} + c_2 \rho_{e,2}} + b_{r,0} ,
\tag{3.9}
$$

where the coefficients

$$\begin{bmatrix} a_{r,0} & b_{r,0} \end{bmatrix} = \left[\left(\frac{\rho_e}{\rho}\right)_A \ln I_A \quad \left(\frac{\rho_e}{\rho}\right)_B \ln I_B \right] \left(P \left[\left(\frac{\boldsymbol{\mu}}{\rho}\right)_A \quad \left(\frac{\boldsymbol{\mu}}{\rho}\right)_B \right] \right)^{-1} \begin{bmatrix} \rho_{e,1} & 0 \\ \rho_{e,1} & \rho_{e,2} \end{bmatrix}^{-1} \quad (3.10)$$

only depends on the two component media A and B.

The above result demonstrates that for a series of mixtures that are made up of the same two components, $\ln I$ is linear with the weighted-component-ratio r_c, no matter which pair of basis materials is used. As an extension, for a constrained set of materials whose compositions can be accurately represented by two major principal components (i.e., the soft or bony tissues), $\ln I$ closely follows a linear relationship with r_c.[2]

3.3 Reconstruction of BVM component weights

For an object scanned under DECT protocols, the two images of BVM component weights, $c_1(x)$ and $c_2(x)$, can be recovered by either an image-domain decomposition approach, a sinogram-domain decomposition approach, or our JSIR approach. Figure 3.3 compares the three possible routings.

Image-domain decomposition approach

To implement the BVM-based image-domain method, a phantom containing the two BVM basis materials, polystyrene and 23% $CaCl_2$ solution, is required for the calibration process in order to convert the two HU images into BVM component images [74]. Two BVM component

---

[2]A previous study by Lalonde *et al.* [19] demonstrated that the compositions of soft or bony tissues can be accurately modeled as a combination of two components with varied fractions for different tissues and a third constant component.
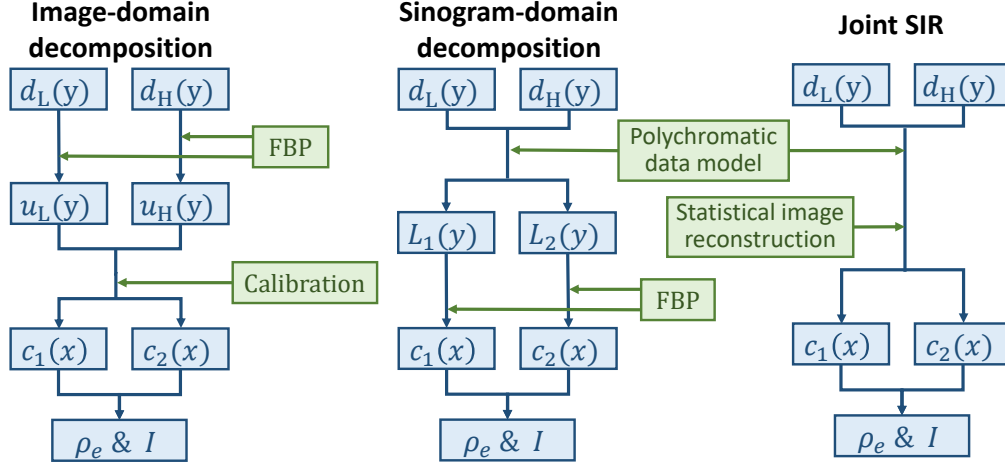
Figure 3.3: Comparison of the three different routings of reconstruction BVM component images from the DECT data.

weights for an unknown material at image location x are computed as

$$
\begin{bmatrix} c_1(x) \\ c_2(x) \end{bmatrix} = \begin{bmatrix} \bar{u}_{1,\mathrm{L}} & \bar{u}_{2,\mathrm{L}} \\ \bar{u}_{1,\mathrm{H}} & \bar{u}_{2,\mathrm{H}} \end{bmatrix}^{-1} \begin{bmatrix} u_{\mathrm{L}}(x) \\ u_{\mathrm{H}}(x) \end{bmatrix} ,
\tag{3.11}
$$

where $u_{\mathrm{L}}(x)$ and $u_{\mathrm{H}}(x)$ are the separately reconstructed SECT images of the scanned object for low and high energy, respectively. $\bar{u}_{i,\mathrm{L}}$ and $\bar{u}_{i,\mathrm{H}}$ are the modified HUs of the basis materials obtained from calibration images.

Sinogram-domain decomposition approach

To implement the BVM-based sinogram-domain method, we rewrite (2.19) for BVM as

$$
\left[\frac{I_d}{I_0} \right]_j (y) = \sum_E \Psi_j(y, E) \exp\left(- L_1(y)\mu_1(E) - L_2(y)\mu_2(E) \right) ,
\tag{3.12}
$$

where $L_i(y) = \sum_x h(y|x)c_i(x)$. The two line-integrals $L_i(y)$ are solved for each source-detector pair y independently and then used to reconstruct the BVM component images $c_i(x)$ via the FBP algorithm.

Joint statistical image reconstruction (JSIR) approach

Unlike the image-domain or sinogram-domain methods that perform separate steps of material decomposition and image reconstruction, the JSIR approach reconstructs the two images of BVM component weights, $\mathbf{c}_1$ and $\mathbf{c}_2$, directly and simultaneously from the two energy-uncompensated measurement sinograms. Instead of assuming an exact match between the ground truth and the measurements, the JSIR reconstruction process is based on a statistical model of CT data and formulated as a penalized maximum likelihood estimation problem.

Let $d_j(y)$, $j \in \{L, H\}$ be the transmission measurement of source-detector pair y, which are assumed to be independently Poisson distributed with mean of

$$Q_j(y : \boldsymbol{\mu}) = I_{0,j}(y) \sum_E \Psi_j(y, E) \exp\left(-\sum_x h(y|x)\mu(x, E) \right) + \gamma_j(y), \qquad (3.13)$$

where $\Psi_j(y, E)$ is the normalized energy-fluence spectra of the two scans and $I_{0,j}(y)$ is the corresponding unattenuated in-air profile, which is expressed in noise-equivalent quanta (NEQ) [35, 36]. Note that in most situations $\Psi_j(y, E)$ and $I_{0,j}(y)$ are detector-dependent because of the bow-tie filter. Additionally, an estimate of background events (i.e., scattered radiation), $\gamma_j(y)$, which is assumed to be known, is also included in the data model to improve the model accuracy.

Plugging (3.1) into (3.13), the expect mean of the transmission measurement can then be written as a function of the two BVM component images as

$$Q_j(y : \mathbf{c}) = I_{0,j}(y) \sum_E \Psi_j(y, E) \exp\left(-\sum_x h(y|x) \sum_{i=1}^{2} c_i(x)\mu_i(E)\right) + \gamma_j(y). \qquad (3.14)$$

To find the maximum likelihood estimator of the two BVM component images, maximization of the Poisson log-likelihood is converted to the equivalent problem of minimizating the I-divergence [75] between the measured transmission data $\mathbf{d}_j$ and the estimated mean values $\mathbf{Q}_j$ parameterized by $\mathbf{c}_i$. The I-divergence is defined as

$$d_I(\mathbf{d}_j\|\mathbf{Q}_j) = \sum_y \left(d_j(y) \ln \frac{d_j(y)}{Q_j(y)} - d_j(y) + Q_j(y)\right), \qquad (3.15)$$

which is nonnegative and is convex over $\mathbf{d}_j$ and $\mathbf{Q}_j$.

Because of the ill-conditioning of the dual-energy reconstruction problem, a regularization function is employed to enforce smooth images. The objective function of the minimization problem is then defined as

$$g(\mathbf{c}) = \sum_{j=\text{L,H}} d_I(\mathbf{d}_j\|\mathbf{Q}_j) + \lambda R(\mathbf{c}), \qquad (3.16)$$

in which the spatial penalty function $R(\mathbf{c}_i)$ is formulated as

$$R(\mathbf{c}) = \sum_{i=1}^{2} \sum_x \sum_{x' \in \mathcal{N}(x)} w_{x,x'} \phi\big(c_i(x) - c_i(x')\big), \qquad (3.17)$$

where $\mathcal{N}(x)$ is the adjacent neighborhood of pixel x, and $w_{x,x'}$ is an inverse-distance weight for each pixel-pair. The value difference between neighboring pixels is penalized by the

potential function

$$\phi(t) = \delta \left(\left| \frac{t}{\delta} \right| - \ln \left(1 + \left| \frac{t}{\delta} \right| \right) \right). \tag{3.18}$$

This Huber-type penalty funcion is a modified version of the well-known log-cosh function, which helps preserve edges while suppressing image noise [76]. The penalty function is convex and twice continuously differentiable, with a quadratic region for $|t| \ll \delta$ and a linear region for $|t| \gg \delta$.

The single scalar λ controls the trade-off between data fitting and image smoothness. A larger λ produces images with a smaller noise level but lower resolution.

The optimization algorithm for minimizing the objective function (3.16) will be discussed in Chapter 4.

3.4   Theoretical value of BVM component weights

Assume that x-ray beams of two different energy spectra pass through a thin layer of material with thickness l, where l is sufficiently small and the source intensities are sufficiently large (i.e., the measurement is noiseless). Let $\Psi_j(E)$ and $I_{0,j}$, $j \in \{\text{L}, \text{H}\}$ be the two spectra and the corresponding source intensities, respectively. Let $\mu_x(E)$ and $\mu_i(E), i \in \{1, 2\}$ be the linear attenuation coefficients of the scanned material and basis materials, respectively. The measured transmission, which equals the true transmission, is formulated as

$$d_j = I_{0,j} \sum_E \Psi_j(E) \exp\left(-l\,\mu_x(E)\right), \tag{3.19}$$

and the BVM-modeled transmission is formulated as

$$Q_j = I_{0,j} \sum_E \Psi_j(E) \exp\left(-l\left(c_1\mu_1(E) + c_2\mu_2(E)\right)\right). \tag{3.20}$$

In our JSIR method, the BVM component weights c_1 and c_2 are determined by minimizing

$$\sum_{j=L,H} d_I(d_j \| Q_j) = \sum_{j=L,H} \left(d_j \ln\left(\frac{d_j}{Q_j}\right) - d_j + Q_j\right). \tag{3.21}$$

Applying the Taylor expansion to the objective function at $l = 0$ gives

$$\sum_{j=L,H} d_I(d_j \| Q_j) = \frac{l^2}{2} \sum_{j=L,H} I_{0,j} \left[\sum_E \Psi_j(E)\left(c_1\mu_1(E) + c_2\mu_2(E) - \mu_x(E)\right)\right]^2 + o(l^2). \tag{3.22}$$

Rewrite (3.22) in matrix form gives

$$\sum_{j=L,H} d_I(d_j \| Q_j)$$

$$= \frac{l^2}{2}\left(\begin{bmatrix}\boldsymbol{\mu}_1 & \boldsymbol{\mu}_2\end{bmatrix}\begin{bmatrix}c_1\\c_2\end{bmatrix} - \boldsymbol{\mu}_x\right)^{\mathsf{T}}\left(\sum_{j=L,H} I_{0,j}\boldsymbol{\Psi}_j\boldsymbol{\Psi}_j{}^{\mathsf{T}}\right)\left(\begin{bmatrix}\boldsymbol{\mu}_1 & \boldsymbol{\mu}_2\end{bmatrix}\begin{bmatrix}c_1\\c_2\end{bmatrix} - \boldsymbol{\mu}_x\right) + o(l^2)$$

$$= \frac{l^2}{2}\left(A\begin{bmatrix}c_1\\c_2\end{bmatrix} - \mathbf{b}\right)^{\mathsf{T}} W\left(A\begin{bmatrix}c_1\\c_2\end{bmatrix} - \mathbf{b}\right) + o(l^2),$$

$$\tag{3.23}$$

where

$$
A = \begin{bmatrix} \boldsymbol{\Psi}_{\mathrm{L}}{}^{\mathsf{T}} \\ \boldsymbol{\Psi}_{\mathrm{H}}{}^{\mathsf{T}} \end{bmatrix} \begin{bmatrix} \boldsymbol{\mu}_1 & \boldsymbol{\mu}_2 \end{bmatrix} = \begin{bmatrix} \sum_E \Psi_{\mathrm{L}}(E)\mu_1(E) & \sum_E \Psi_{\mathrm{L}}(E)\mu_2(E) \\ \sum_E \Psi_{\mathrm{H}}(E)\mu_1(E) & \sum_E \Psi_{\mathrm{H}}(E)\mu_2(E) \end{bmatrix},
$$

$$
\mathbf{b} = \begin{bmatrix} \boldsymbol{\Psi}_{\mathrm{L}}{}^{\mathsf{T}} \\ \boldsymbol{\Psi}_{\mathrm{H}}{}^{\mathsf{T}} \end{bmatrix} \boldsymbol{\mu}_x = \begin{bmatrix} \sum_E \Psi_{\mathrm{L}}(E)\mu_x(E) \\ \sum_E \Psi_{\mathrm{H}}(E)\mu_x(E) \end{bmatrix}, \tag{3.24}
$$

$$
W = \begin{bmatrix} I_{0,\mathrm{L}} & 0 \\ 0 & I_{0,\mathrm{H}} \end{bmatrix}.
$$

Thus, the theoretical BVM component weights are given by a least-squares fitting of the linear attenuation coefficient curve weighted by $\left(\sum_{j=\mathrm{L,H}} I_{0,j} \boldsymbol{\Psi}_j \boldsymbol{\Psi}_j{}^{\mathsf{T}} \right)$ as

$$
\begin{aligned}
\begin{bmatrix} c_1 \\ c_2 \end{bmatrix} &= \operatorname*{argmin}_{\boldsymbol{\tau}} \left(\begin{bmatrix} \boldsymbol{\mu}_1 & \boldsymbol{\mu}_2 \end{bmatrix} \boldsymbol{\tau} - \boldsymbol{\mu}_x \right)^{\mathsf{T}} \left(\sum_{j=\mathrm{L,H}} I_{0,j} \boldsymbol{\Psi}_j \boldsymbol{\Psi}_j{}^{\mathsf{T}} \right) \left(\begin{bmatrix} \boldsymbol{\mu}_1 & \boldsymbol{\mu}_2 \end{bmatrix} \boldsymbol{\tau} - \boldsymbol{\mu}_x \right) \\
&= \operatorname*{argmin}_{\boldsymbol{\tau}} (A\boldsymbol{\tau} - \mathbf{b})^{\mathsf{T}} W (A\boldsymbol{\tau} - \mathbf{b}) \\
&= (A^{\mathsf{T}} W A)^{-1} (A^{\mathsf{T}} W) \, \mathbf{b},
\end{aligned} \tag{3.25}
$$

which is equivalent to

$$
\begin{bmatrix} c_1 \\ c_2 \end{bmatrix} = P \boldsymbol{\mu}_x, \tag{3.26}
$$

where

$$
P = (A^{\mathsf{T}} W A)^{-1} (A^{\mathsf{T}} W) \begin{bmatrix} \boldsymbol{\Psi}_{\mathrm{L}}{}^{\mathsf{T}} \\ \boldsymbol{\Psi}_{\mathrm{H}}{}^{\mathsf{T}} \end{bmatrix}. \tag{3.27}
$$

Figure 3.4 compares the simulated and computed BVM component weights for 4 representative reference tissues. The simulated BVM weights are the reconstructed values at the centers of cylindrical, homogeneous objects with diameters of 40, 80, 120, ..., 280, and 320 cm, while the computed BVM weights were derived using the corresponding local spectra at the centers (i.e., source spectra filtered by the tissue of the corresponding diameters). It can be seen that there is a good agreement between the computed and simulated BVM weights. The differences are less than 10^{-3} for cortical bone and are well below 2×10^{-4} for soft tissue and spongiosa. Thus, the theoretical BVM component weights computed via (3.26) are able to represent the expected ground truth with very high accuracy.

Note that the theoretical BVM component weights depend slightly on the local spectra, and therefore may change slightly across a homogeneous object. However, the impact of the location-dependent equivalent spectra is much less than that of SPR modeling error and image formation uncertainty. A spectrum variation of up to 400 mm water filtration leads to less than 0.03% and 0.1% changes of predicted ρ_e for all the reference soft and bony tissues, respectively, except for the thyroid tissue. The changes of predicted I-value are less than 0.14% and 0.18% for the reference soft and bony tissues, respectively.

In the JSIR-BVM method, the unattenuated central-axis spectra were used to compute the theoretical BVM weights of the reference human tissues for fitting the I-value parameterization functions.
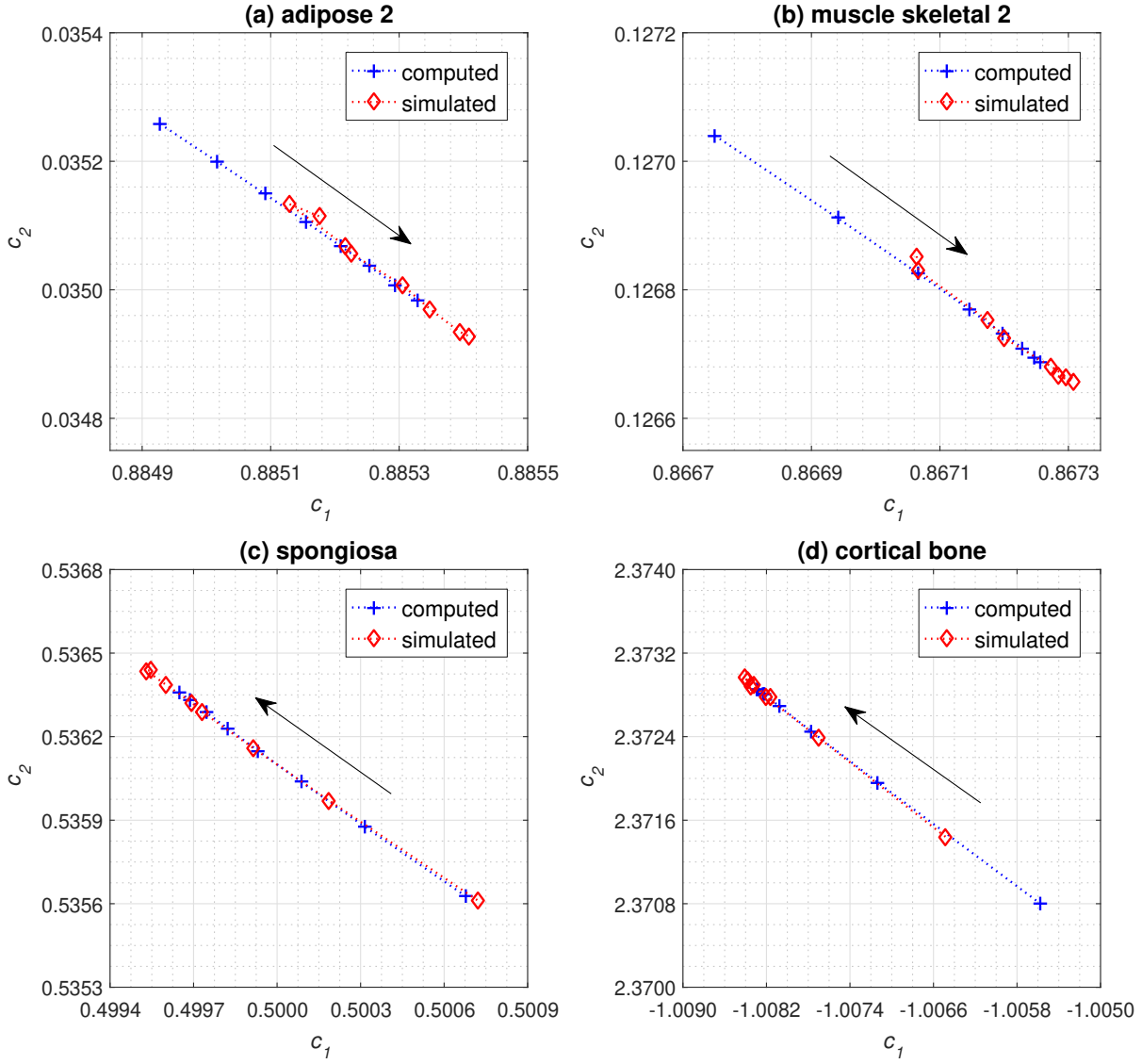
Figure 3.4: Comparison of theoretically computed BVM weights and simulated BVM weights for selected reference human tissues under difference levels of addition spectral filtration by varying object size. The arrows indicate the directions of phantom size increase.

Chapter 4

Joint statistical image reconstruction (JSIR) of DECT data

In the JSIR-BVM method, the reconstruction of the two BVM component images is formulated as an optimization problem with the objective function defined by (3.16). The optimization problem can be solved by the regularized dual-energy alternating minimization (DE-AM) algorithm [41, 42], which alternately minimizes a decomposed surrogate function in each iteration (see Appendix B). The surrogate function is an upper bound of the original objective function and is much easier to minimize than the original objective function. Therefore, decreasing the value of the surrogate function ensures a decrease in the original objective function.

The original DE-AM algorithm, however, suffers from slow convergence [77]. In this chapter, we derive a modified DE-AM algorithm, which can dramatically speed up the convergence and is able to achieve convergence speed that is comparable to a monochromatic single-energy AM algorithm. Most acceleration strategies for the monochromatic single-energy AM algorithm, such as the subset methods [78–82] and the momentum methods [82, 83], can be applied to the modified DE-AM algorithm for further acceleration.

Note that all the algorithms evaluated in this chapter are unregularized and are implemented without ordered subsets. Unless otherwise indicated, all synthetic data are generated without noise and background events.

4.1 Constraint on BVM component weights

Within the photon energy range of CT scans (i.e., from $20\,\mathrm{keV}$ to $150\,\mathrm{keV}$), the photon linear attenuation coefficient function of typical tissue samples are nonnegative and nonincreasing with respect to energy E. To achieve meaningful reconstruction results, the objective function (3.16) should be minimized under the constraint

$$
\begin{aligned}
(\mathbf{c}_1, \mathbf{c}_2) \in \mathcal{D}_\mathbf{c} = \Big\{ &(\mathbf{c}_1, \mathbf{c}_2) : c_1(x)\mu_1(E) + c_2(x)\mu_2(E) \geq 0 \quad \forall\, (x, E) : E_{\min} \leq E \leq E_{\max}; \\
&c_1(x)\mu_1(E_a) + c_2(x)\mu_2(E_a) \geq c_1(x)\mu_1(E_b) + c_2(x)\mu_2(E_b) \quad \forall\, (x, E_a, E_b) : \\
&E_{\min} \leq E_a < E_b \leq E_{\max} \Big\}.
\end{aligned}
$$

To simplify the constraint in the reconstruction algorithm, we use a projected basis vector-pair

$$
\begin{bmatrix} \tilde{\boldsymbol{\mu}}_1 & \tilde{\boldsymbol{\mu}}_2 \end{bmatrix} = \begin{bmatrix} \boldsymbol{\mu}_1 & \boldsymbol{\mu}_2 \end{bmatrix} \begin{bmatrix} 1 & -\xi_a \\ -\xi_b & 1 \end{bmatrix}^{\mathsf{T}} \tag{4.1}
$$

instead of the actual linear attenuation function of the two physical basis materials, $\begin{bmatrix} \boldsymbol{\mu}_1 & \boldsymbol{\mu}_2 \end{bmatrix}$, in the reconstruction algorithm. The corresponding projected component weights are then

given by

$$\begin{bmatrix} \tilde{\mathbf{c}}_1 & \tilde{\mathbf{c}}_2 \end{bmatrix} = \begin{bmatrix} \mathbf{c}_1 & \mathbf{c}_2 \end{bmatrix} \begin{bmatrix} 1 & -\xi_a \\ -\xi_b & 1 \end{bmatrix}^{-1}, \tag{4.2}$$

which satisfies

$$\begin{bmatrix} \tilde{\boldsymbol{\mu}}_1 & \tilde{\boldsymbol{\mu}}_2 \end{bmatrix} \begin{bmatrix} \tilde{\mathbf{c}}_1^{\mathsf{T}} \\ \tilde{\mathbf{c}}_2^{\mathsf{T}} \end{bmatrix} = \begin{bmatrix} \boldsymbol{\mu}_1 & \boldsymbol{\mu}_2 \end{bmatrix} \begin{bmatrix} \mathbf{c}_1^{\mathsf{T}} \\ \mathbf{c}_2^{\mathsf{T}} \end{bmatrix}. \tag{4.3}$$

Let

$$\begin{aligned} \xi_a &= \min \left(\min_{E_{\min} \leq E \leq E_{\max}} \frac{\mu_1(E)}{\mu_2(E)}, \ \min_{E_{\min} \leq E_a < E_b \leq E_{\max}} \frac{\mu_1(E_a) - \mu_1(E_b)}{\mu_2(E_a) - \mu_2(E_b)} \right), \\ \xi_b &= \min \left(\min_{E_{\min} \leq E \leq E_{\max}} \frac{\mu_2(E)}{\mu_1(E)}, \ \min_{E_{\min} \leq E_a < E_b \leq E_{\max}} \frac{\mu_2(E_a) - \mu_2(E_b)}{\mu_1(E_a) - \mu_1(E_b)} \right). \end{aligned} \tag{4.4}$$

Then the constraint $(\mathbf{c}_1, \mathbf{c}_2) \in \mathcal{D}_{\mathbf{c}}$ is equivalent to nonnegativity constraints over $\tilde{\mathbf{c}}_1$ and $\tilde{\mathbf{c}}_2$, i.e.,

$$(\tilde{\mathbf{c}}_1, \tilde{\mathbf{c}}_2) \in \tilde{\mathcal{D}}_{\mathbf{c}} = \left\{ (\tilde{\mathbf{c}}_1, \tilde{\mathbf{c}}_2) : \forall x, \ \tilde{c}_1(x) \geq 0, \ \tilde{c}_2(x) \geq 0 \right\}. \tag{4.5}$$

For simplicity of notation, we denote the projected basis vector-pair $(\tilde{\boldsymbol{\mu}}_1, \tilde{\boldsymbol{\mu}}_2)$ and the corresponding component weights $(\tilde{\mathbf{c}}_1, \tilde{\mathbf{c}}_2)$ as $(\boldsymbol{\mu}_1, \boldsymbol{\mu}_2)$ and $(\mathbf{c}_1, \mathbf{c}_2)$, respectively, in the remainder of this chapter and in Appendix B, which discuss the reconstruction algorithms. While in the other parts of this dissertation, we only discuss the component weights for the original basis vector-pair that is the linear attenuation functions of basis materials.

4.2 Factors limiting convergence speed of the DE-AM algorithm

As stated in Appendix B, the generalized AM algorithm can be applied to different categories of forward data models. In order to reveal the impact of forward model complexity on the algorithm convergence, we choose three representative categories of models: (1) the monochromatic single-energy model

$$Q(y) = I_0(y) \exp\left(-\sum_x h(y|x)\bar{\mu}_0 c_i(x) \right), \tag{4.6}$$

(2) the polychromatic single-energy model

$$Q(y) = I_0(y) \sum_E \Psi(y, E) \exp\left(-\sum_x h(y|x)\mu_0(E)c_0(x) \right), \tag{4.7}$$

and (3) the polychromatic dual-energy model

$$Q_j(y) = I_{0,j}(y) \sum_E \Psi_j(y, E) \exp\left(-\sum_x h(y|x) \sum_{i=1}^{2} \mu_i(E)c_i(x) \right), \quad j \in \{\mathrm{L}, \mathrm{H}\}. \tag{4.8}$$

The corresponding AM algorithms are referred to as the M-SE-AM, P-SE-AM, and DE-AM algorithms, respectively. For the two single-energy reconstructions, $\boldsymbol{\mu}_0$ was chosen to be the attenuation function of water and $\bar{\mu}_0$ was chosen to be the effective attenuation coefficient of water given the source spectrum.

The three categories of AM algorithms are compared using the same virtual mini CT scanner geometry (see Section 4.5). Figure 4.1 compares the convergence of the above three AM algorithms for modeling error-free and noise-free sinograms. The result suggests that for the same geometry and similar objects, the DE-AM algorithm requires more than 1000 times the
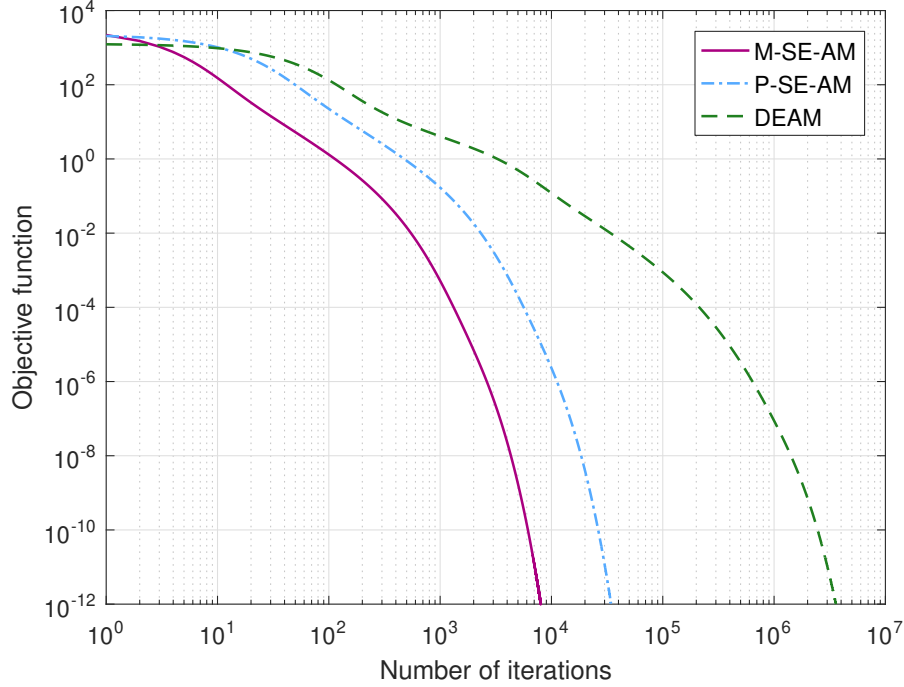
Figure 4.1: Objective function values as a function of iteration numbers for different categories of AM algorithms.

number of iterations to achieve a convergence level comparable to the M-SE-AM algorithm. The P-SE-AM algorithm is about 3 to 5 times slower than the M-SE-AM algorithm.[1]

In each iteration of the AM algorithm (see Appendix B), the objective function $g(\mathbf{c})$ is "lifted" twice to get the alternative function that is much easier to minimize. The first lifting results in the surrogate function $g^{\mathrm{sur}}(\mathbf{c} : \hat{\mathbf{c}}^{(k)})$ and the second one results in the decoupled surrogate function $\tilde{g}^{\mathrm{sur}}(\mathbf{c} : \hat{\mathbf{c}}^{(k)})$, which has a closed-form solution.

---

[1]In the polychromatic implementations (i.e., the P-SE-AM and DE-AM algorithms), the minimum photon energy E_{min} was set to $20\,\mathrm{keV}$. A lower minimum energy will further slow down the two algorithms due to a larger auxiliary variable $z(i, x)$ given by (B.19).

To illustrate the explanation of the slow convergence of the DE-AM algorithm more clearly, we rewrite the decoupling process (B.20) into two sub-steps as follows

$$
\begin{aligned}
g^{\mathrm{sur}}&(\mathbf{c}:\hat{\mathbf{c}}^{(k)}) \\
&= \sum_j \sum_y \sum_E \left[\hat{p}_j^{(k)}(y,E) \sum_i \mu_i(E) \sum_x h(y|x) c_i(x) \right. \\
&\qquad \left. + \hat{q}_j^{(k)}(y,E) \exp\left(-\sum_i \mu_i(E) \sum_x h(y|x)\big(c_i(x) - \hat{c}_i^{(k)}(x)\big) \right) \right] + C \\
&\leq \sum_j \sum_y \sum_E \sum_i \left[\hat{p}_j^{(k)}(y,E)\mu_i(E) \sum_x h(y|x) c_i(x) \right. \\
&\qquad \left. + \hat{q}_j^{(k)}(y,E)\frac{\mu_i(E)}{z_1(i)} \exp\left(-z_1(i) \sum_x h(y|x)\big(c_i(x) - \hat{c}_i^{(k)}(x)\big) \right) \right] + C \\
&\leq \sum_j \sum_y \sum_E \sum_i \sum_x \left[\hat{p}_j^{(k)}(y,E)\mu_i(E)h(y|x) c_i(x) \right. \\
&\qquad \left. + \hat{q}_j^{(k)}(y,E)\frac{\mu_i(E)}{z_1(i)}\frac{h(y|x)}{z_2(x)} \exp\left(-z_1(i)z_2(x)\big(c_i(x) - \hat{c}_i^{(k)}(x)\big) \right) \right] + C \\
&= \tilde{g}^{\mathrm{sur}}\big(\mathbf{c}:\hat{\mathbf{c}}^{(k)}\big),
\end{aligned}
\tag{4.9}
$$

where the auxiliary variables $z_1(i)$ and $z_2(x)$ satisfy

$$
\begin{aligned}
&z_1(i) \geq 0, \ \forall i; \\
&z_2(x) \geq 0, \ \forall x; \\
&\sum_i \frac{\mu_i(E)}{z_1(i)} \leq 1, \ \forall E; \\
&\sum_x \frac{h(y|x)}{z_2(x)} \leq 1, \ \forall y.
\end{aligned}
\tag{4.10}
$$

The first decoupling is referred to as the *basis decoupling* and the second one is referred to as the *spatial decoupling*.

It can be seen that the constraint over $z_2(x)$ is the same for all categories of AM algorithms whenever the scanner geometry and image size are the same. Thus, we assume that the impacts from spatial decoupling are comparable for all categories of AM algorithms. Several acceleration strategies of the M-SE-AM algorithm have been previously discussed [82]. In this dissertation, we only focus on the impact of basis decoupling and surrogate lifting and derive acceleration methods that are related to these two factors.

- Basis decoupling:

  In the original DE-AM algorithm, the update of each iteration, $\left(\hat{\mathbf{c}}^{(k+1)} - \hat{\mathbf{c}}^{(k)}\right)$, is proportional to the reciprocal of the auxiliary variable $z(i, x) = z_1(i)z_2(x)$. Therefore, smaller auxiliary variables lead to larger updates in each iteration.

  On the other hand, in order to ensure that the surrogate function upper-bounds the original objective function, the auxiliary variables are constrained by

  $$\omega(y, E) \equiv \sum_x \sum_i \frac{\mu_i(E)h(y|x)}{z(i, x)} \leq 1. \tag{4.11}$$

  We can use $\omega(y, E)$ as an indicator for the relaxation level of the decoupling. A small $\omega(y, E)$ suggests that there exists a large gap between the un-decoupled and decoupled functions and with high possibility the step size is underestimated.

  Figure 4.2 shows the distribution of $\omega(y, E)$ for a typical conventional CT scanner geometry (i.e., the Philips Brilliance Big Bore scanner) for the three categories of AM algorithms. For the M-SE-AM algorithm, a large fraction of $\omega(y, E)$'s are close to 1. For the P-SE-AM and DE-AM algorithms, however, the majority of $\omega(y, E)$'s are less than 0.25 and 0.1, respectively. Empirically, a simple scale-down of $z(i, x)$ by 4-fold and 10-fold in the P-SE-AM and DE-AM algorithms, respectively, would still guarantee monotonic convergence of the algorithms for various scanner geometries.
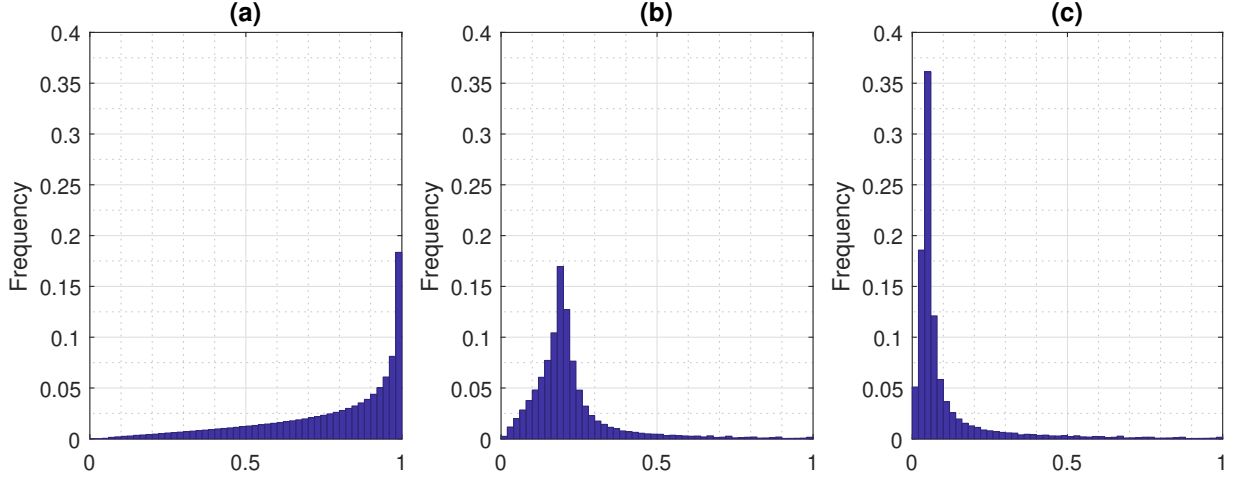
Figure 4.2: The distribution of $\omega(y, E)$ for (a) M-SE-AM algorithm, (b) P-SE-AM algorithm, and (c) DE-AM algorithm.

In addition, Chen [77] has shown that there exists a high correlation between the two BVM component weights, which is much higher than the spatial correlation. Therefore, the objective function is highly ridged in the basis domain. Because the two BVM component weights are updated separately in the original DE-AM algorithm, such high correlation in the basis domain also contributes to the slow convergence.

- Surrogate lifting:

  The surrogate function retains the same gradient as the original objective function but has a different curvature. For the single-energy case, the surrogate function is a good approximation of the original function. However, for the dual-energy case, there exist large gaps between the surrogate function and the highly ridged objective function in some directions. Therefore, even if the optimal point of the surrogate function is achieved in each iteration, it may not be a good update for the original objective function.
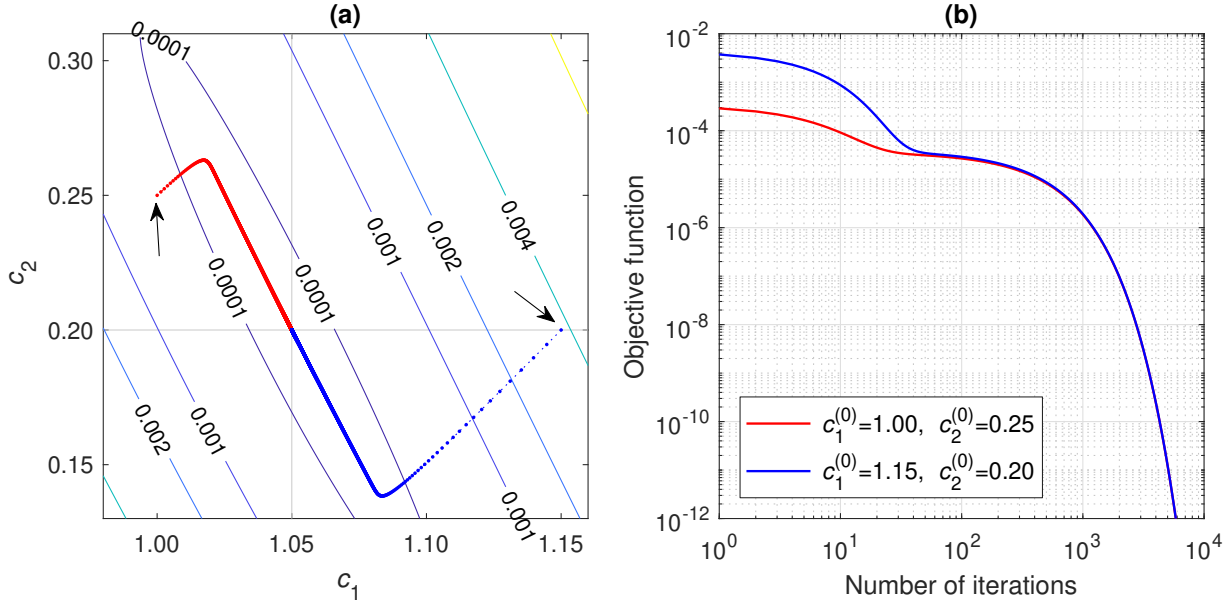
Figure 4.3: (a) Contour lines of $g(\mathbf{c})$ and the trajectory of $\mathbf{c}^{(k)}$ for the DE-AM algorithm and (b) the objective function *vs.* iteration numbers corresponding to the trajectories. The arrows in (a) indicate the initial points.

To visualize the two issues above, we consider a reduced dual-energy problem that has only one ray path (i.e., source-detector pair) and one image region that needs to be estimated. The reduced forward model is as follows,

$$Q_j(\mathbf{c}) = I_{0,j} \sum_E \Psi_j(E) \exp\left(-h_0 \sum_{i=1}^2 \mu_i(E) c_i\right), \quad j \in \{\mathrm{L}, \mathrm{H}\} \tag{4.12}$$

in which h_0 is set to $100\,\mathrm{mm}$ and the ground truth is set to $c_1^* = 1.05$ and $c_2^* = 0.20$, which are approximately the BVM component weights of water.[2]

Figure 4.3 shows the iterations of the DE-AM algorithm for two different initial points. The contour lines of the objective function indicate that it has a hill-valley shape in the basis domain. The estimates drop down the hill within about $40-50$ iterations and then go slowly along the valley, which requires thousands of iterations to get close to the optimal point.

---

[2]Note that these c_i values correspond to the projected BVM component weights as described in Section 4.1.

To further separate the impact of basis decoupling and surrogate lifting, we then analyze two modified problems from the same initial points.

Figure 4.4 shows the DE-AM iterations that minimize the centered surrogate function $g^{\mathrm{sur}}(\mathbf{c} : \mathbf{c}^*)$, which is expanded at the ground truth $\mathbf{c}^*$ and has the same optimal point as the original objective function $g(\mathbf{c})$. This modification has no surrogate lifting but is affected by the basis decoupling. The centered surrogate function also has a hill-valley shape (not shown in the figure). The trajectories of the estimates have similar behavior as in Figure 4.3 (i.e., dropping down the hill and going slowly along the valley of the centered surrogate function) but it requires about 10-fold fewer iterations to achieve convergence.

Figure 4.5 shows the iterations for finding the exact optimal point of the surrogate function $g^{\mathrm{sur}}(\mathbf{c} : \hat{\mathbf{c}}^{(k)})$ in each iteration. Thus the convergence is only affected by the surrogate lifting. We can see that the minimization of the alternative surrogate function is very ineffective along the valley of the original objective function. It takes only one step to reach the valley but about 100 iterations to crawl along the valley. Furthermore, Figure 4.6 shows the ratio of the surrogate function $g^{\mathrm{sur}}(\mathbf{c} : \mathbf{c}^*)$ to the original objective function $g(\mathbf{c})$. It can be seen that although the surrogate function is quite close to the objective function in some directions, its value can be over 10 times larger than the objective function along the valley direction. Thus, the surrogate function is a very poor approximation of the objective function in the valley direction, which contributes to the small step-sizes shown in Figure 4.5.

In the following, we derive algorithm modifications to deal with the two factors causing slow convergence. In Section 4.3, we propose a modified DE-AM algorithm that attempts to eliminate the impact of basis decoupling. Then in Section 4.4, we propose an algorithm based on an approximate function instead of the surrogate function that is able to achieve faster convergence beyond the limitation of the surrogate function.
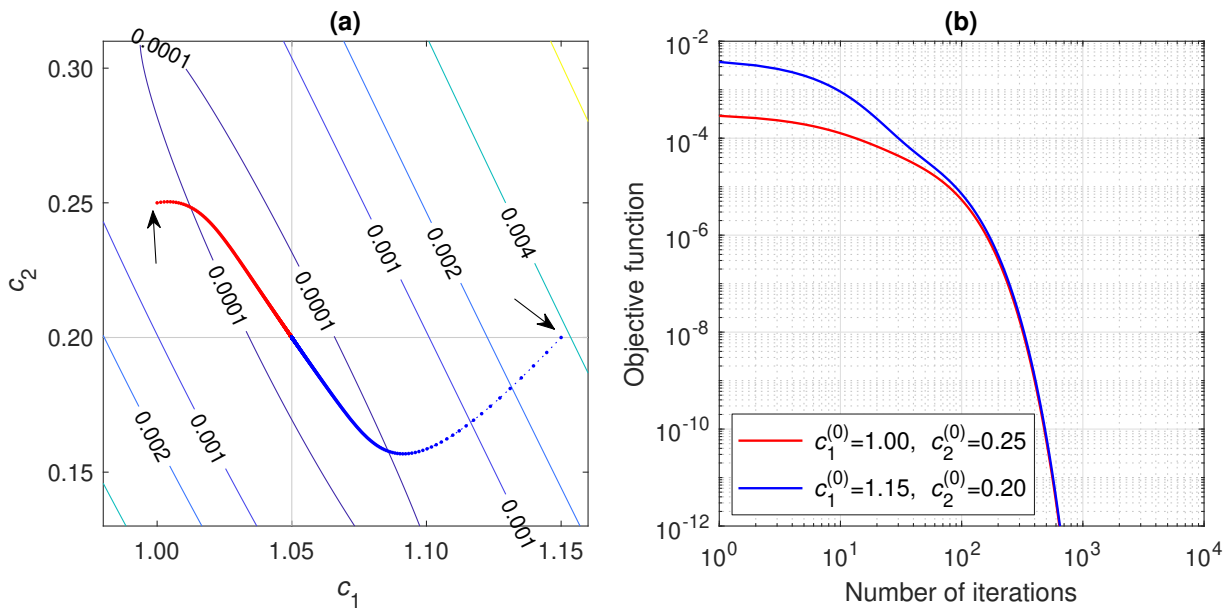
Figure 4.4: (a) Contour lines of $g(\mathbf{c})$ and the trajectory of $\mathbf{c}^{(k)}$ for minimizing the centered surrogate function $g^{\mathrm{sur}}(\mathbf{c} : \mathbf{c}^*)$ and (b) the objective function *vs.* iteration numbers . The arrows in (a) indicate the initial points.
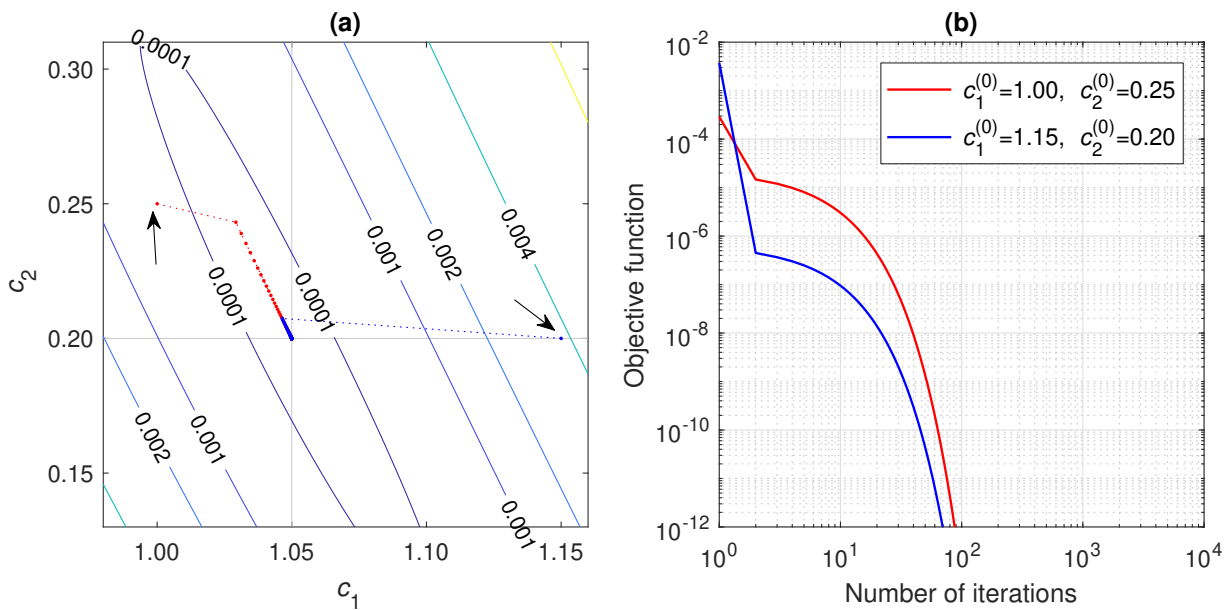
Figure 4.5: (a) Contour lines of $g(\mathbf{c})$ and the trajectory of $\mathbf{c}^{(k)}$ for finding the optimal point of the surrogate function $g^{\mathrm{sur}}(\mathbf{c} : \hat{\mathbf{c}}^{(k)})$ in each iteration and (b) the objective function *vs.* iteration numbers. The arrows in (a) indicate the initial points.
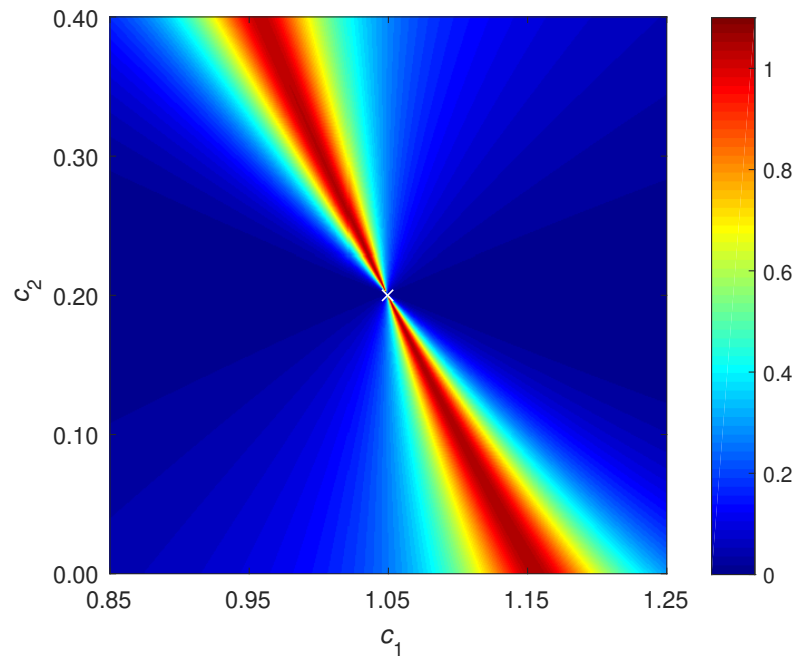
Figure 4.6: The common logarithm (base 10) of the ratio of the centered surrogate function relative to the original objective function, $\log_{10}\left(g^{\mathrm{sur}}\left(\mathbf{c}:\mathbf{c}^*\right)/g(\mathbf{c})\right)$, for the reduced problem.

4.3 Acceleration with Newton's update in the basis domain

In order to eliminate slow convergence due to the basis decoupling, we apply a spatial-only decoupling to the surrogate function as follows,

$$
\begin{aligned}
g^{\text{sur}}&\left(\mathbf{c} : \hat{\mathbf{c}}^{(k)}\right)\\
&= \sum_j \sum_y \sum_E \left[\hat{p}_j^{(k)}(y, E) \left(\sum_x \sum_i h(y|x)\mu_i(E)c_i(x) \right) \right.\\
&\quad \left. + \hat{q}_j^{(k)}(y, E) \exp\left(-\sum_x h(y|x) \sum_i \mu_i(E)\big(c_i(x) - \hat{c}_i^{(k)}(x)\big) \right) \right] + C\\
&= \sum_j \sum_y \sum_E \left[\hat{p}_j^{(k)}(y, E) \sum_x h(y|x) \sum_i \mu_i(E)c_i(x) \right.\\
&\quad \left. + \hat{q}_j^{(k)}(y, E) \exp\left(-\sum_x \frac{h(y|x)}{z_0(x,y)} z_0(x,y) \sum_i \mu_i(E)\big(c_i(x) - \hat{c}_i^{(k)}(x)\big) \right) \right] + C\\
&\leq \sum_x \sum_j \sum_y \sum_E \left[\hat{p}_j^{(k)}(y, E)h(y|x) \sum_i \mu_i(E)c_i(x) \right.\\
&\quad \left. + \hat{q}_j^{(k)}(y, E) \frac{h(y|x)}{z_0(x,y)} \exp\left(-z_0(x,y) \sum_i \mu_i(E)\big(c_i(x) - \hat{c}_i^{(k)}(x)\big) \right) \right] + C\\
&= \breve{g}^{\text{sur}}\left(\mathbf{c} : \hat{\mathbf{c}}^{(k)}\right),
\end{aligned}
\tag{4.13}
$$

where the auxiliary variable

$$
z_0(x, y) = \sum_{x'} h(y|x')
\tag{4.14}
$$

satisfies the constraint of the convex decomposition lemma (Lemma B.2).

Therefore, $\breve{g}_{\text{sur}}\left(\mathbf{c} : \hat{\mathbf{c}}^{(k)}\right)$ is decoupled in the spatial domain (i.e., is separable for each image location x) but is not decoupled in the energy/basis domain. The decoupled surrogate

function can be rewritten as a decoupled sum

$$\breve{g}^{\text{sur}}\left(\mathbf{c} : \hat{\mathbf{c}}^{(k)}\right) = \sum_x \breve{g}_x^{\text{sur}}\left(\mathbf{c}(x) : \hat{\mathbf{c}}^{(k)}(x)\right), \tag{4.15}$$

where $\mathbf{c}(x) = \begin{bmatrix} c_1(x) & c_2(x) \end{bmatrix}^{\mathsf{T}}$.

To derive an algorithm, Newton's method is used to minimize $\breve{g}_{\text{sur}}(\mathbf{c} : \hat{\mathbf{c}}^{(k)})$ over $\mathbf{c}$ for each image location x in parallel.

Let

$$\nabla \breve{g}_x^{\text{sur}}(x) = \begin{bmatrix} \nabla_1(x) \\ \nabla_2(x) \end{bmatrix} \tag{4.16}$$

and

$$\nabla^2 \breve{g}_x^{\text{sur}}(x) = \begin{bmatrix} \nabla_{1,1}^2(x) & \nabla_{1,2}^2(x) \\ \nabla_{2,1}^2(x) & \nabla_{2,2}^2(x) \end{bmatrix} \tag{4.17}$$

be the gradient and Hessian matrix of $\breve{g}_x^{\text{sur}}\left(\mathbf{c}(x) : \hat{\mathbf{c}}^{(k)}(x)\right)$ at the current estimate $\hat{\mathbf{c}}^{(k)}(x)$, which are given by

$$\begin{aligned}
\nabla_i(x) &= \frac{\partial}{\partial c_i(x)} \breve{g}_x^{\text{sur}}\left(\mathbf{c}(x) : \hat{\mathbf{c}}^{(k)}(x)\right)\Big|_{\mathbf{c}(x)=\hat{\mathbf{c}}^{(k)}(x)} \\
&= \sum_y h(y|x) \left[\sum_j \sum_E \hat{p}_j^{(k)}(y, E)\mu_i(E) - \sum_j \sum_E \hat{q}_j^{(k)}(y, E)\mu_i(E) \right]
\end{aligned} \tag{4.18}$$

and

$$\nabla^2_{i,i'}(x) = \frac{\partial^2}{\partial c_i(x) \partial c_{i'}(x)} \breve{g}_x^{\mathrm{sur}}\big(\mathbf{c}(x) : \hat{\mathbf{c}}^{(k)}(x)\big)\bigg|_{\mathbf{c}(x)=\hat{\mathbf{c}}^{(k)}(x)}$$
$$= \sum_y h(y|x) z_0(x,y) \left[\sum_j \sum_E \hat{q}_j^{(k)}(y,E) \mu_i(E) \mu_{i'}(E) \right], \tag{4.19}$$

respectively. Because $\boldsymbol{\mu_1}$ and $\boldsymbol{\mu_2}$ are linearly independent, the Hessian matrix is positive definite.

Let $\Delta \mathbf{c}^{(k)}$ be the Newton direction of the decoupled surrogate function $\breve{g}^{\mathrm{sur}}\big(\mathbf{c} : \hat{\mathbf{c}}^{(k)}\big)$ at $\mathbf{c} = \hat{\mathbf{c}}^{(k)}$, i.e., for each image pixel x,

$$\Delta \mathbf{c}^{(k)}(x) = \begin{bmatrix} \Delta c_1^{(k)}(x) \\ \Delta c_2^{(k)}(x) \end{bmatrix} = -\big[\nabla^2 \breve{g}_x^{\mathrm{sur}}(x)\big]^{-1} \big[\nabla \breve{g}_x^{\mathrm{sur}}(x)\big]. \tag{4.20}$$

Note that the decoupled surrogate function $\breve{g}^{\mathrm{sur}}\big(\mathbf{c} : \hat{\mathbf{c}}^{(k)}\big)$ has the same gradient as the original objective function $g(\mathbf{c})$ at $\mathbf{c} = \hat{\mathbf{c}}^{(k)}$, i.e.,

$$\nabla g\big(\hat{\mathbf{c}}^{(k)}\big) = \nabla g^{\mathrm{sur}}\big(\hat{\mathbf{c}}^{(k)} : \hat{\mathbf{c}}^{(k)}\big) = \nabla \breve{g}^{\mathrm{sur}}\big(\hat{\mathbf{c}}^{(k)} : \hat{\mathbf{c}}^{(k)}\big). \tag{4.21}$$

The directional derivative of $g(\mathbf{c})$ along $\Delta \mathbf{c}^{(k)}$

$$\big[\nabla g\big(\hat{\mathbf{c}}^{(k)}\big)\big]^{\mathsf{T}} \Delta \mathbf{c}^{(k)} = \big[\nabla \breve{g}^{\mathrm{sur}}\big(\hat{\mathbf{c}}^{(k)} : \hat{\mathbf{c}}^{(k)}\big)\big]^{\mathsf{T}} \Delta \mathbf{c}^{(k)}$$
$$= -\sum_x \big[\nabla \breve{g}_x^{\mathrm{sur}}(x)\big]^{\mathsf{T}} \big[\nabla^2 \breve{g}_x^{\mathrm{sur}}(x)\big]^{-1} \big[\nabla \breve{g}_x^{\mathrm{sur}}(x)\big] < 0 \tag{4.22}$$

if $\mathbf{c}^{(k)}$ is not the optimal point of $g(\mathbf{c})$. Therefore, $\Delta\mathbf{c}^{(k)}$ is ensured to be a descent direction of the original objective function $g(\mathbf{c})$. The backtracking line search method [84] is used to select the step size in each iteration.

The iterative reconstruction algorithm is show below.

Algorithm 1: Accelerated DE-AM algorithm #1

Pre-compute $z_0(x,y) = \sum_{x'} h\left(y|x'\right)$

Initialize $c_i^{(0)}(x)$

Select $\alpha \in (0,1)$

for $k = 0, 1, 2, \ldots$ **do**

$\quad$ **foreach** y, j, E **do**

$\quad\quad$ $\hat{q}_j^{(k)}(y,E) = I_{0,j}(y)\Psi_j(y,E)\exp\left(-\sum_x h(y|x)\sum_i \mu_i(E)c_i^{(k)}(x)\right)$

$\quad\quad$ $\hat{p}_j^{(k)}(y,E) = d_j(y)\dfrac{\hat{q}_j^{(k)}(y,E)}{\sum_{E'}\hat{q}_j^{(k)}(y,E')}$

$\quad$ **end**

$\quad$ **foreach** x **do**

$\quad\quad$ Compute $\nabla \breve{g}_x^{\mathrm{sur}}(x)$ and $\nabla^2 \breve{g}_x^{\mathrm{sur}}(x)$ by (4.18) and (4.19)

$\quad\quad$ Compute the Newton direction $\Delta\mathbf{c}^{(k)}(x) = -\left[\nabla^2\breve{g}_x^{\mathrm{sur}}(x)\right]^{-1}\left[\nabla\breve{g}_x^{\mathrm{sur}}(x)\right]$

$\quad$ **end**

$\quad$ Choose the maximum step size $t^{(k)} = t \in (0,1]$ that satisfies

$\quad\quad$ $g\left(\hat{\mathbf{c}}^{(k)} + t\Delta\mathbf{c}^{(k)}\right) \leq g\left(\hat{\mathbf{c}}^{(k)}\right) + \alpha t\left[\nabla g\left(\hat{\mathbf{c}}^{(k)}\right)\right]^{\mathsf{T}}\Delta\mathbf{c}^{(k)}$

$\quad$ Update $\hat{\mathbf{c}}^{(k+1)} = \hat{\mathbf{c}}^{(k)} + t^{(k)}\Delta\mathbf{c}^{(k)}$

end

4.4 Acceleration with approximation function

One difficulty with directly minimizing the original objective function $g(\mathbf{c})$ is the log-sum-exp term in the objective function. The DE-AM algorithm alternately minimizes the surrogate

function $g^{\mathrm{sur}}\big(\mathbf{c} : \hat{\mathbf{c}}^{(k)}\big)$, which upper-bounds the original objective function and approximates it in the nearby region of the current estimates $\hat{\mathbf{c}}$. However, in Section 4.2 we showed that the surrogate function is a very poor approximation of the objective function in some directions and leads to slow convergence.

In Jensen's inequality (B.14), if the distribution of the random variables is concentrated, the decomposition gap $\mathbb{E}\big[f(\boldsymbol{\tau})\big] - f\big(\mathbb{E}[\boldsymbol{\tau}]\big)$ is relatively small and it is possible to use $f\big(\mathbb{E}[\boldsymbol{\tau}]\big)$ as an approximation of $\mathbb{E}\big[f(\boldsymbol{\tau})\big]$.

Using this as motivation, we compute an approximation of the data model in the nearby region of the current estimate $\hat{\mathbf{c}}^{(k)}$ as

$$
\begin{aligned}
Q_j(y) &= \sum_E I_{0,j}(y)\Psi_j(y, E)\exp\Big(-\sum_x h(y|x)\sum_i \mu_i(E)c_i(x)\Big) \\
&= \hat{Q}_j^{(k)}(y)\sum_E \frac{\hat{q}_j^{(k)}(y, E)}{\hat{Q}_j^{(k)}(y)}\exp\Big(-\sum_x h(y|x)\sum_i \mu_i(E)\big(c_i(x) - \hat{c}_i^{(k)}(x)\big)\Big) \\
&\approx \hat{Q}_j^{(k)}(y)\exp\Big(-\sum_E \frac{\hat{q}_j^{(k)}(y, E)}{\hat{Q}_j^{(k)}(y)}\sum_x h(y|x)\sum_i \mu_i(E)\big(c_i(x) - \hat{c}_i^{(k)}(x)\big)\Big) \\
&= \tilde{Q}_j\big(y : \hat{\mathbf{c}}^{(k)}\big).
\end{aligned}
\tag{4.23}
$$

Letting

$$
\hat{\xi}_{i,j}^{(k)}(y) = \sum_E \frac{\hat{q}_j^{(k)}(y, E)}{\hat{Q}_j^{(k)}(y)}\mu_i(E),
\tag{4.24}
$$

then (4.23) can be rewritten as

$$
\tilde{Q}_j\big(y : \hat{\mathbf{c}}^{(k)}\big) = \hat{Q}_j^{(k)}(y)\exp\Big(-\sum_x h(y|x)\sum_i \hat{\xi}_{i,j}^{(k)}(y)\big(c_i(x) - \hat{c}_i^{(k)}(x)\big)\Big).
\tag{4.25}
$$

66

An approximation of the objective function is then generated as the I-divergence between the measurement $d_j(y)$ and the approximate data model $\tilde{Q}_j(y : \hat{\mathbf{c}}^{(k)})$ instead of the exact data model $Q_j(y)$ as

$$
\begin{aligned}
g^{\mathrm{apx}}\big(\mathbf{c} : \hat{\mathbf{c}}^{(k)}\big) &= d_I\big(\mathbf{d} \,\|\, \tilde{\mathbf{Q}} : \hat{\mathbf{c}}^{(k)}\big) \\
&= \sum_j \sum_y \Bigg[-d_j(y) \ln \Bigg(\hat{Q}_j^{(k)}(y) \exp\Bigg(-\sum_x h(y|x) \sum_i \hat{\xi}_{i,j}^{(k)}(y)\big(c_i(x) - \hat{c}_i^{(k)}(x)\big) \Bigg) \Bigg) \\
&\qquad + \hat{Q}_j^{(k)}(y) \exp\Bigg(-\sum_x h(y|x) \sum_i \hat{\xi}_{i,j}^{(k)}(y)\big(c_i(x) - \hat{c}_i^{(k)}(x)\big) \Bigg) \Bigg] \\
&= \sum_j \sum_y \Bigg[-d_j(y) \ln \big(\hat{Q}_j^{(k)}(y) \big) + d_j(y) \Bigg(\sum_x h(y|x) \sum_i \hat{\xi}_{i,j}^{(k)}(y)\big(c_i(x) - \hat{c}_i^{(k)}(x)\big) \Bigg) \\
&\qquad + \hat{Q}_j^{(k)}(y) \exp\Bigg(-\sum_x h(y|x) \sum_i \hat{\xi}_{i,j}^{(k)}(y)\big(c_i(x) - \hat{c}_i^{(k)}(x)\big) \Bigg) \Bigg].
\end{aligned}
\tag{4.26}
$$

It should be noted that the approximation function $g^{\mathrm{apx}}\big(\mathbf{c} : \hat{\mathbf{c}}^{(k)}\big)$ is not guaranteed to be an upper bound of the original objective function $g(\mathbf{c})$. However, it is very close to the original objective function in the nearby region of $\hat{\mathbf{c}}^{(k)}$ and is a much better approximation than the surrogate function (as shown in Figure 4.7 compared to Figure 4.6).

Empirically, minimization of $g^{\mathrm{apx}}\big(\mathbf{c} : \hat{\mathbf{c}}^{(k)}\big)$ would result in a decrease of $g(\mathbf{c})$ whenever $\hat{\mathbf{c}}^{(k)}$ is not too far away from the optimal point of $g(\mathbf{c})$.[3] Figure 4.8 compares the values of the objective function at the optimal points of the surrogate function and the approximation function compared to the initial objective function, i.e.,

$$
\log_{10}\left(\frac{g\Big(\underset{\mathbf{c}}{\mathrm{argmin}}\, g^{\mathrm{tp}}\big(\mathbf{c} : \mathbf{c}^{(0)}\big) \Big)}{g\big(\mathbf{c}^{(0)}\big)} \right), \quad \mathrm{tp} \in \{\mathrm{sur}, \mathrm{apx}\}.
\tag{4.27}
$$
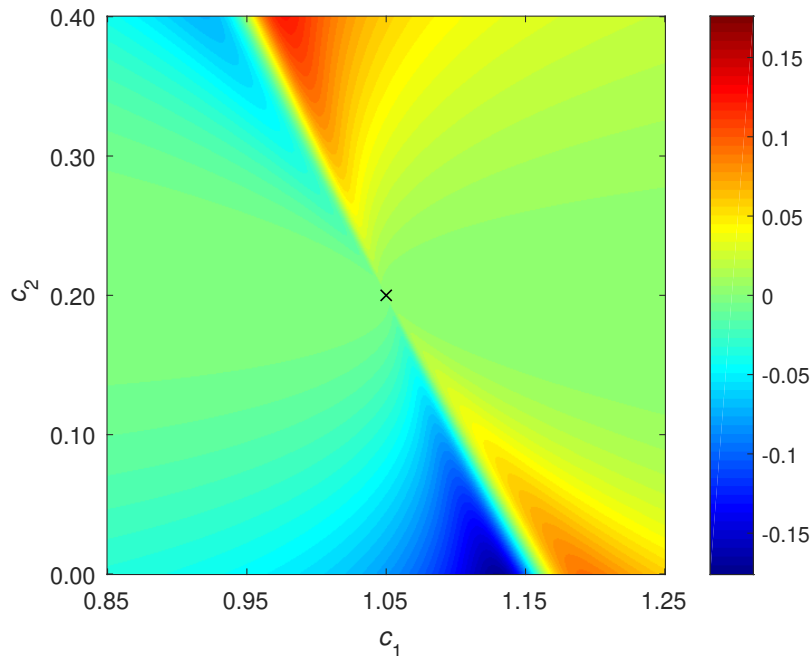
Figure 4.7: The common logarithm (base 10) of the ratio of the centered approximation function relative to the original objective function, $\log_{10}\left(g^{\mathrm{apx}}(\mathbf{c}:\mathbf{c}^*)/g(\mathbf{c})\right)$, for the reduced problem.

The result suggests that, in a relatively large region near the optimal point, the minimization of the approximation function decreases the value of the original objective function by a factor greater than 10 times of that achieved by minimizing the surrogate function, while both functions have relatively poor performance along the valley direction of the objective function.

Therefore, at each iteration k, we minimize the approximation function $g^{\mathrm{apx}}(\mathbf{c}:\hat{\mathbf{c}}^{(k)})$ instead of the surrogate function $g^{\mathrm{sur}}(\mathbf{c}:\hat{\mathbf{c}}^{(k)})$, which would empirically achieve much faster convergence than the minimization of the surrogate function.

[3]In practice, FBP reconstructed images, which are generally not far away from the optimal images, are used as the initial estimate.
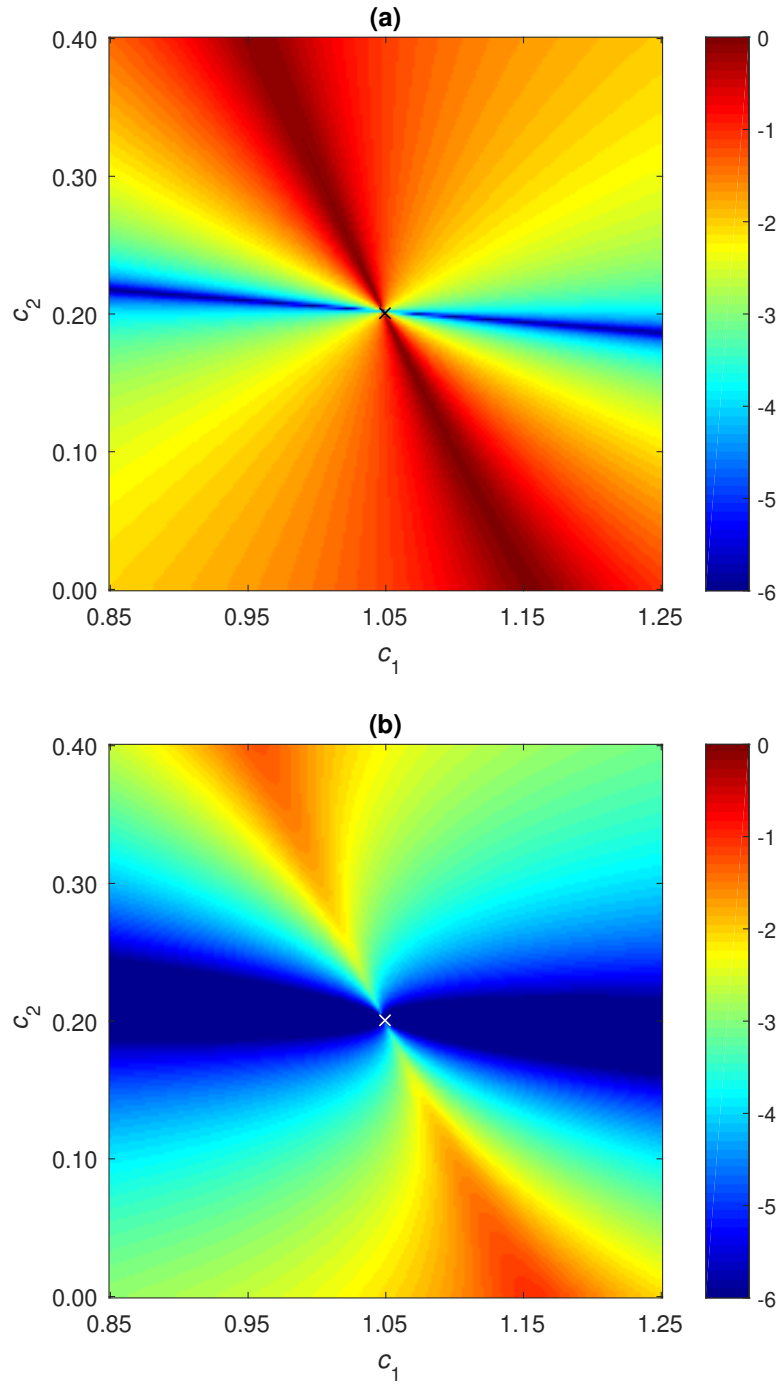
Figure 4.8: The common logarithm (base 10) of the ratio of the objective function $g(\mathbf{c})$ at the optimal point of (a) the surrogate function $g^{\text{sur}}(\mathbf{c} : \mathbf{c}^{(0)})$ and (b) the approximation function $g^{\text{apx}}(\mathbf{c} : \mathbf{c}^{(0)})$ relative to the that at the initial point $\mathbf{c}^{(0)}$ as a function of the initial point.

Similar to Section 4.3, the approximate function is further decoupled as

$$
\begin{aligned}
g^{\mathrm{apx}}&\left(\mathbf{c} : \hat{\mathbf{c}}^{(k)}\right)\\
&= \sum_{j}\sum_{y}\sum_{x}\left[d_j(y)\sum_i \xi_{i,j}^{(k)}(y)c_i(x)\right.\\
&\qquad\left. + \hat{Q}_j^{(k)}(y)\exp\left(-\sum_x \frac{h(y|x)}{z_0(x,y)}z_0(x,y)\sum_i \hat{\xi}_{i,j}^{(k)}(y)\big(c_i(x)-\hat{c}_i^{(k)}(x)\big)\right)\right] + C\\
&\le \sum_{x}\sum_{j}\sum_{y}\left[d_j(y)h(y|x)\sum_i \hat{\xi}_{i,j}^{(k)}(y)c_i(x)\right.\\
&\qquad\left. + \hat{Q}_j^{(k)}(y)\frac{h(y|x)}{z_0(x,y)}\exp\left(-z_0(x,y)\sum_i \hat{\xi}_{i,j}^{(k)}(y)\big(c_i(x)-\hat{c}_i^{(k)}(x)\big)\right)\right] + C\\
&= \breve{g}^{\mathrm{apx}}\left(\mathbf{c} : \hat{\mathbf{c}}^{(k)}\right)\\
&= \sum_{x}\breve{g}_x^{\mathrm{apx}}\left(\mathbf{c}(x) : \hat{\mathbf{c}}^{(k)}(x)\right).
\end{aligned}
\tag{4.28}
$$

The gradient $\nabla\breve{g}_x^{\mathrm{apx}}(x) = \begin{bmatrix}\nabla_1(x)\\\nabla_2(x)\end{bmatrix}$ and the Hessian matrix $\nabla^2\breve{g}_x^{\mathrm{apx}}(x) = \begin{bmatrix}\nabla_{1,1}^2(x) & \nabla_{1,2}^2(x)\\\nabla_{2,1}^2(x) & \nabla_{2,2}^2(x)\end{bmatrix}$
are given by

$$
\begin{aligned}
\nabla_i(x) &= \frac{\partial}{\partial c_i(x)}\breve{g}_x^{\mathrm{apx}}\left(\mathbf{c}(x) : \hat{\mathbf{c}}^{(k)}(x)\right)\Big|_{\mathbf{c}(x)=\hat{\mathbf{c}}^{(k)}(x)}\\
&= \sum_{y}h(y|x)\sum_j\left[d_j(y)\hat{\xi}_{i,j}^{(k)}(y) - \hat{Q}_j^{(k)}(y)\hat{\xi}_{i,j}^{(k)}(y)\right]\\
&= \sum_{y}h(y|x)\left[\sum_j\sum_E \hat{p}_j^{(k)}(y,E)\mu_i(E) - \sum_j\sum_E \hat{q}_j^{(k)}(y,E)\mu_i(E)\right]
\end{aligned}
\tag{4.29}
$$

and

$$\nabla^2_{i,i'}(x) = \frac{\partial^2}{\partial c_i(x)\partial c_{i'}(x)}\breve{g}_x^{\mathrm{apx}}\big(\mathbf{c}(x) : \hat{\mathbf{c}}^{(k)}(x)\big)\Big|_{\mathbf{c}(x)=\hat{\mathbf{c}}^{(k)}(x)}$$

$$= \sum_y h(y|x)z_0(x,y)\sum_j \hat{Q}_j^{(k)}(y)\hat{\xi}_{i,j}^{(k)}(y)\hat{\xi}_{i',j}^{(k)}(y) \tag{4.30}$$

$$= \sum_y h(y|x)z_0(x,y)\sum_j \frac{\left[\sum_E \hat{q}_j^{(k)}(y,E)\mu_i(E)\right]\left[\sum_E \hat{q}_j^{(k)}(y,E)\mu_{i'}(E)\right]}{\hat{Q}_j^{(k)}(y)},$$

respectively.

The decoupled approximate function $\breve{g}_x^{\mathrm{apx}}(\mathbf{c} : \hat{\mathbf{c}}^{(k)})$ also has the same gradient as the original objective function $g(\mathbf{c})$ at $\mathbf{c} = \hat{\mathbf{c}}^{(k)}$, i.e.,

$$\nabla g\big(\hat{\mathbf{c}}^{(k)}\big) = \nabla g^{\mathrm{apx}}\big(\hat{\mathbf{c}}^{(k)} : \hat{\mathbf{c}}^{(k)}\big) = \nabla\breve{g}^{\mathrm{apx}}\big(\hat{\mathbf{c}}^{(k)} : \hat{\mathbf{c}}^{(k)}\big). \tag{4.31}$$

Therefore, the Newton direction of the decoupled approximate function $\breve{g}_x^{\mathrm{apx}}(\mathbf{c} : \hat{\mathbf{c}}^{(k)})$ is a descent direction of the original objective function $g(\mathbf{c})$.

The iterative algorithm is shown below.

Algorithm 2: Accelerated DE-AM algorithm #2

Pre-compute $z_0(x,y) = \sum_{x'} h\left(y|x'\right)$

Initialize $c_i^{(0)}(x)$

Select $\alpha \in (0,1)$

for $k = 0,\ 1,\ 2,\ \ldots$ **do**

    foreach $y,\ j,\ E$ **do**

$$\hat{q}_j^{(k)}(y,E) = I_{0,j}(y)\Psi_j(y,E)\exp\left(-\sum_x h(y|x)\sum_i \mu_i(E)c_i^{(k)}(x)\right)$$

$$\hat{p}_j^{(k)}(y,E) = d_j(y)\frac{\hat{q}_j^{(k)}(y,E)}{\sum_{E'}\hat{q}_j^{(k)}(y,E')}$$

    end

    foreach x **do**

        Compute $\nabla \breve{g}_x^{\mathrm{apx}}(x)$ and $\nabla^2 \breve{g}_x^{\mathrm{apx}}(x)$ by (4.29) and (4.30)

        Compute the Newton direction $\Delta \mathbf{c}^{(k)}(x) = -\left[\nabla^2 \breve{g}_x^{\mathrm{apx}}(x)\right]^{-1}\left[\nabla \breve{g}_x^{\mathrm{apx}}(x)\right]$

    end

    Choose the maximum step size $t^{(k)} = t \in (0,1]$ that satisfies

$$g\left(\hat{\mathbf{c}}^{(k)} + t\Delta\mathbf{c}^{(k)}\right) \leq g\left(\hat{\mathbf{c}}^{(k)}\right) + \alpha t\left[\nabla g\left(\hat{\mathbf{c}}^{(k)}\right)\right]^{\mathsf{T}}\Delta\mathbf{c}^{(k)}$$

    Update $\hat{\mathbf{c}}^{(k+1)} = \hat{\mathbf{c}}^{(k)} + t^{(k)}\Delta\mathbf{c}^{(k)}$

end

4.5 Simulation result

A virtual mini CT geometry with 116 detectors and 600 source views per rotation was used to evaluate these algorithms. The image size was 80×80 with pixel size $1\,\mathrm{mm} \times 1\,\mathrm{mm}$. The ground truth of the component images is shown in Figure 4.9. The four inserts were selected to imitate muscle, cortical bone, adipose tissue and femur bone (clockwise from the top),
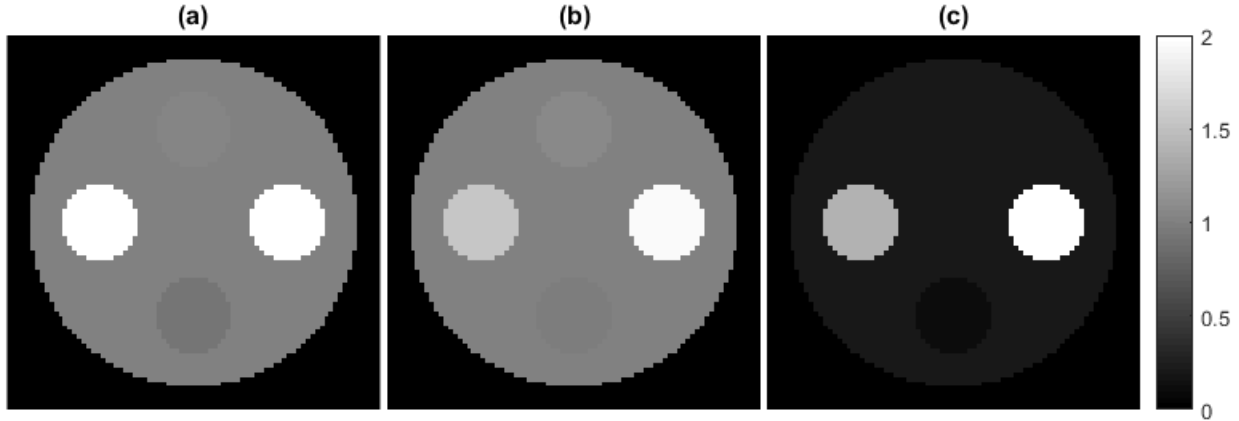
Figure 4.9: True component images of the virtual phantom used for the mini CT scanner geometry: (a) $c_0(x)$, (b) $c_1(x)$, and (c) $c_2(x)$.

while the background was set as water. The tube potentials were set to $90/140\,\mathrm{kVp}$ and $140\,\mathrm{kVp}$ for the dual-energy case and the single-energy case, respectively.

A noise-free case and a Poisson noise case were considered for dual-energy joint reconstruction. The sinogram noise level was chosen for tube exposures of $250\,\mathrm{mAs}$ and $75\,\mathrm{mAs}$ for $90\,\mathrm{kVp}$ and $140\,\mathrm{kVp}$, respectively. All simulated data were generated with no modeling error (i.e., the synthetic sinograms were generated from true $\mathbf{c}_i$ images). The sinogram-domain decomposition results via FBP reconstruction were used as the initial images for all algorithms.

Figure 4.10 shows the objective functions of the original DE-AM algorithm and the two accelerated modifications as a function of iteration numbers. Figure 4.11 and Figure 4.12 show the corresponding RMS errors of the two component images for selected numbers of iterations. Note that the RMS errors are not monotonically decreasing because they are not the goal of the minimization problem. The result suggests that the three algorithms follow difference trajectories of the estimates from the initial point to the optimal point.

After enough iterations, all three algorithms converge to the same solution. The original DE-AM algorithm, however, requires more than 10^5 iteration to converge for this mini CT geometry. The accelerated DE-AM algorithm #1 dramatically accelerates the convergence compared to the original DE-AM algorithm. The accelerated DE-AM algorithm #2 achieves the best performance among the three algorithms, which requires approximately only 1/100 and 1/5 of iterations, compared with the original DE-AM algorithm and the accelerated DE-AM algorithm #1, respectively, to achieve the same level of convergence.

Comparing Figure 4.10 with Figure 4.1, it can be seen that the accelerated DE-AM algorithm #2 accounts for the factors discussed in Section 4.2 that limit the speed of the original DE-AM algorithm and achieves convergence almost as fast as the M-SE-AM algorithm.
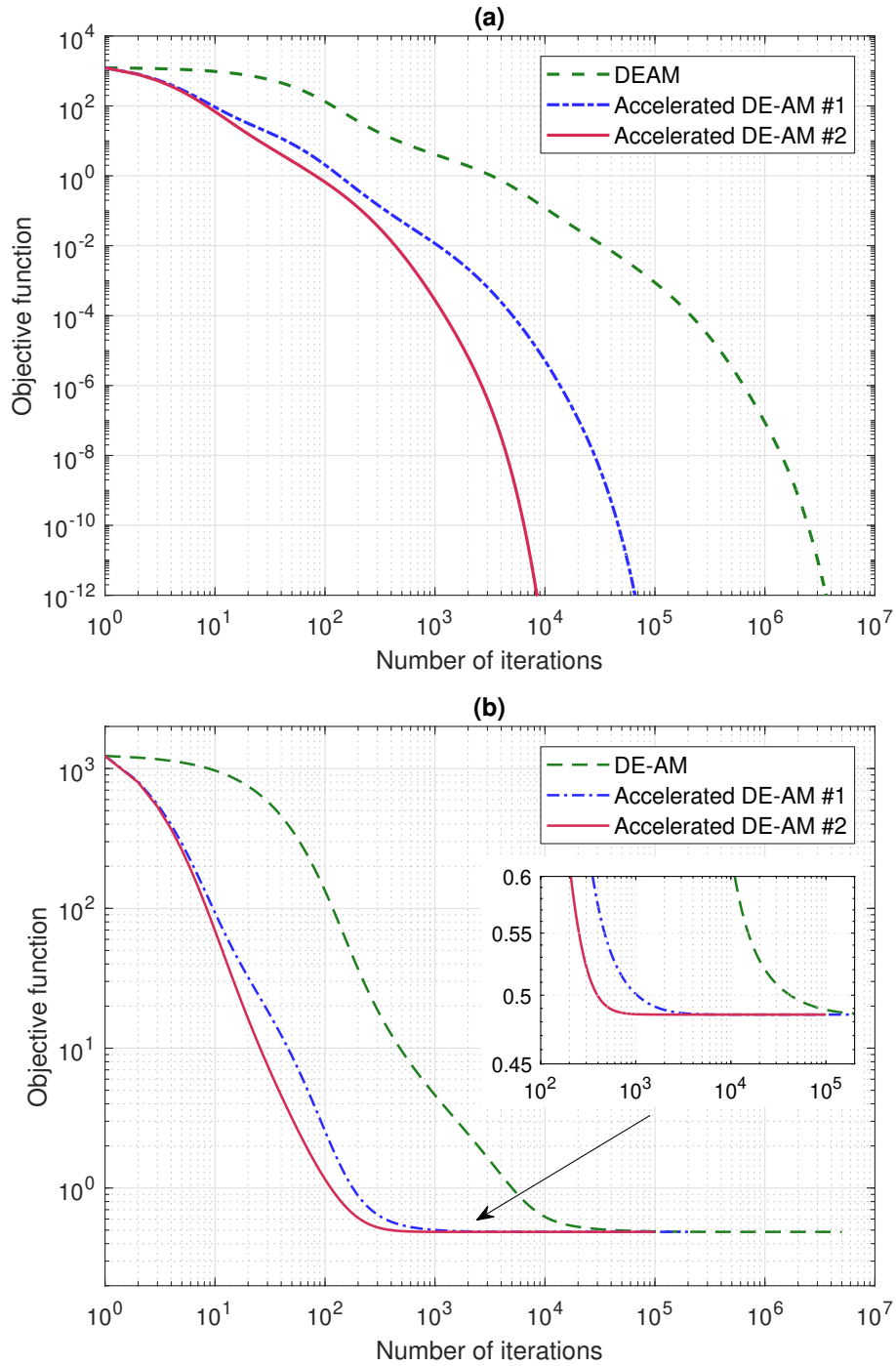
Figure 4.10: Objective function values as a function of iteration numbers for different reconstructions of (a) noise-free sinograms and (b) sinograms with Poisson noise.
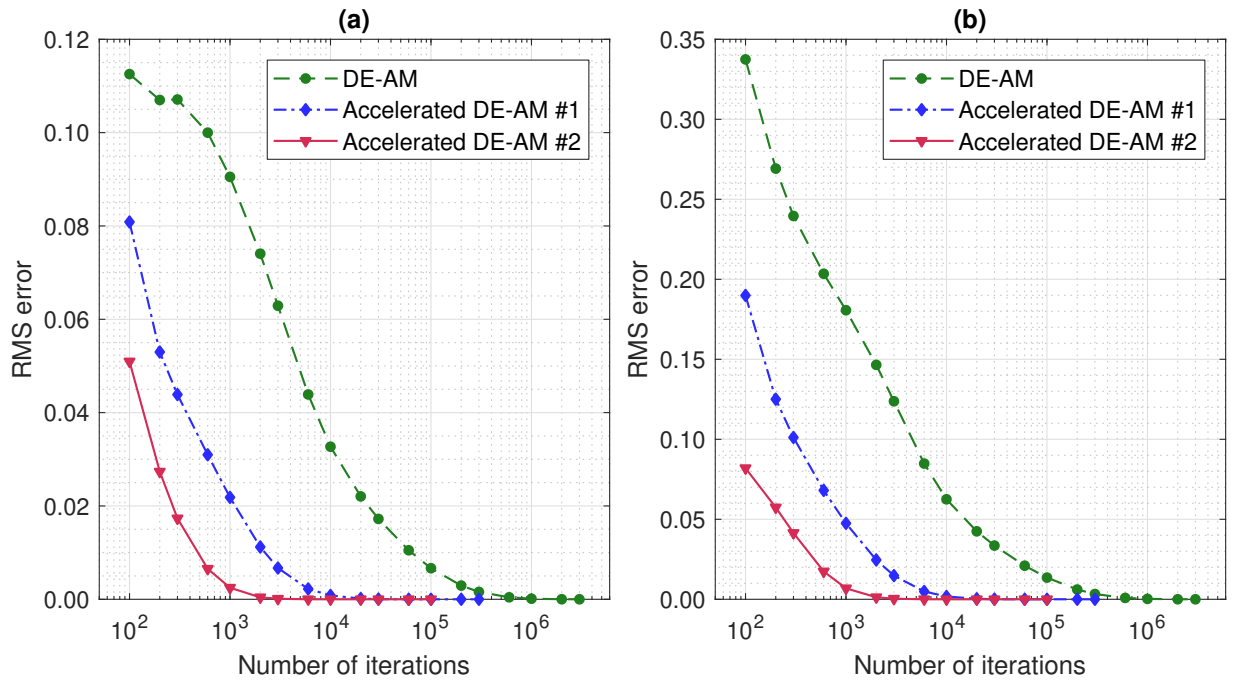
Figure 4.11: The RMS errors of (a) $c_1(x)$ and (b) $c_2(x)$ as a function of iteration numbers for different reconstructions of noise-free sinograms.
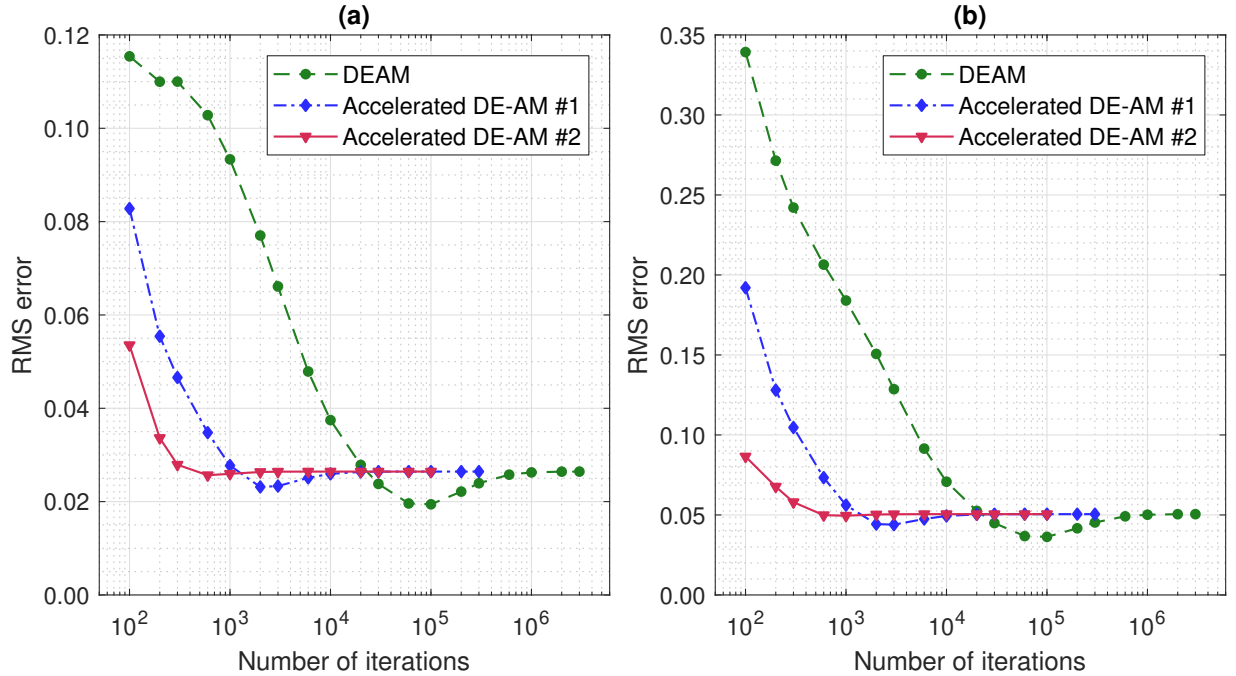
Figure 4.12: The RMS errors of (a) $c_1(x)$ and (b) $c_2(x)$ as a function of iteration numbers for different reconstructions of sinograms with Poisson noise.

Chapter 5

Performance of the JSIR-BVM method: compared to image- and sinogram-domain decomposition methods

In this chapter, the performance of the BVM-JSIR method is evaluated and compared with image- and sinogram-domain decomposition methods in a simulation framework. Three different DECT-SPR models including the BVM are implemented to fairly compare different reconstruction and decomposition techniques.[1]

5.1   Virtual CT scanner setup

The proprietary geometry of the Philips Brilliance Big Bore scanner (Philips Medical Systems, Cleveland, OH), which was the one used for our experiments (see Chapter 6), was

---

[1]Part of this chapter is based on Zhang *et al.* [85].
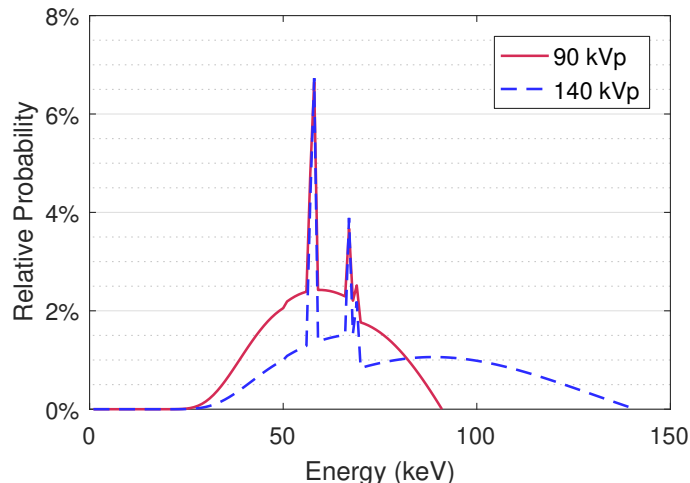
Figure 5.1: The normalized central-axis energy-fluence spectra of the DECT scans used in theoretical computations and simulations.

used to generate the synthetic sinograms of the virtual phantom and patient. The sinograms were generated with 816 detectors in the detector row and 1320 source views per rotation, which corresponds to the ultra-fast mode of the Philips Brilliance Big Bore CT scanner. All generated synthetic sinograms were scatter-free.

The DECT source spectra, $\Phi_{0,j}(E)$, were computed by the Birch-Marshall model [86] for 90 kVp and 140 kVp tube potentials with 12 mm of equivalent Al filtration and were mathematically hardened using the known geometry and density of the Teflon$^{\text{TM}}$ bow-tie filter giving rise to the detector-dependent spectra, $\Phi_j(y, E)$. The detector-response function, $D(E)$, was generated for the detectors of the Philips Brilliance Big Bore scanner. The simulated spectra were chosen to imitate the typical spectra of the actual scanner. Figure 5.1 shows the simulated energy-fluence spectra at the central axis of the virtual scanner, which were also used to evaluate the theoretical accuracy of different DECT-SPR models.

For all calibration-based methods, The Gammex RMI 467 tissue characterization phantom (Gammex, Middleton, WI), which contains 13 tissue substitutes, was used for the calibration process. The exact densities and elemental compositions of calibration materials were assumed to be known in the calibration process.

5.2 Photon linear attenuation coefficient modeling accuracy

The BVM component weights of the reference human tissues were computed via (3.26) and then used to reproduce the energy-dependent photon linear attenuation coefficients via (3.1). Figure 5.2 shows the prediction error within the typical energy range of CT x-ray sources for 12 selected reference tissues that are representative of the reference tissue set. As the result shows, the BVM is able to reproduce the linear attenuation coefficients of typical tissues within 1.5% for photon energy higher than 25 keV. For lower energies, the modeling error is larger. Because there are almost no incident photons of energy below 30 keV, it is fundamentally difficult to accurately predict the linear attenuation coefficients for such low energies from the DECT measurements.

It should be noted that among all the reference human tissues listed in Appendix A, the thyroid is difficult to model for most CT-based techinques [11, 15, 73]. This is because the thyroid contains 0.1% of iodine, whose atomic number ($Z = 53$) is much higher than the atomic number of typical elements found in tissues ($2 \leq Z \leq 20$). The iodine presents a K-edge at 33.2 keV,[2] which is within the energy range of CT scans. As a result, it is impossible to accurately approximate its linear attenuation coefficient using basis materials that are chosen for typical tissue composition. Figure 5.3 shows the attenuation coefficient
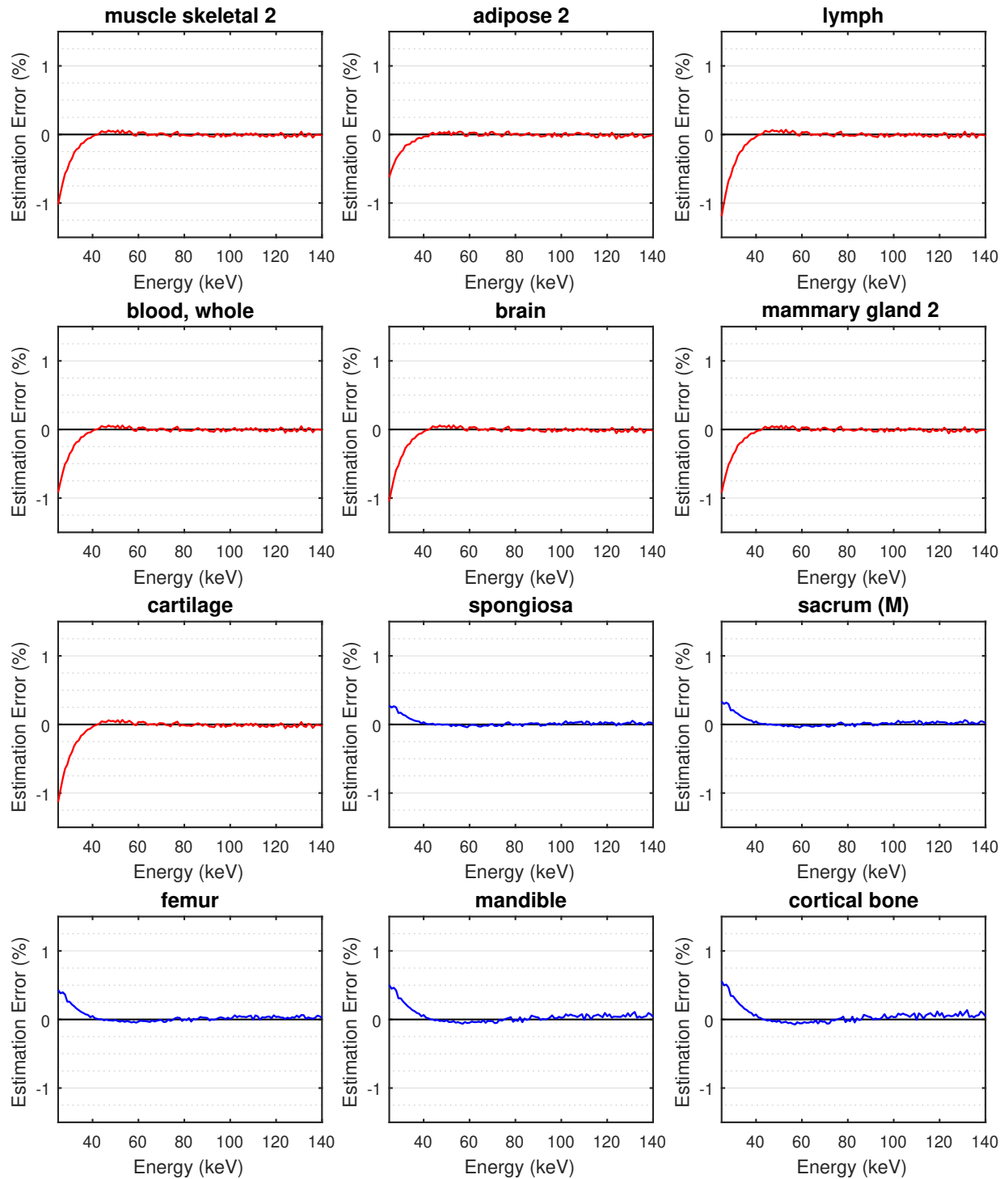
Figure 5.2: Theoretical BVM modeling errors for photon linear attenuation coefficients of the reference human tissues between 25 keV and 140 keV, shown as the residual errors relative to the reference values.
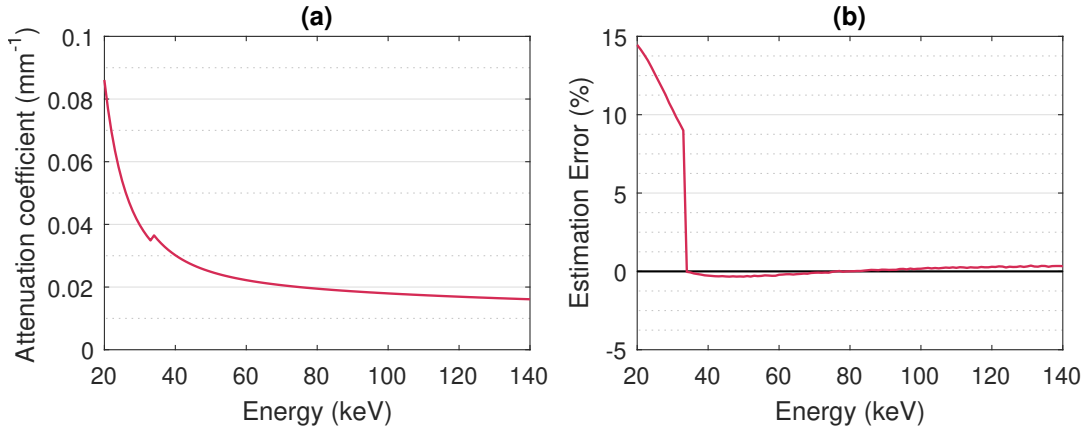
Figure 5.3: (a) Photon linear attenuation coefficient of thyroid and (b) the corresponding BVM modeling error between 20 keV and 140 keV.

curve of the reference thyroid tissue and the corresponding modeling error derived by the BVM. The residual modeling error is similar to that of other tissue compositions above the K-edge energy, while the modeling error exceeds 10% for energies below the K-edge energy. The thyroid tissue is also found to be the worst case in the BVM-based technique for proton stopping power estimation. Therefore, it may require additional correction for CT scans that contain the thyroid region.

5.3 Proton SPR modeling accuracy

The accuracy with which the BVM, as well as the Hünemohr and Bourque ρ_e-Z_{eff} models, reproduce proton stopping powers was tested by comparing the theoretical model predictions against the computed ground truth for the tabulated mass densities and element compositions of the reference human tissues.

[2]The probability of photoelectric absorption significantly increases when the photon energy is slightly higher than the K-shell binding energy of the material due to the ejection of the K-shell electron.

For the BVM, the electron densities and mean excitation energies were predicted from the BVM component weights via (3.2) and (3.5).

To evaluate the Hünemohr model and the Bourque model, the theoretical CT numbers were calculated by taking the average over the known x-ray spectrum as

$$\mathrm{HU}_j = 1000 \left(\frac{\int_E \Psi_j(E) \mu(E) \, \mathrm{d}E}{\int_E \Psi_j(E) \mu_\mathrm{w}(E) \, \mathrm{d}E} - 1 \right) , \tag{5.1}$$

where $\mu(E)$ and $\mu_\mathrm{w}(E)$ are the linear attenuation coefficients of the scanned material and water, respectively. The calibration parameters were determined by using the calculated CT numbers of the Gammex RMI 467 phantom materials and were then applied to the calculated CT numbers of the reference human tissues.

Figures 5.4–5.6 show the residual prediction error for each of the three two-parameter DECT-SPR models for reference humans tissues listed in Appendix A.[3] The minimum, maximum, absolute-mean, and RMS of the modeling errors are summarized in Table 5.1.

All three models show comparable modeling accuracy under idealized conditions with no CT image-formation uncertainties. The electron-density estimation errors are within 0.2% for all tissues with the exception of the thyroid tissue. The predicted SPRs of all tissue types are within 0.5% of the reference values and the RMS errors are less than 0.2%. The result is consistent with the literature, which has shown that most currently available DECT models support relatively low intrinsic SPR prediction errors with 0.16% to 0.41% RMS errors for general human tissues [13, 52]. However, it should be noted that such high accuracy may not be achievable due to the aforementioned image-formation uncertainties and other related uncertainties.

---

[3]The deflated lung is not shown because it has the same composition as the inflated lung, and therefore has the same theoretical modeling error.
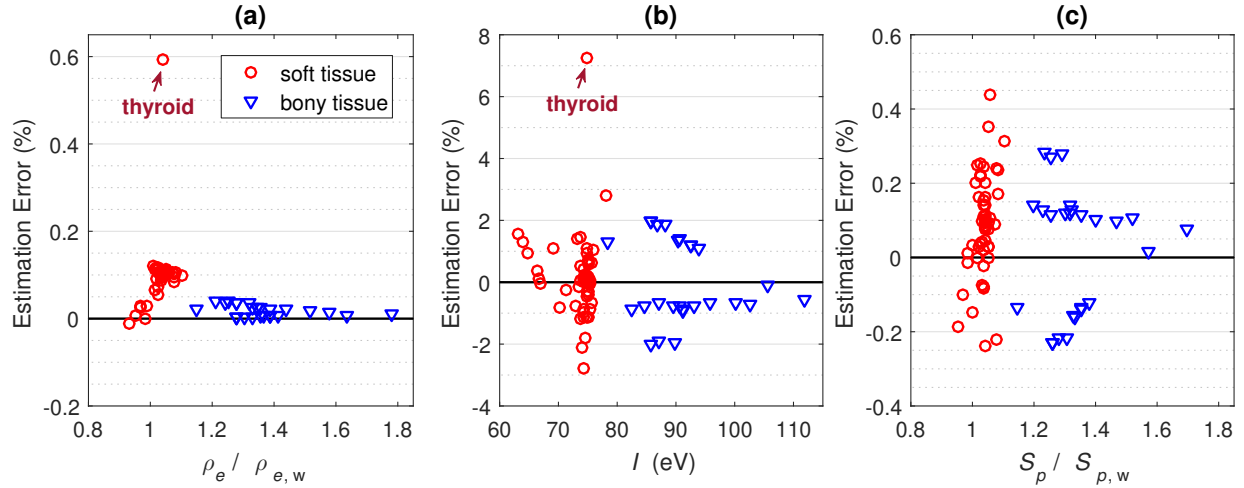
Figure 5.4: Theoretical modeling errors of the BVM for (a) electron density, (b) mean excitation energy, and (c) proton SPR at 200 MeV of the reference human tissues, shown as the residual errors relative to the reference values.
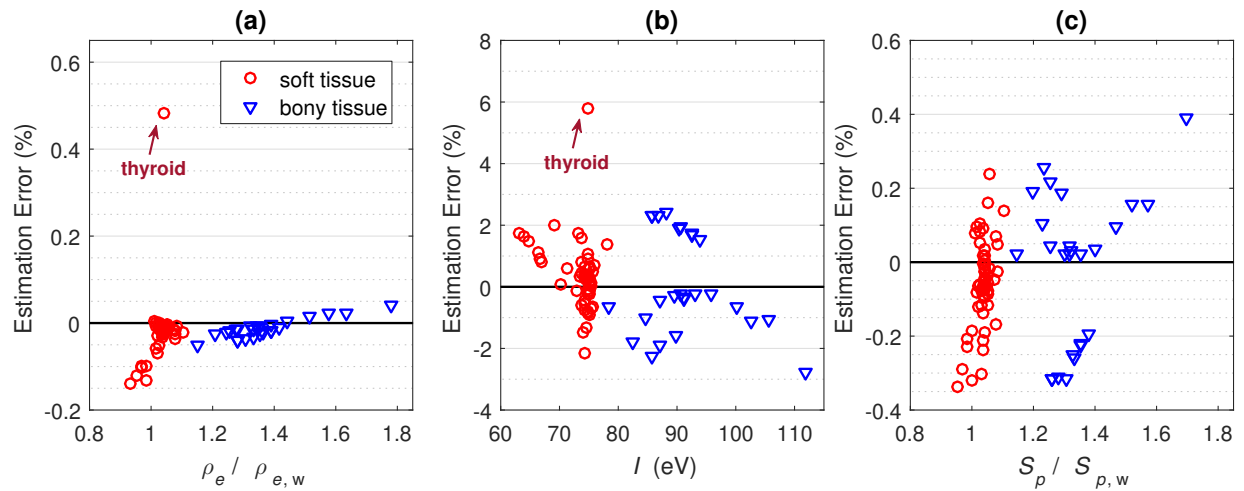
Figure 5.5: Theoretical modeling errors of the Hünemohr model for (a) electron density, (b) mean excitation energy, and (c) proton SPR at 200 MeV of the reference human tissues, shown as the residual errors relative to the reference values.
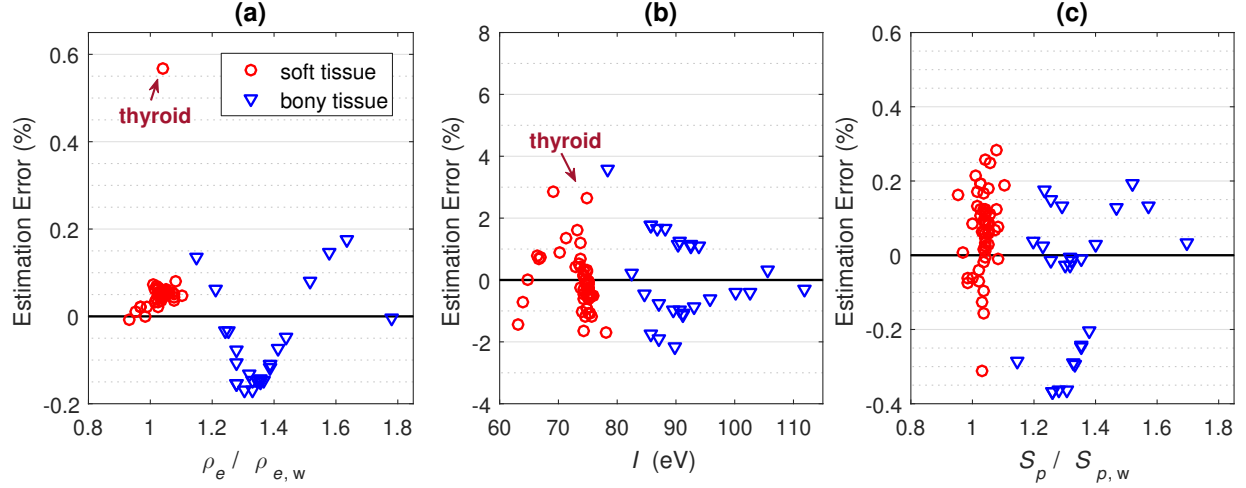
Figure 5.6: Theoretical modeling errors of the Bourque model for (a) electron density, (b) mean excitation energy, and (c) proton SPR at 200 MeV of the reference human tissues, shown as the residual errors relative to the reference values.

Table 5.1: Statistics of the theoretical residual errors predicted using different DECT-SPR models.

| | Model | Relative estimation error (%) | | | |
		min	max	abs-mean	RMS
ρ_e	BVM	-0.01	0.59	0.08	0.10
	Hünemohr	-0.14	0.48	0.03	0.07
	Bourque	-0.17	0.57	0.08	0.10
Z_{eff}	BVM	$-$	$-$	$-$	$-$
	Hünemohr	-0.14	0.48	0.03	0.07
	Bourque	-0.10	0.02	0.01	0.02
I	BVM	-2.79	7.25	0.92	1.33
	Hünemohr	-2.78	5.81	0.95	1.30
	Bourque	-2.17	3.59	0.82	1.06
S_p	BVM	-0.24	0.44	0.14	0.16
	Hünemohr	-0.34	0.39	0.12	0.16
	Bourque	-0.37	0.28	0.12	0.16

The overall SPR modeling error can be divided into two parts: one is that of the reproduction of the material properties that can be directly determined from DECT data, i.e., the photon cross-section modeling parameters (ρ_e, Z_{eff}) or (ρ_e, r_c); and the other one is the I-value parameterization as an empirical function of Z_{eff} or r_c. It has been shown that one major SPR modeling uncertainty that is inherent to all DECT approaches is the uncertainty associated with the I-value parameterization [21], due to the lack of a one-to-one correspondence between photon cross-section modeling parameters and the I-value. Therefore, inappropriate I-value parameterization due to poor prior knowledge of the scanned object may introduce substaintial errors into the SPR prediction result of all DECT approaches [87].

It is believed that the elemental compositions of tissue may vary dramatically between different individuals and also for the same individual at different ages or in different health conditions. For examples, the fraction of lipid in adipose tissues gradually increases from approximately 35% for newborns to approximately 70% for adults on average [88]. The marrow tissue is nearly 100% red marrow in newborns, while the fraction of red marrow decreases to a range of 25% to 70% of total marrows for elderly males and especially approaches near zero in the medullary cavities of the long bones of adults [89]. Certain diseases may also significantly change the tissue compositions. For example, cirrhosis of the liver due to chronic alcoholism may cause the mass fraction of lipid in the liver to increase from approximately 5% to 19% [88,90].

To more comprehensively assess the inherent modeling uncertainties in the application for unknown patient tissue characterization, we followed the analysis by Han [52] that investigated the sensitivity of SPR estimates to the variations of human tissue composition. We varied the fraction of major components for three categories of human tissues: adipose-like tissue, muscle-like tissue, and trabecular bone. For adipose- and muscle-like tissues, the fraction of lipid, protein, and water were varied, while the compositions of ash and carbohydrate

Table 5.2: Variations in the component composition of soft and bony tissue.

	Adipose-like tissue	Muscle-like tissue	Trabecular bone
Protein[†]	$0-10$	$10-25$	
Lipid[†]	$30-88$	$0-12$	
Water[†]	$1.7-69.7$	$61.1-88.1$	
Carbohydrate[†]		1	
Ash[†]	0.3	0.9	
Osseous[†]			$20-70$
Red marrow[§]			$0-100$

[†] represented by the percentage mass fraction.
[§] represented by the percentage mass fraction in total marrow.

were kept constant. For trabecular bone tissues, the fraction of osseous tissue (modeled as cortical bone) and red/yellow marrows were varied. The range of component fractions shown in Table 5.2 was chosen to accommodate the large tissue variation reported in the literature [88, 91–93] in order to cover the extreme cases that may occur in practice.

Figures 5.7–5.9 show the SPR modeling error that is due only to the I-value parameterization error, which is computed as

$$
e = 100\% \cdot \left(\frac{k_2(200\,\mathrm{MeV}) - \ln\left(I_{\mathrm{par}}/\mathrm{eV}\right)}{k_2(200\,\mathrm{MeV}) - \ln\left(I_{\mathrm{ref}}/\mathrm{eV}\right)} - 1 \right) \tag{5.2}
$$

for the three investigated models, where the constant $k_2(200\,\mathrm{MeV})$ is given in Section 1.2.4, I_{ref} is the reference I-value computed via the Bragg additivity rule, and I_{par} is the I-value derived from the empirical parameterization function of Z_{eff} or r_c. In other words, the electron densities are assumed to have no error.

All three models achieve good modeling errors over a wide range of tissue compositions, while the Hünemohr model and the Bourque model may have some relatively large modeling errors in some cases. The absolute SPR error of the BVM due to I-value parameterization is
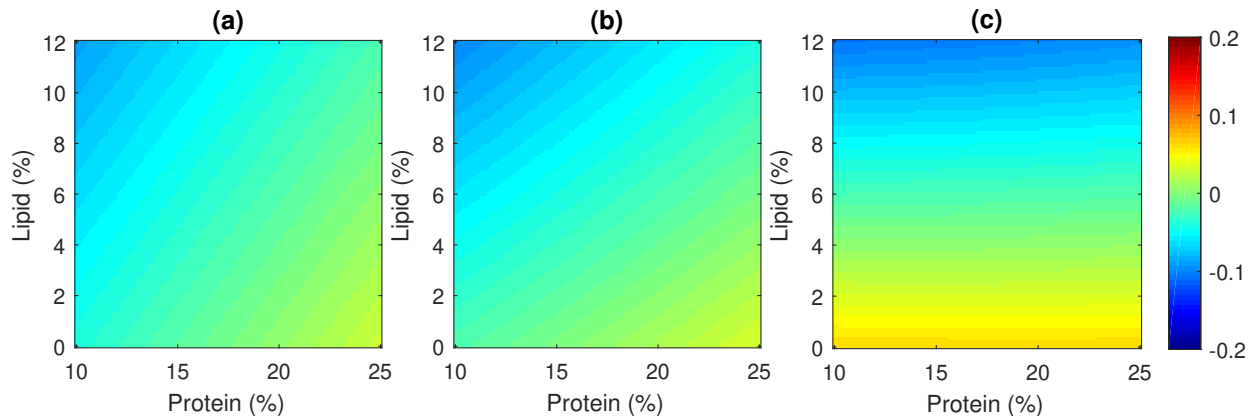
Figure 5.7: The percentage SPR error propagated from I-value parameterization error of (a) BVM, (b) Hünemohr model, and (c) Bourque model for muscle-like tissues.
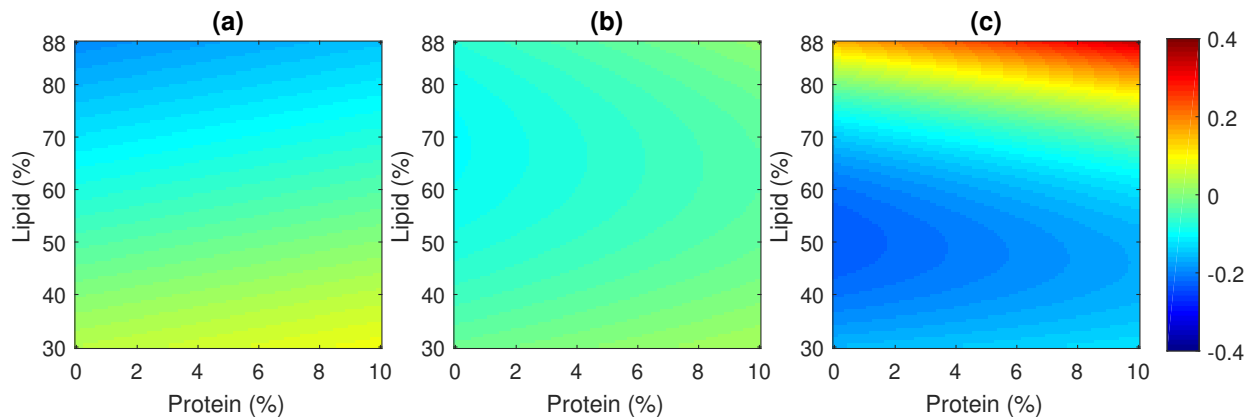
Figure 5.8: The percentage SPR error propagated from I-value parameterization error of (a) BVM, (b) Hünemohr model, and (c) Bourque model for adipose-like tissues.
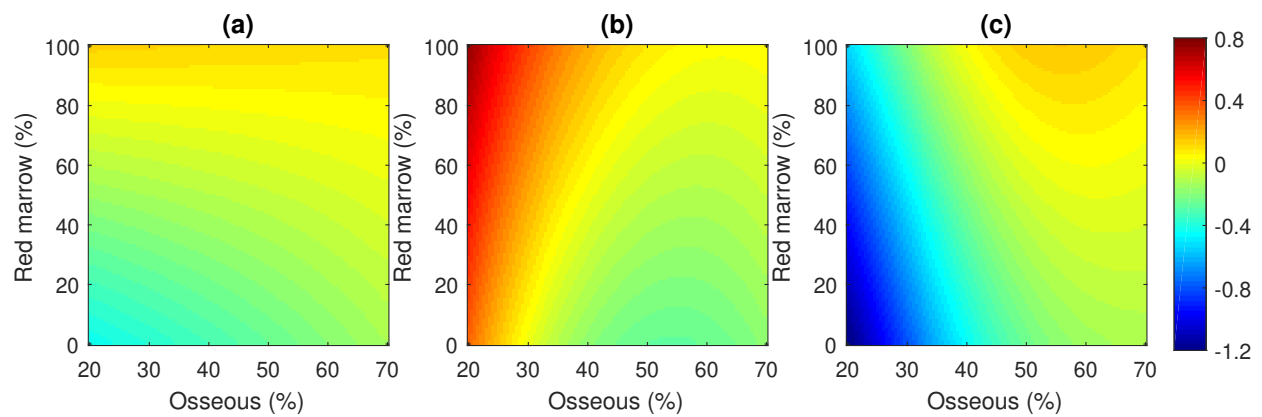
Figure 5.9: The percentage SPR error propagated from I-value parameterization error of (a) BVM, (b) Hünemohr model, and (c) Bourque model for trabecular bones.
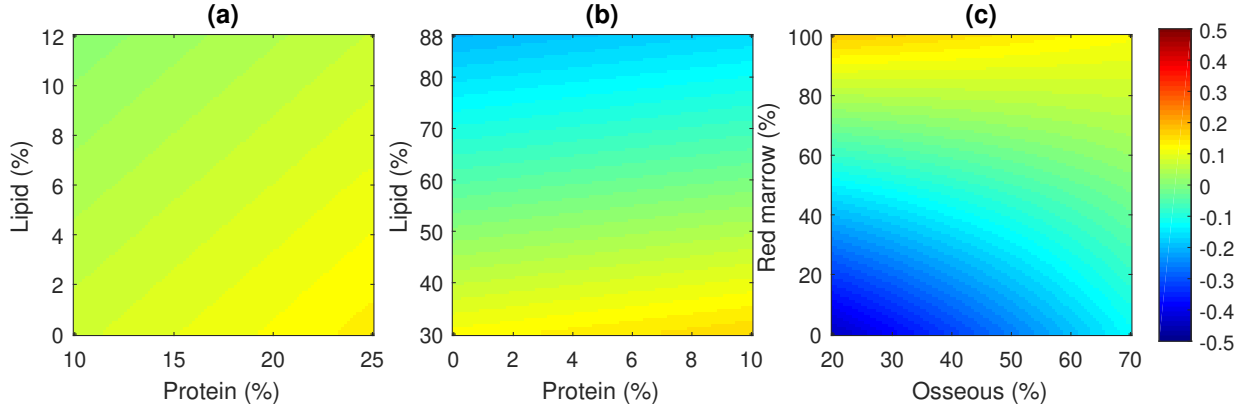
Figure 5.10: The percentage relative SPR error of of (a) muscle-like tissues, (b) adipose-like tissues, and (c) trabecluar bones predicted by BVM as a function of the composition variation.

less than 0.10%, 0.20%, and 0.45% for muscle-like, adipose-like, and trabecular bone tissues, respectively, over the investigated ranges of tissue composition variations in Table 5.2. The Hünemohr model achieves less than 0.11%, 0.11%, and 0.77% absolute errors for muscle-like, adipose-like, and trabecular bone tissues, respectively. The Bourque model achieves less than 0.11%, 0.35%, and 1.25% absolute errors for muscle-like, adipose-like, and trabecular bone tissues, respectively. Among all the three models, BVM is most robust to the tissue composition variations. The Bourque model is slightly more sensitive to tissue composition variations of adipose-like tissues. Both the Hünemohr model and Bourque model present approximately 1% errors for the trabecular bone with relatively low fraction of osseous tissue.

Figure 5.10 shows the overall SPR modeling error (i.e., contributions from both I-value parameterization error and ρ_e modeling error) of the BVM. The absolute modeling error is less than 0.13%, 0.21%, 0.45% for adipose-like, muscle-like, and trabecular bone. Moreover, comparison between Figure 5.10 and Figures 5.7–5.9 suggests that the I-value parameterization error dominates the overall SPR modeling error for the BVM. The result demonstrates that the BVM maintains good theoretical modeling accuracy over a wide range of component variations of typical human tissues.

5.4 Simulation of virtual phantoms

A series of synthetic sinograms were generated for virtual test phantoms containing 34 selected reference human tissues to evaluate the accuracy of different SPR mapping approaches and models in the presence of image noise and other uncertainties inherent in the CT reconstruction process. The geometry of the virtual phantoms was designed based on the Gammex RMI 467 phantom, which consists of a cylindrical solid water background of 330 mm diameter with 17 cylindrical inserts of 30 mm diameter (as shown in Figure 5.11). Two different phantom realizations were required to include all 34 selected tissue inserts. The standard Gammex tissue substitutes were used as the calibration materials for the Hünemohr method and the Bourque method in both the image- and sinogram-domain decomposition approaches, while a Gammex-like phantom with polystyrene and 23% $CaCl_2$ solution inserts was used for calibrating the BVM-based image-domain decomposition method. Table 5.3 lists the insert arrangements for these test and calibration phantoms. The ground truth images of the virtual phantoms are shown in Figure 5.12.

Noiseless sinograms that represent the ideal case of infinite source intensity were generated via (3.13). The sinogram measurement noise was modeled as Poisson random noise, while the effect of scattered radiation and spectrum alteration was neglected in this simulation analysis.

The simulated sinograms were processed using three distinct decomposition approaches: the image-domain, sinogram-domain, and JSIR approaches. Three DECT-SPR models were applied to the reconstruction results in both the image- and sinogram-domain decomposition approaches, while only the BVM was applied in the JSIR approach. Table 5.4 summarizes the seven methods that are investigated in this simulation study.
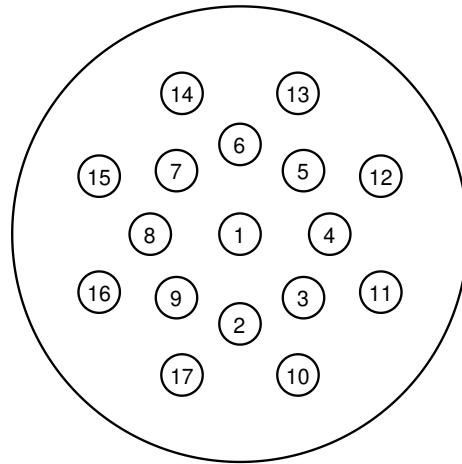
Figure 5.11: Illustration of the virtual phantom geometry.
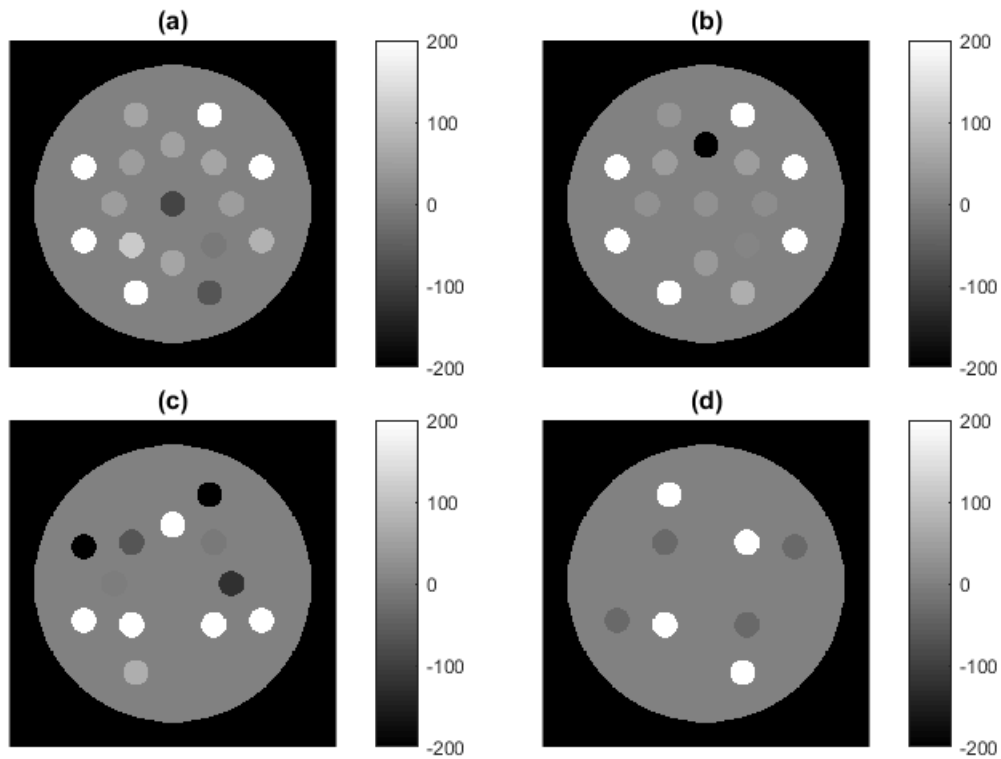
Figure 5.12: Ground truth monochromatic CT images (60 keV) of virtual phantoms: (a) tissue #1, (b) tissue #2, (c) Gammex, and (d) BVM-bases.

Table 5.3: Arrangement of inserts in the test and calibration phantoms. The insert locations inside the phantoms are shown in Figure 5.11.

No.	Tissue #1	Tissue #2	Gammex	BVM-bases
1	adipose 2	lymph	CT solid water	
2	blood, whole	brain	CT solid water	
3	breasts	cell nucleus	CB2 50% $CaCO_3$	polystyrene
4	eye lens	small intestine	AP6 adipose	
5	heart, blood filled	kidney 2	SR2 brain	$CaCl_2$ solution
6	liver 2	lung, deflated	SB3 cortical bone	
7	lung, inflated	muscle skeletal 2	BR12 breast	polystyrene
8	ovary	pancreas	water	
9	cartilage	red marrow	CB2 30% $CaCO_3$	$CaCl_2$ solution
10	yellow marrow	skin	CT solid water	$CaCl_2$ solution
11	thyroid	femur	IB3 inner bone	
12	cranium	mandible	CT solid water	polystyrene
13	humerus, total bone	sacrum (M)	LN300 lung	
14	spleen	testis	CT solid water	$CaCl_2$ solution
15	rib, 10th	rib, 2nd/6th	LN450 lung	
16	cortical bone	spongiosa	B200 mineral bone	polystyrene
17	vertebral, C4 ex.	vertebral, D6/L3 ex.	LV1 liver	

Table 5.4: Summary of investigated methods.

	Decomposition approach	DECT-SPR model	Calibration
imag-BVM	image-domain	BVM	Yes
imag-HM	image-domain	Hünemohr model	Yes
imag-BM	image-domain	Bourque model	Yes
sino-BVM	sinogram-domain	BVM	No
sino-HM	sinogram-domain	Hünemohr model	Yes
sino-BM	sinogram-domain	Bourque model	Yes
JSIR-BVM	joint SIR	BVM	No

All image reconstructions were processed with a pixel size of $1\,\mathrm{mm} \times 1\,\mathrm{mm}$ and a slice thickness of $3\,\mathrm{mm}$. For the image- and sinogram-domain decomposition methods, the images were reconstructed with a ramp filter modified by a $1.5\,\mathrm{mm}$ Gaussian kernel [94]. A water-based beam hardening correction [29, 30] was applied to each synthetic polychromatic sinogram before the single-energy reconstructions in the image-domain methods. For the JSIR-BVM method, the regularization parameters were set to $\delta = 0.01$ and $\lambda = 6$. These reconstruction parameters were selected to achieve similar resolutions from different reconstruction algorithms for typical soft tissue contrast ($75\,\mathrm{HU}$) in the $330\,\mathrm{mm}$ diameter phantom [94].

To quantify the accuracy of the predicted proton SPR image of these virtual test phantoms, relative SPR estimation error is evaluated for all pixels within a region of interest (ROI) of $24\,\mathrm{mm}$ diameter inside each homogeneous tissue insert and then the average estimation error is calculated for each tissue's ROI. The mean error over all ROI pixels, the RMS-of-mean error (i.e., RMS of the mean errors of each tissue), and RMS error over all ROI pixels are then computed as

$$e_{\mathrm{mean}} = \frac{1}{K} \sum_{k=1}^{K} \bar{e}_k = \frac{1}{KN} \sum_{k=1}^{K} \sum_{x \in R_k} e_x\,, \tag{5.3}$$

$$e_{\mathrm{RMS\text{-}of\text{-}mean}} = \left[\frac{1}{K} \sum_{k=1}^{K} (\bar{e}_k)^2 \right]^{\frac{1}{2}} = \left[\frac{1}{K} \sum_{k=1}^{K} \left(\frac{1}{N} \sum_{x \in R_k} e_x \right)^2 \right]^{\frac{1}{2}}\,, \tag{5.4}$$

$$e_{\mathrm{RMS}} = \left[\frac{1}{KN} \sum_{k=1}^{K} \sum_{x \in R_k} e_x^2 \right]^{\frac{1}{2}}\,, \tag{5.5}$$

where N is the number of pixels in each ROI, K is the number of tissue types, R_k is the ROI of the k-th tissue, e_x is the relative SPR estimation error at image pixel x, and $\bar{e}_k$ is the mean estimation error for the k-th tissue. The mean error shows the overall bias of the SPR estimates, while the RMS-of-mean error measures the variation of the systematic estimation

error for different tissues. The RMS error reflects the pixel-to-pixel variation in the SPR image.

5.4.1 Impact of reconstructed image intensity uncertainties

To address the performance of the investigated methods under different dose levels, the source intensities in the CT data model were varied in order to adjust the sinogram noise level, while keeping the relative source intensities of the low- and high-energy scans equal. The reference source intensity level (i.e., 100%) was set to 300 mAs for 90 kVp and 90 mAs for 140 kVp, respectively, which were chosen to reproduce the total volume CT dose index (CTDI$_{vol}$) typical of a single-energy diagnostic adult abdomen scan on the actual scanner. A low-noise case and a high-noise case were simulated with 200% and 50% source intensities, respectively. Additionally, noiseless sinograms were also included in the analysis to represent the ideal case of infinite source intensity.

Figure 5.13 shows the reconstructed CT images from the 100% source-intensity-level synthetic sinograms for the BVM-based image-domain, sinogram-domain, and JSIR methods. The image noise levels associated with each method for different levels of source intensity are shown in Figure 5.14. All CT images were computed at 60 keV, which is approximately the mean of the effective energies of low- and high-energy scans. The image noise level is calculated as one standard deviation (1σ) of HU values for pixels within selected regions inside the solid water background.

The DEAM-reconstructed images in the JSIR-BVM method are 4-fold less noisy than the FBP reconstructions in either the image- or sinogram-domain decomposition methods while

93
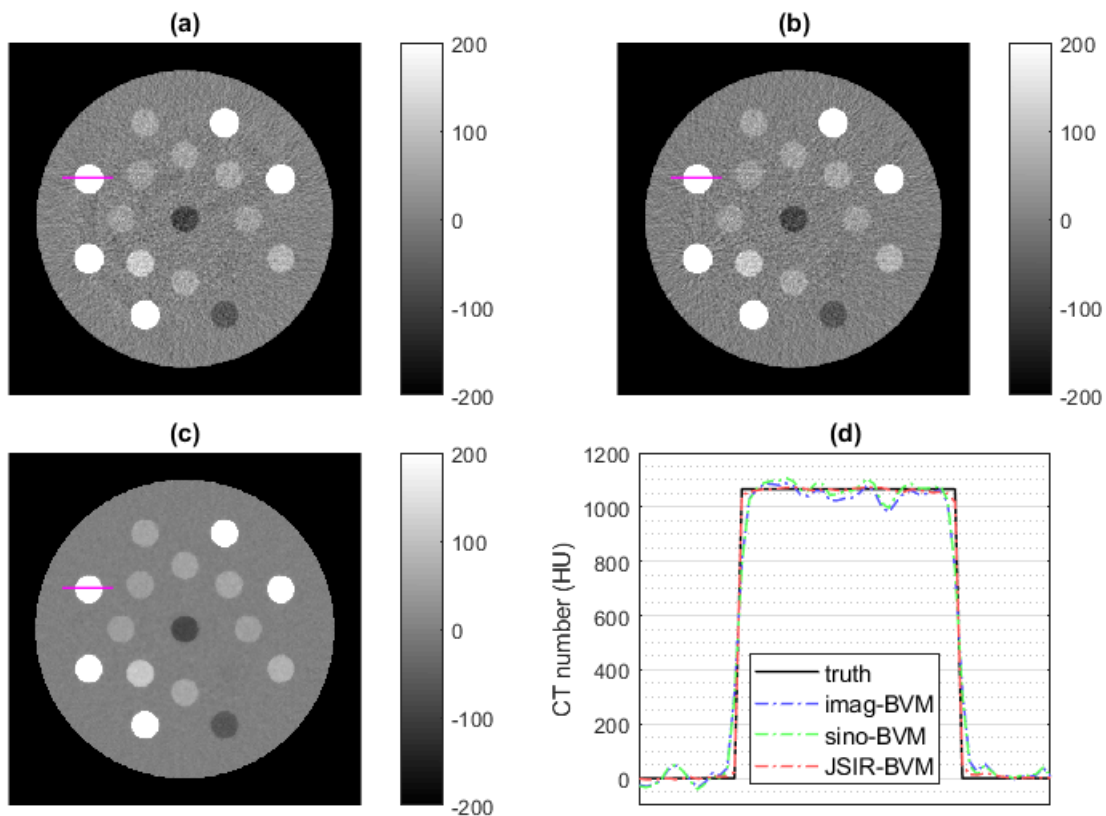
Figure 5.13: Monochromatic CT images (60 keV) of the tissue #1 phantom reconstructed by the BVM-based (a) image-domain, (b) sinogram-domain, and (c) JSIR methods from 100% source-intensity sinograms. (d) shows the profiles across a bone insert (rib, 10th) indicated by the magenta lines in images.
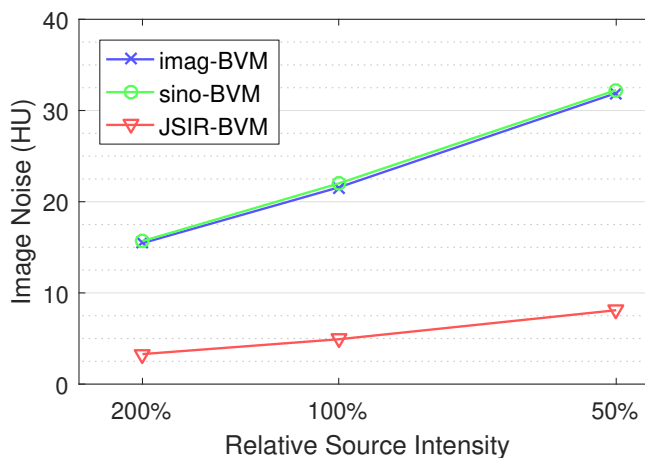
Figure 5.14: Comparison of the image noise level of 60 keV monochromatic CT images from different reconstruction approaches.
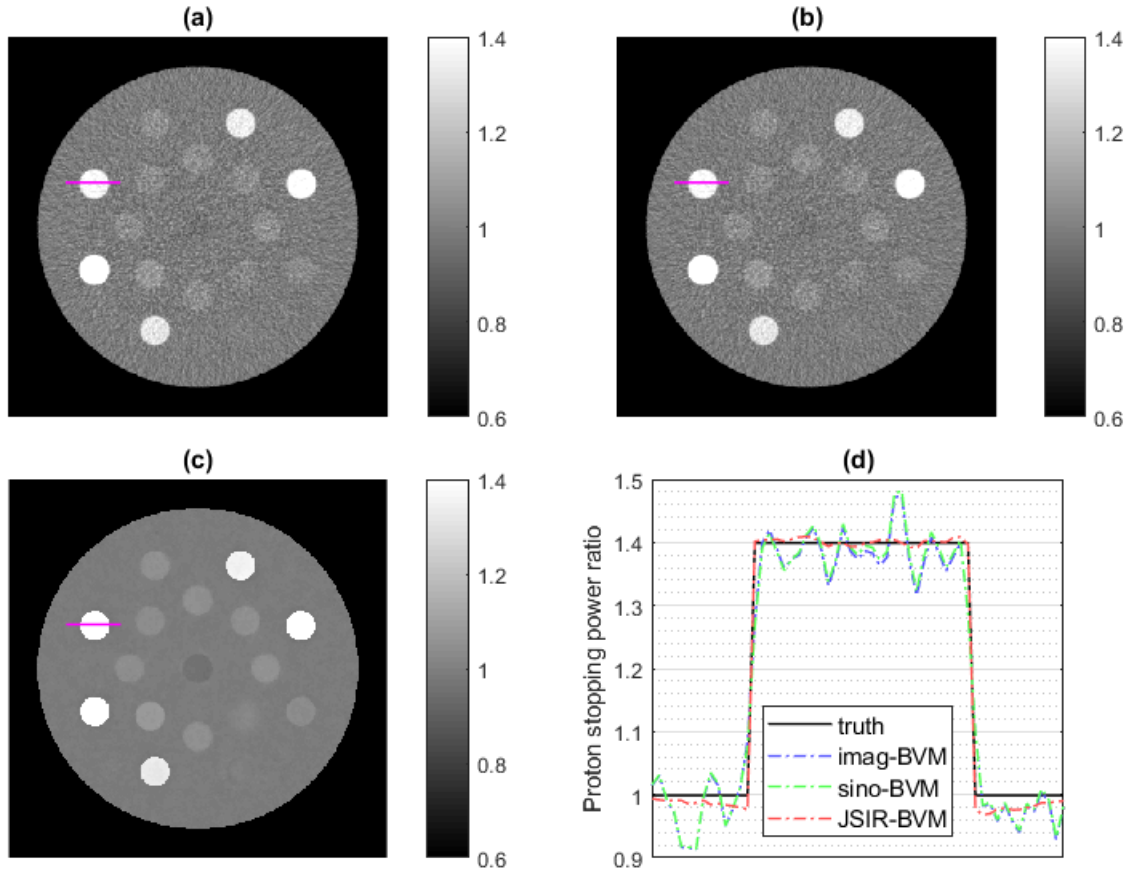
Figure 5.15: SPR images (200 MeV) of the tissue #1 phantom estimated by the BVM-based (a) image-domain, (b) sinogram-domain, and (c) JSIR methods from 100% source-intensity sinograms. (d) shows the profiles across a bone insert (rib, 10th) indicated by the magenta lines in images.

preserving image sharpness at the high-contrast insert boundaries (see Figure 5.13c). Compared to the image-domain decomposition method, both the sinogram-domain decomposition and the JSIR method are able to reduce the streak artifacts between bony inserts in the images. The JSIR method more effectively suppresses such artifacts and achieves more accurate reconstructions. Both CT image noise and residual beam-hardening artifacts are propagated into the converted SPR images as shown in Figure 5.15. The quality of the SPR images derived from the FBP-based image- and sinogram-domain decomposition methods are compromised by the high image noise.
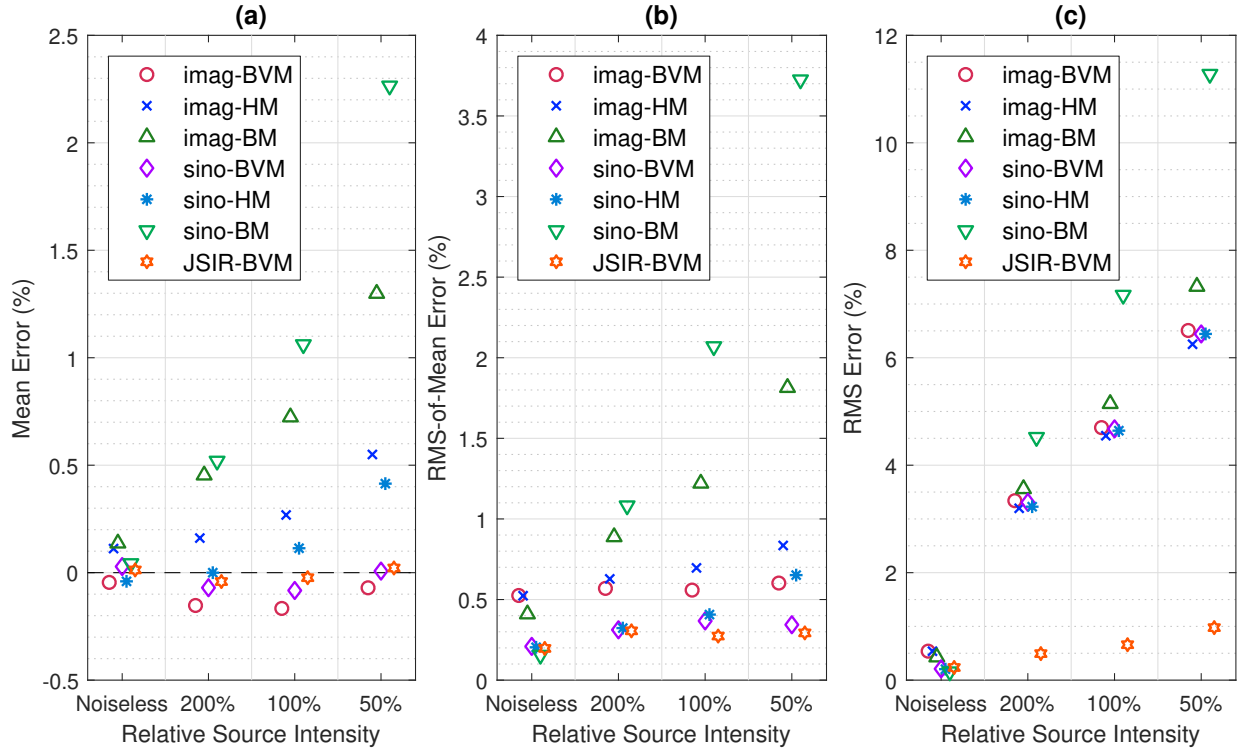
Figure 5.16: Relative SPR estimation errors for reference tissues from each investigated method as a function of sinogram source intensity levels: (a) mean error for all pixels within ROIs, which equals the mean of average estimation errors for different tissues, (b) RMS of average estimation errors for different tissues (RMS-of-mean error), and (c) RMS errors for all pixels within ROIs.

In Figure 5.13, the systematic difference between the results derived from different methods is much smaller than the insert-background contrast and is therefore difficult to visualize on the images. To more quantitatively compare these methods, Figure 5.16 summarizes the statistics for estimation accuracy of all seven investigated methods under different source-intensity levels. Figure 5.17 and Figure 5.18 compare the mean estimation error within each tissue's ROI for all methods applied to the noiseless and 100% source-intensity-level sinograms, respectively.

In the noiseless case, all methods achieve small mean errors, i.e., below 0.15% for all methods. For the sinogram-domain methods and the JSIR method, the RMS-of-mean errors are less
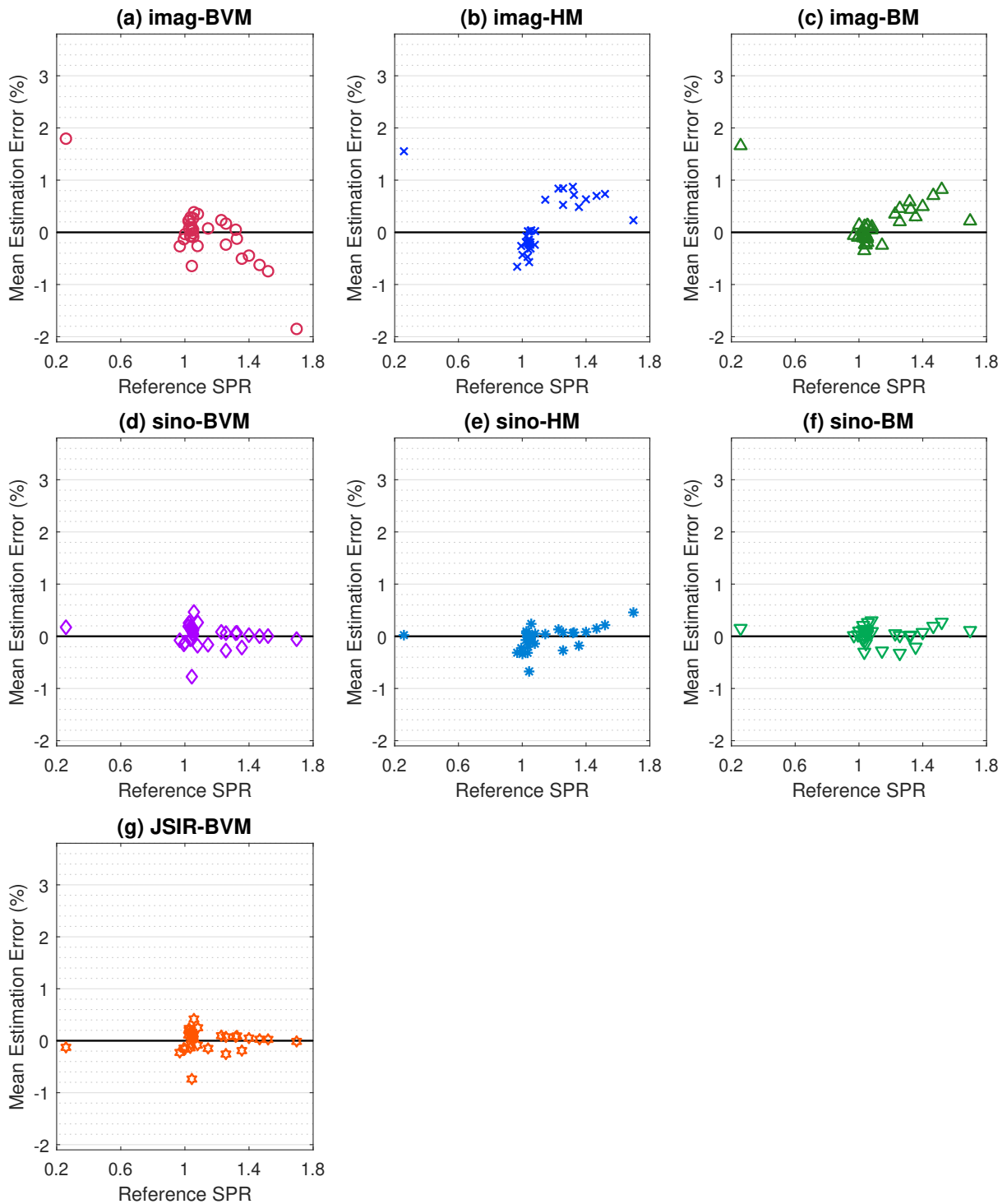
Figure 5.17: Mean of relative SPR estimation errors for each reference tissue sample predicted by each investigated method from noisless sinograms.
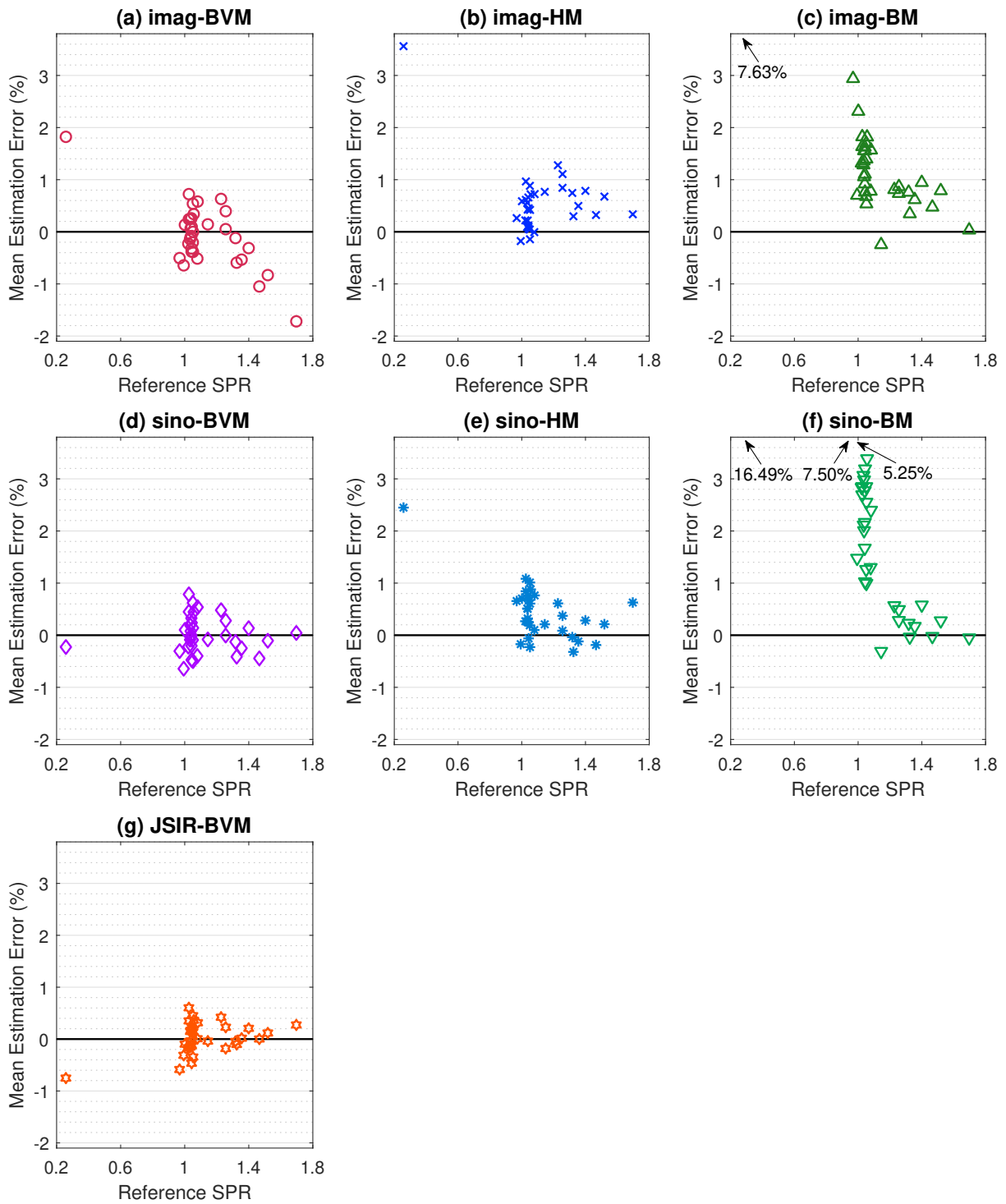
Figure 5.18: Mean of relative SPR estimation errors for each reference tissue sample predicted by each investigated method from 100% source-intensity sinograms. Outliers not included in the display window are indicated by the arrows.

than 0.25% and are comparable to the intrinsic modeling error. The mean SPR estimation error for each individual tissue samples is within 0.5% (except for the thyroid tissue). On the other hand, the RMS-of-mean errors of the image-domain decomposition methods are approximately twice the modeling error. The higher estimation errors of the image-domain decomposition methods in the noiseless case can be explained by the systematic image intensity errors including the HU nonuniformity due to the impact of residual beam-hardening effects. The BVM-based image-domain decomposition method clearly shows the impact of residual beam-hardening effects, i.e., the SPRs of bony tissues with higher Z_{eff} tend to be more underestimated.[4]

The performances of most of the methods deteriorate when noise is present in the sinograms. The RMS-of-mean errors generally increase with the noise level. Among the seven methods, the JSIR-BVM method has the best performance, which achieves mean and RMS-of-mean errors of less than 0.05% and 0.31%, respectively, for all noise levels. These errors are close to the intrinsic BVM modeling accuracy and almost do not change with the noise level. As shown in Figure 5.18, under the 100% source intensity level the JSIR-BVM achieved mean errors of less than 1% for all tissue samples. On the other hand, some of the other methods exhibit relatively large mean errors for individual tissue samples, especially for the low-density deflated lung tissue.

For the same source intensity level, the RMS errors of the JSIR-BVM method are less than 1/6 of those of all the other six methods, which indicates that the JSIR-BVM method has much smaller pixel-to-pixel SPR variations inside homogeneous regions compared to the other two approaches. Thus the JSIR-BVM method achieves high mean estimation accuracy

---

[4]For bony tissues, the reference SPR, which is shown as the x-axis in Figure 5.17 and Figure 5.18, is generally positively correlated with Z_{eff}.

under different noise levels as well as dramatically reduces the statistical uncertainty of SPR estimates.

For all six image- and sinogram-domain decomposition methods, the pixel-wise variations of SPR estimates are approximately twice as large as the corresponding 60 keV monochromatic CT image noise. The BVM and Hünemohr model-based methods exhibit similar noise propagation from the sinogram to the SPR image. The Bourque model-based methods, however, results in slightly larger RMS error than the other methods for the same noise level. Besides introducing random uncertainty into SPR images, sinogram noise also lead to systematic errors for most image- and sinogram-domain decomposition methods. Generally, the RMS-of-mean errors monotonically increase with the sinogram noise level, which indicates the mean SPR estimation error for each individual tissue samples increases when the sinogram noise gets higher. The mean errors exhibited by both Bourque and Hünemohr model-based methods also increase with the increased noise level, while those of BVM-based methods remain relatively low for all noise levels. The sinogram-domain decomposition methods based on BVM and Hünemohr's model generally achieve lower mean and RMS-of-mean errors than the corresponding image-domain decomposition methods. Bourque's model-based sinogram-domain decomposition method, however, is the least robust of all the methods. Among the six image- and sinogram-domain decomposition methods, the sinogram-domain BVM method is the most robust in the presence of noise.

5.4.2   Impact of test object geometry

The impact of object size variations on the estimation accuracy was evaluated by scaling the 330 mm diameter test phantoms to 250 mm diameter (i.e., about 25% smaller than the calibration phantom) with proportionally scaled insert sizes and positions, while calibration

processes were based on 330 mm calibration phantoms. Only noiseless sinograms were used in these comparisons in order to avoid the impact of random uncertainties.

Figure 5.19 shows the differences of the mean SPR estimates on the scaled 250 mm phantom compared to those on the 330 mm test phantoms for all tissue inserts. As indicated by the results, both the JSIR-BVM method and the sinogram-domain decomposition methods, which jointly reconstruct spectrum-invariant component images, are almost unaffected by the size change. The mean SPR differences between the test phantoms of the two different sizes are less than 0.15% for the same tissue (except for the low-density deflated lung tissue in the JSIR-BVM method).

All image-domain decomposition methods, however, are sensitive to phantom size due to the dependence of residual beam hardening effects on scan object size, leading to size-dependent CT numbers in the separately reconstructed images. This effect leads to overestimation of SPRs of $1-4\%$ for bony tissues in the 250 mm phantom compared to the 330 mm phantom. Bony tissues with higher Z_{eff} tend to exhibit a larger difference in SPR estimates due to the sensitivity to beam hardening effects. SPR estimates of low-Z_{eff} tissues, such as the adipose tissue, are reduced up to about 0.3% on the smaller test phantom. This pattern of errors is nearly identical for all three image-domain methods based on different DECT-SPR models. This result suggests that the HU difference caused by the residual beam hardening effects in the single-energy reconstructed images is the dominant contribution to the systematic variation of SPR estimates.

The image-domain BVM method was then chosen to further analyze the impact of object size and location. A series of test phantoms with cortical bone inserts at different positions (i.e.,
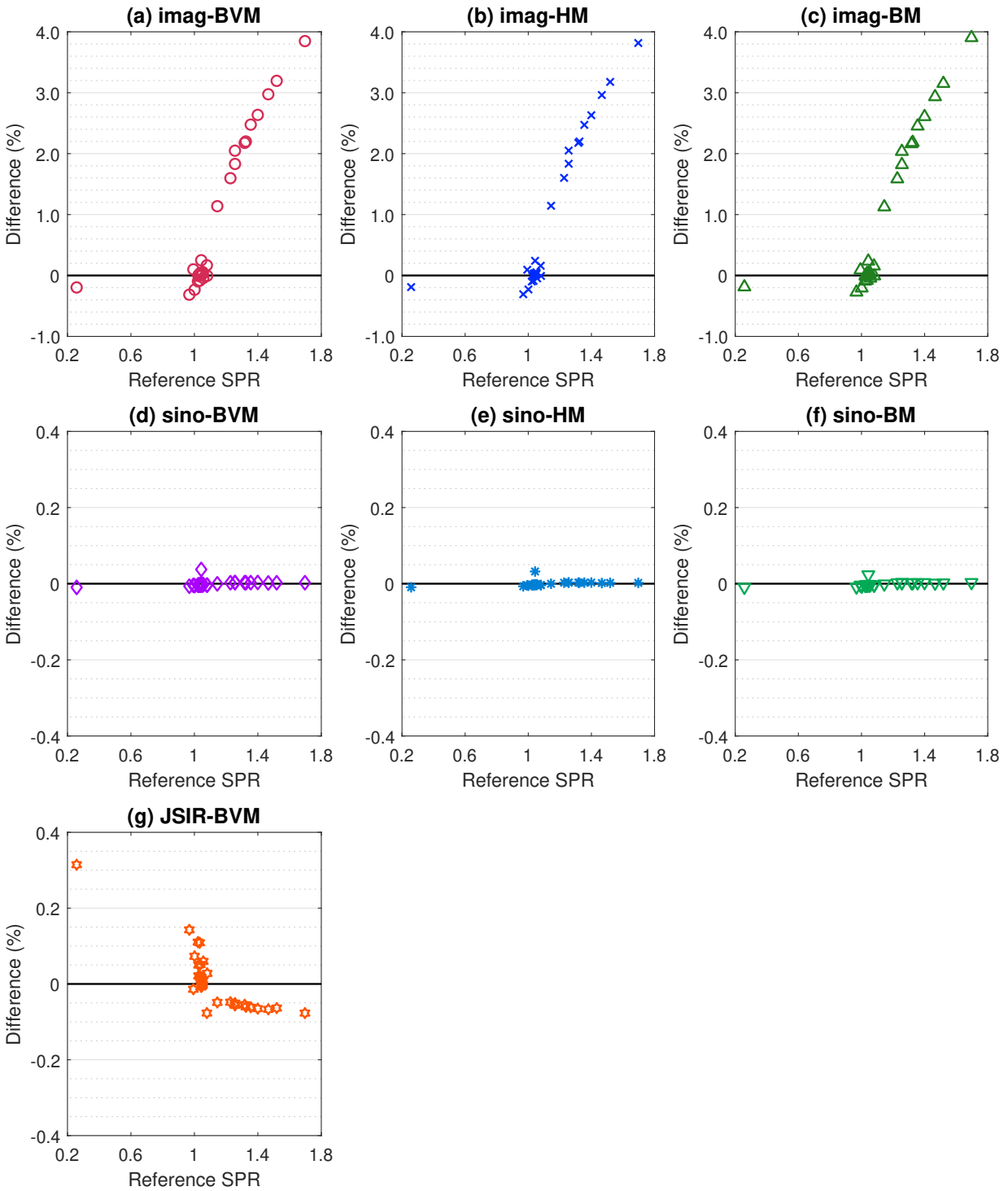
Figure 5.19: Percentage difference of mean SPR estimate for each reference tissue sample due to the test phantom size being changed from 330 mm to 250 mm for each investigated method.
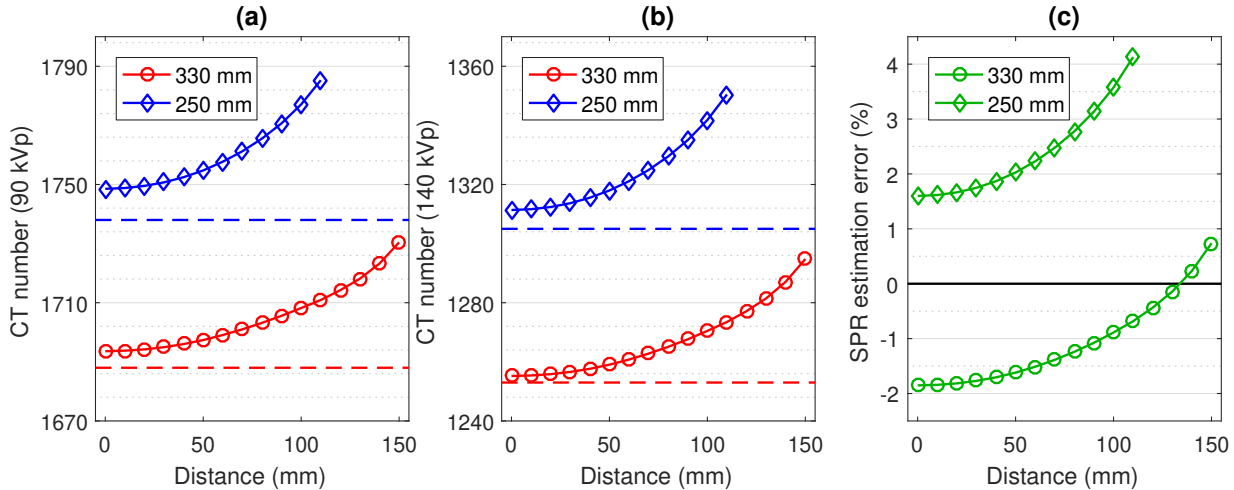
Figure 5.20: The average CT numbers of the cortical bone sample on the (a) 90 kVp and (b) 140 kVp images reconstructed via FBP, and (c) the corresponding relative SPR estimation error from the image-domain BVM method as a function of the distance between the center of the insert and that of the phantom. The dashed lines indicate the expected CT numbers for the bone insert located at the phantom center.

different distances from the phantom center) were generated, where each phantom contains only one cortical bone insert.[5]

As Figure 5.20 shows, both the reconstructed CT image intensities and predicted SPR values of cortical bone tissue depend on both of the phantom size and the radial distance from the phantom center. In the two separately reconstructed images, the CT numbers of the smaller phantom are generally higher than those on the larger phantom. On the same phantom, the CT numbers also increase with the distance from the phantom center.

The trend of the CT number variation can be explained as follows. Conventional beam hardening corrections, including the water-based correction we implemented and many calibration-based correction methods of commercial scanners, assume that the patient is composed of variable-density but fixed atomic composition. However, when patient tissue composition

---

[5]The cortical bone has the highest Z_{eff} among all reference tissues and is therefore the most sensitive to geometry change.

deviates significantly from water, water-based BH correction would result in residual HU dependency on size and location, or more precisely the local equivalent spectrum. The equivalent spectrum for a pixel at the center of a cylindrical phantom is generally harder than that for a pixel at the borders due to the larger filtration from other parts of the scanned object. Thus, the HU values of high-Z materials at the borders tend to be higher than those of the same material at the center. Similarly, for objects of different sizes, the larger objects generally have more filtration and therefore have lower CT numbers.

On the same phantom, the difference of CT numbers between the central and the peripheral inserts can be as much as $40 \, \text{HU}$ (i.e., around 1.5%) in both low- and high-energy CT images, which leads to more than a 2% increase in the predicted SPR. The difference between the SPR estimates of the central insert on the large phantom and that of the peripheral inserts on the small phantom can be as much as 6%. Similar results are also obtained for the other two image-domain decomposition methods. On the other hand, the position-dependent HU variations in the sinogram-domain decomposition and the JSIR methods are less than $5 \, \text{HU}$. Thus the two approaches are able to achieve uniform SPR estimates with less than 0.1% variation across the whole phantom.

Moreover, besides the test object variability, the location-dependent CT number variations of the calibration phantoms can also introduce noticeable uncertainties into the SPR estimates of the test objects for the calibration-based image-domain methods. Figure 5.21 shows that a rearrangement of the Gammex inserts in the calibration phantom, in which the inner ring and outer ring of inserts were exchanged, alters soft and bony tissue SPR estimates by as much as 0.36% and 0.77%, respectively, for the image-domain Bourque method.
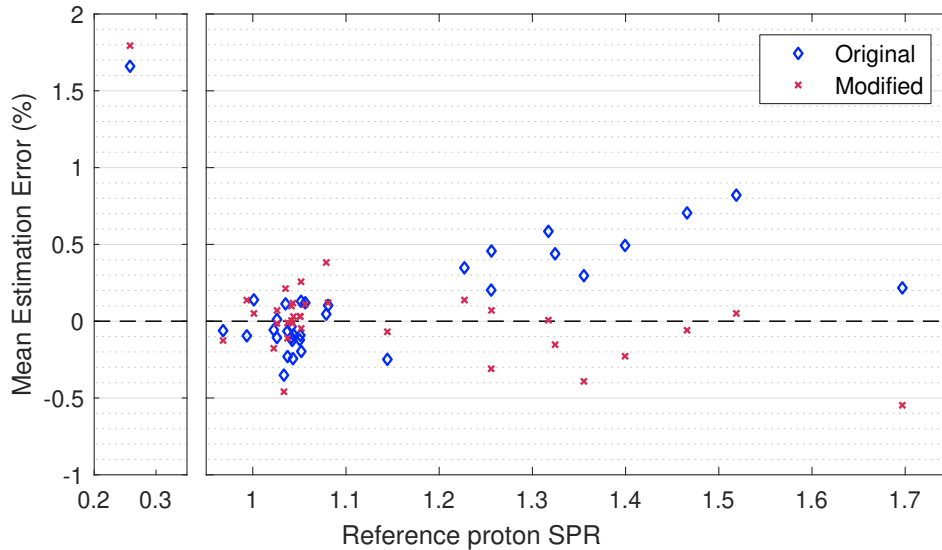
Figure 5.21: Comparison of average SPR estimation error for each tissue sample of the image-domain Bourque method calibrated by the Gammex phantom with two different insert arrangements.

5.5 Simulation of a virtual patient

The seven methods in Table 5.4 were then evaluated using the ICRP adult female phantom [95].[6] Three slices in the head, thorax, and pelvis regions were selected for simulation and twelve ROIs were selected within homogeneous areas (as shown in Figure 5.22). The ROIs contain ten soft tissue regions, including one lung tissue region with relatively low density, and two spongiosa regions. Table 5.5 shows the reference radiological properties of the tissues in selected ROIs.

Synthetic sinograms were generated for the 100% source intensity level, which was set to 300 mAs for 90 kVp and 90 mAs for 140 kVp, and then processed by the seven investigated methods. Other specifications of data generation and image reconstruction are the same as

---

[6]The anatomical model of the ICRP adult female phantom is based on a 43-year-old individual with height of 167 cm and weight of 59 kg. The tissue composition of the adult female phantom was given by ICRP and is not exactly the same as the reference human tissues listed in Appendix A. The detailed properties for all tissue types can be found in [95].
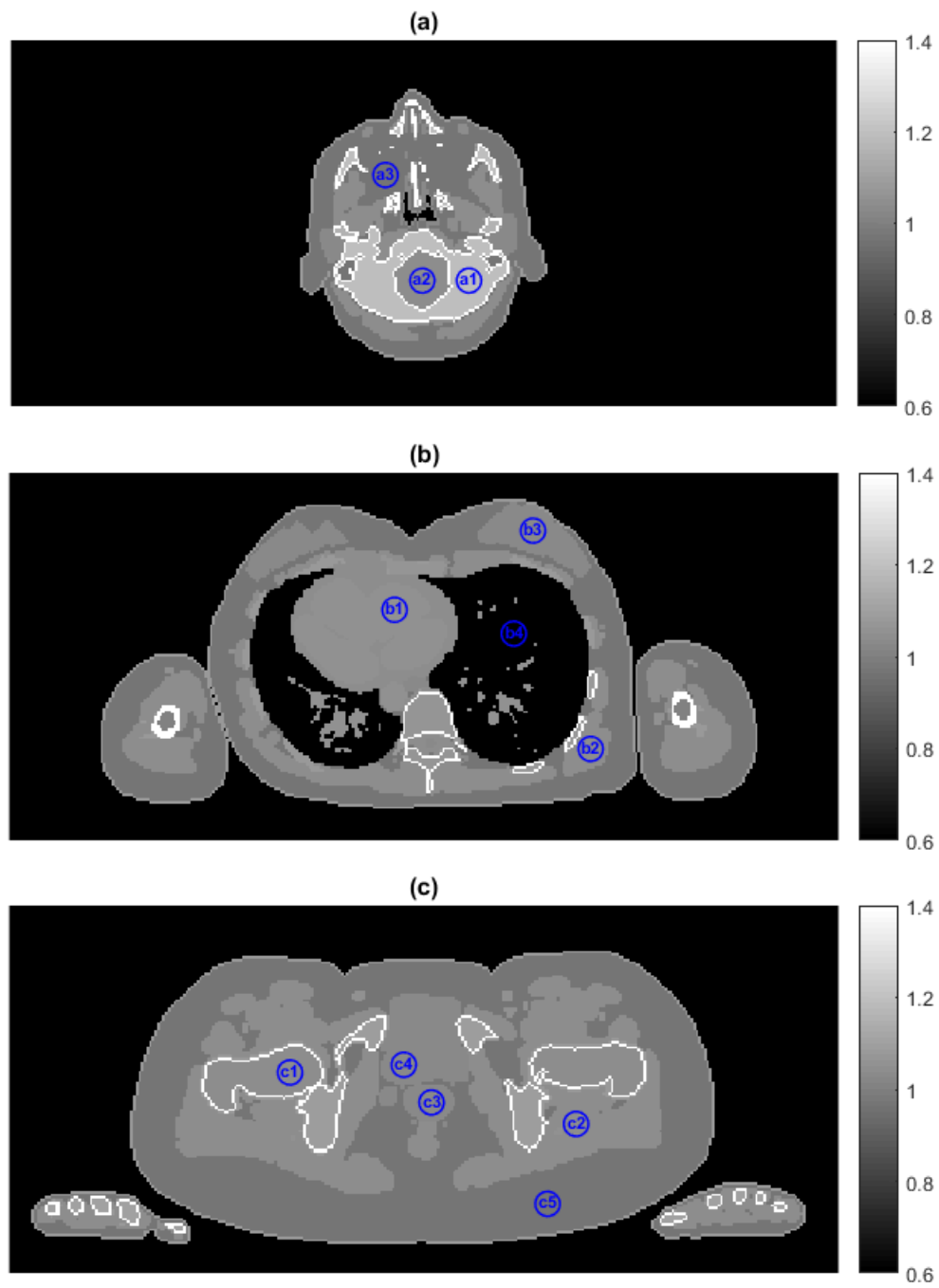
Figure 5.22: True SPR images (200 MeV) of the virtual patient with selected ROIs: (a) head, (b) thorax, and (c) pelvis.

Table 5.5: Properties of ICRP tissue types within selected ROIs.

Tissue Type	Index of ROI			$\rho_e/\rho_{e,\mathrm{w}}$	I (eV)	$S_p/S_{p,\mathrm{w}}$
	head	thorax	pelvis			
Cranium, spongiosa	a1			1.209	81.4	1.198
Femora, upper half, spongiosa			c1	1.038	69.3	1.048
Blood		b1		1.050	75.2	1.050
Muscle tissue		b2	c2	1.040	74.6	1.041
Brain	a2			1.045	73.9	1.047
Large intestine			c3	1.033	74.5	1.035
Uterus			c4	1.023	71.5	1.030
Breast (mammary gland)		b3		1.021	66.9	1.036
Adipose tissue	a3		c5	0.951	64.9	0.968
Lung tissue (compressed lungs)		b4		0.382	75.1	0.382

those in Section 5.4, except that the reconstruction parameter λ of the JSIR method was set to 6 for the thorax and pelvis slices and 20 for the head slice due to the volume difference.

Figure 5.23 shows the reconstructed SPR images for the three BVM-based methods. As the results show, the images reconstructed by the image- and sinogram-domain methods are of comparable quality and contain streak artifacts along the directions in which the path length through the patient body is relatively long. On the other hand, the JSIR-BVM method dramatically suppresses noise and artifacts as well as presents better spatial resolution than the other two methods, especially for the bone-soft tissue boundaries.

Figure 5.24 and Figure 5.25 compare the mean and standard deviation of the estimation errors, respectively, within each ROI. The JSIR-BVM method outperforms the other methods, which achieves RMS-of-mean errors of 0.15%, 0.90%, and 0.20% for electron density, mean excitation energy, and proton SPR, respectively. The maximum absolute-mean errors for each of the ROIs are 0.27%, 1.92%, and 0.37% for electron density, mean excitation energy, and proton SPR, respectively. The JSIR-BVM method also achieves much smaller variation within homogeneous regions, while the other six methods present comparable pixel-to-pixel variations.
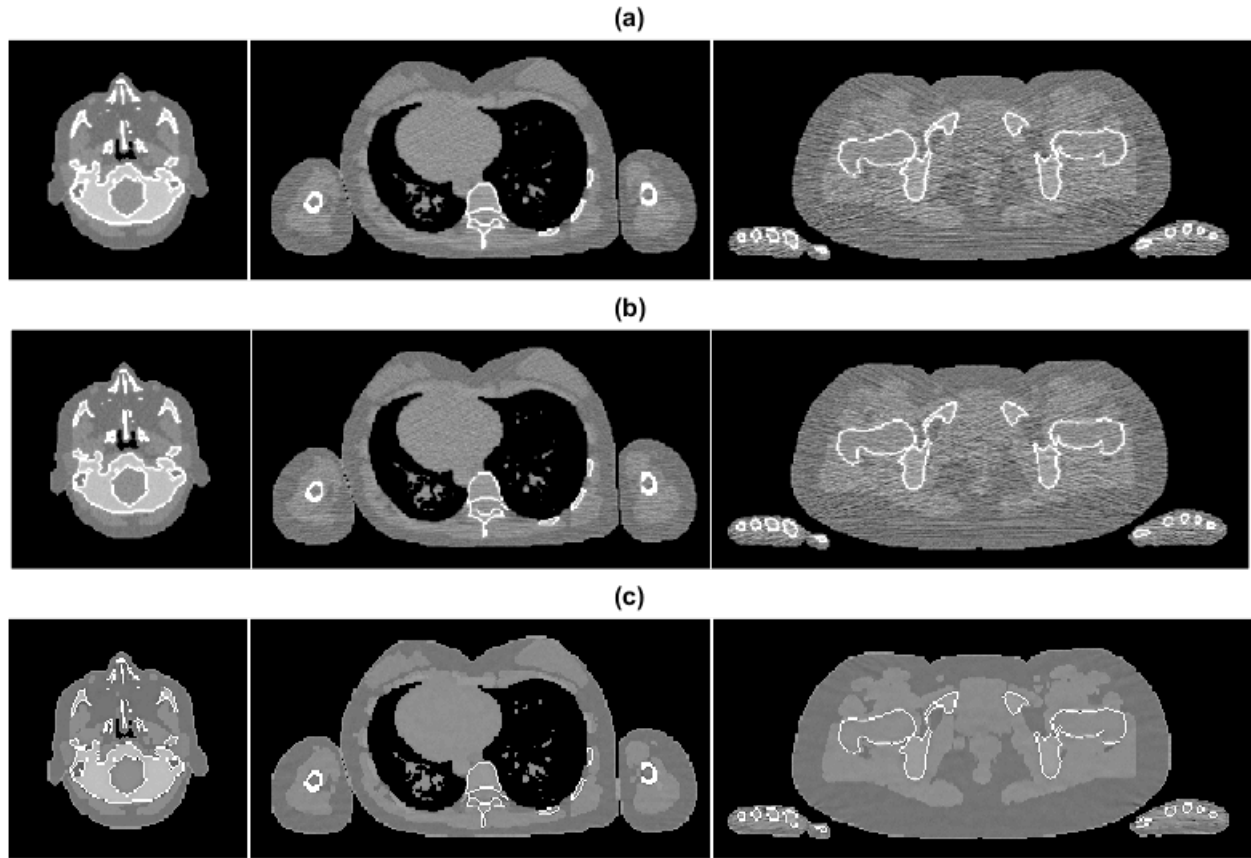
Figure 5.23: The SPR images of the three slices estimated by the BVM based (a) image-domain, (b) sinogram-domain, and (c) JSIR methods. The display window is the same as that in Figure 5.22.

Among the other six methods, the BVM- and Hünemohr model-based sinogram-domain methods achieve better performance than the others, whose RMS-of-mean errors are 0.27% and 0.50%, respectively, for proton SPR estimates. The performances of both Bourque model-based methods get worse when the patient volume increases (i.e., in the pelvis slice).

All three image-domain methods overestimate the SPR of spongiosa tissue in the head slice (i.e., ROI "a1") by 2% to 3%, which is due to the size-difference between the calibration phantom (330 mm in diameter) and the scanned patient site. The impact of size-dependence in the image-domain methods is not very clearly shown for other ROIs because all selected
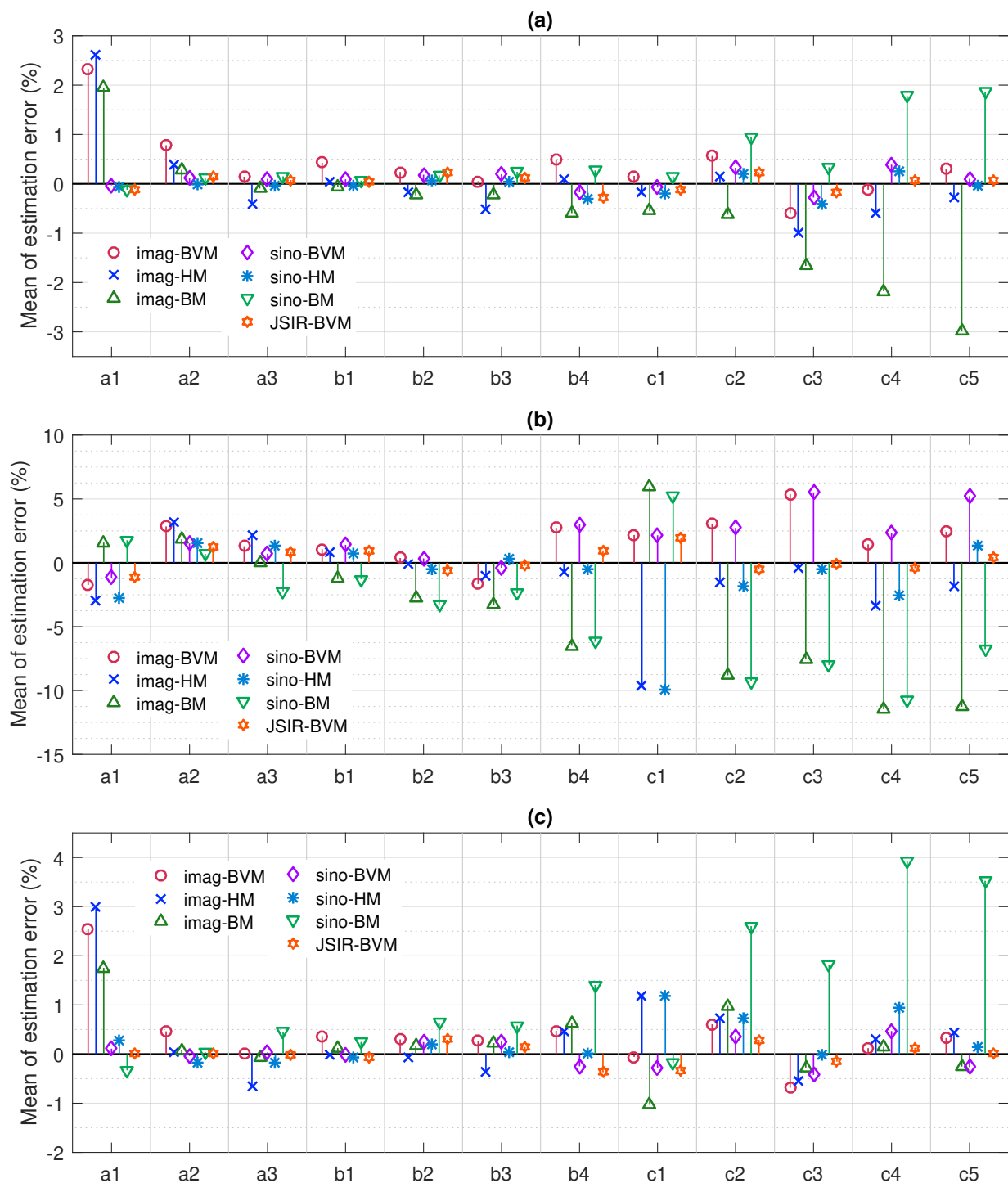
Figure 5.24: Mean estimation error of (a) electron density, (b) mean excitation energy, and (c) proton SPR for selected ROIs.
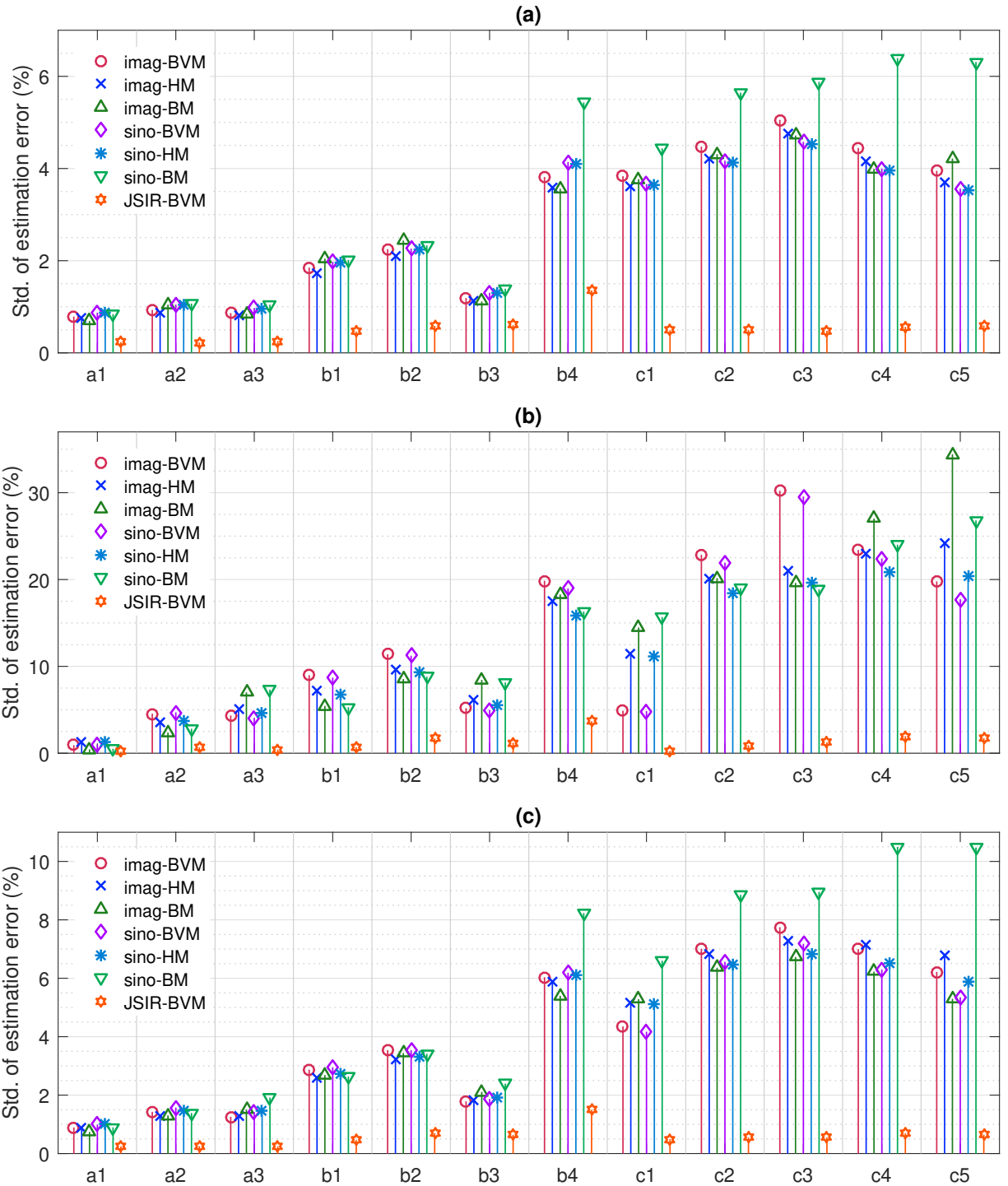
Figure 5.25: Standard deviation (1σ) of estimation errors of (a) electron density, (b) mean excitation energy, and (c) proton SPR for selected ROIs.

ROIs are soft tissues or spongiosa tissues with relative low Z_{eff}, which are not as sensitive to geometry difference as dense bones.

Figure 5.26−5.28 show the distribution of WEPL errors of each patient slice. The WEPLs were computed via Radon transform of the reconstructed SPR images for 100 parallel beams with width of 1 mm for every degree. Table 5.6 summarizes the RMS of WEPL estimation errors for each method and Table 5.7 shows the percentage of predicted WEPLs whose absolute errors exceed 1% of the reference value.

The JSIR-BVM method has the smallest bias and variance of the resultant distribution of WEPL errors among these methods. Most of the estimated WEPLs are close to 0% for all three slices, while only less than 1.5% of the estimates have more than 1% error.

For the head slice, the estimates of all image-domain method are approximately systematically biased by 0.9% to 1.3%, while those of the BVM- and Hünemohr model-based sinogram-domain methods are slightly biased by −0.4% to −0.6%. The systematic bias is much smaller for the thorax and pelvis slices, which is because the size difference between the patient and the calibration phantom is smaller for these two slices.

The sinogram-domain Bourque method becomes the worst for the large patient volume (i.e., the pelvis slice), which may be due to the sensitivity of this method to image noise, which was shown in Section 5.4.

5.6   Discussion

The performance of DECT-based SPR estimation methods is affected by two main sources of uncertainties. The first class is the SPR modeling error, which refers to the estimation
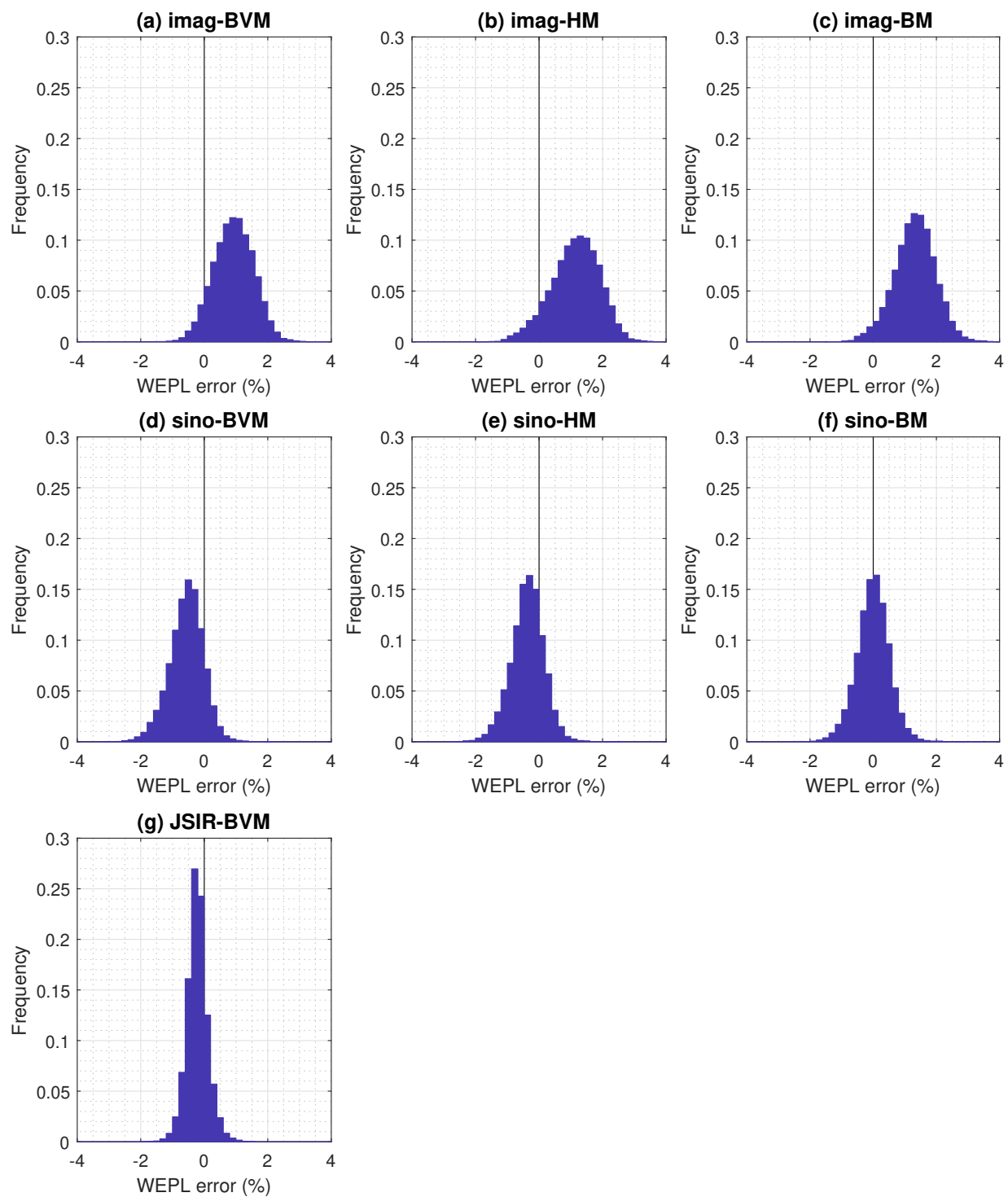
Figure 5.26: The distribution of errors of WEPLs predicted by each investigated method for the head slice.
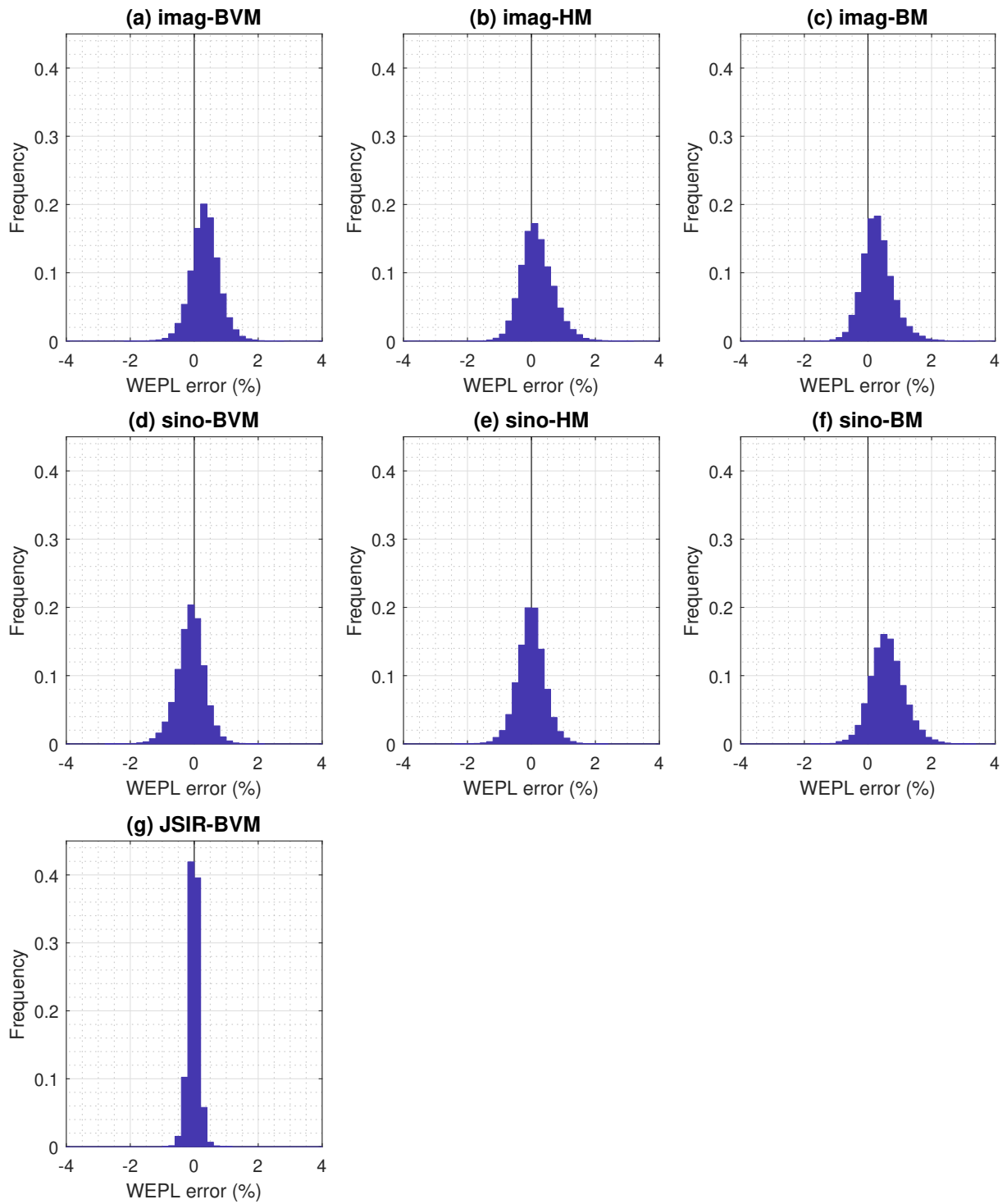
Figure 5.27: The distribution of errors of WEPLs predicted by each investigated method for the thorax slice.
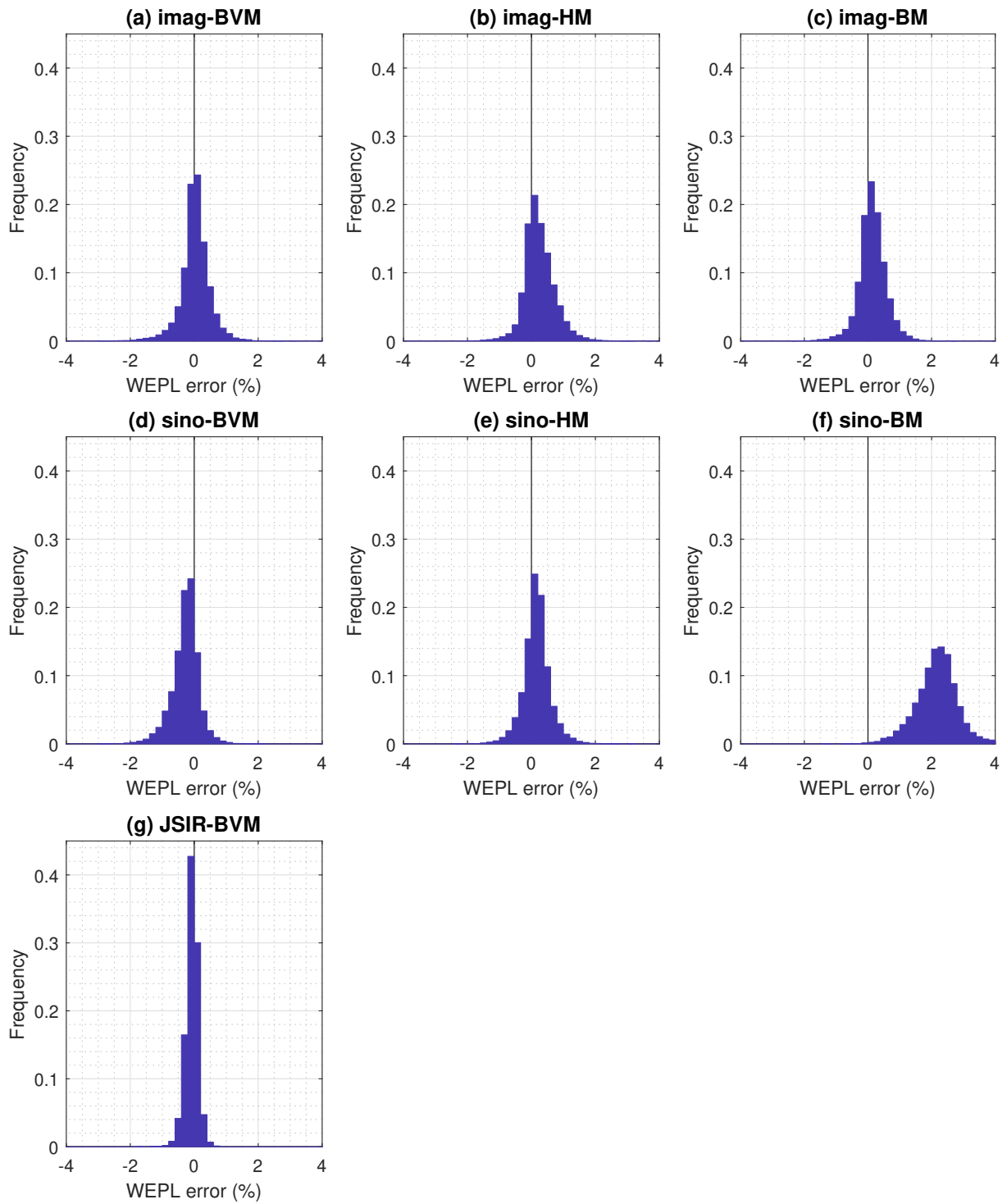
Figure 5.28: The distribution of errors of WEPLs predicted by each investigated method for the pelvis slice.

Table 5.6: The RMS of WEPL estimation errors for each investigated method.

	head	thorax	pelvis
imag-BVM	1.12%	0.55%	0.45%
imag-HM	1.37%	0.54%	0.53%
imag-BM	1.47%	0.57%	0.45%
sino-BVM	0.78%	0.45%	0.51%
sino-HM	0.64%	0.43%	0.45%
sino-BM	0.52%	0.81%	2.27%
JSIR-BVM	0.40%	0.16%	0.21%

Table 5.7: Fraction of absolute WEPL estimation errors exceeding 1% of the reference value.

	head	thorax	pelvis
imag-BVM	45.90%	6.62%	4.52%
imag-HM	59.83%	6.85%	6.87%
imag-BM	69.92%	8.26%	3.90%
sino-BVM	19.82%	3.63%	5.80%
sino-HM	11.68%	2.95%	3.97%
sino-BM	5.90%	21.80%	95.45%
JSIR-BVM	1.49%	0.01%	0.10%

errors of radiological quantities (i.e., electron density, mean excitation energy, and SPR) derived from the idealized DECT measurements. The second class is the image formation uncertainty introduced during CT sinogram acquisition and image reconstruction processes.

Both previous studies [13, 52] and our analysis show that multiple available DECT-SPR models are able to support relatively low intrinsic SPR modeling errors for the reference human tissues. However, we also demonstrate that such high accuracy is not achievable in clinical settings due to the aforementioned image formation uncertainties, including image noise propagated from the measurement and systematic errors due to incomplete correction for scattering and beam hardening. It should be noted that the impact of random noise on method performance is model specific. In our analysis, the Bourque model shows more sensitivity to the noise level than the BVM and the Hünemohr model. This is possibly

due to the high degree of nonlinearity of the Bourque model, which involves three 5th-order polynomial fittings using only 13 distinct tissue substitutes in the calibration process.

As the results demonstrate, the widely-accepted image-domain decomposition approach is vulnerable to image formation uncertainties. Though it is assumed that the scanning conditions of the calibration phantoms can be identically reproduced for the test phantoms and patients, the anatomy, size, ROI location, and composition of patients may differ from those of the calibration phantoms. Our study shows that even simple dissimilarities between the calibration phantom and test object, such as size scaling or ROI position changes, yield CT number variations that cannot be fully accounted for by the calibration process, and thus introduce systematic errors into SPR estimates. Since these image-domain decomposition methods rely on two separately reconstructed CT images, residual beam hardening effects introduce image intensity uncertainties as well as other image artifacts, leading to systematic SPR estimation error much larger than the intrinsic modeling error, thereby limiting the benefit of DECT in mitigating proton range uncertainty. Similar issues caused by uncorrected systematic variations have also been discussed in previous studies [26, 96]. On the other hand, the sinogram-domain methods and the JSIR-BVM method are able to circumvent the influence of unaccounted beam hardening effects with prior knowledge of the spectra.

Although sinogram-domain decomposition methods suffer less from the systematic uncertainties introduced by geometry changes, they may also show degraded estimation performance in the presence of random noise in the measurement data. Likewise, image-domain decomposition methods are also vulnerable to noise in the images. Due to the DECT decomposition process being ill-conditioned, the random sinogram noise is amplified in both image- and sinogram-domain decomposition methods. Moreover, Bär *et al.* [13] have suggested that the impact of random noise cannot be canceled via averaging and may introduce systematic errors into the proton range computation. Our current study confirms that mean errors and

116

RMS-of-mean errors of most image- or sinogram-domain decomposition methods increase with elevated sinogram noise. The WEPLs predicted by image- or sinogram-domain decomposition methods have a much wider distribution around the truth than the JSIR-BVM methods and may be systematically biased.

Our JSIR-BVM method accounts for both systematic bias correction and random noise suppression, and thus shows a robust response to the inherent uncertainties of the acquired sinogram data. Unlike step-wise methods that perform the two-parameter estimation on reconstructed HU images, the JSIR-BVM method directly solves the intertwined problem of the material characterization and image reconstruction. The underlying statistical reconstruction algorithm along with a well-established CT data model dramatically reduces both systematic uncertainties and random noise [42, 94, 97]. The results demonstrate that the JSIR-BVM method supports accurate SPR mapping and WEPL prediction for various object geometries and outperforms other investigated methods in terms of robustness to random uncertainties.

The performance of the JSIR-BVM method relies on an accurate CT forward model, i.e., the ability to compute the expected mean of CT measurements given a known scan object. One important component of forward-modeling uncertainties is that of the x-ray spectra. In these simulation analyses, the spectrum-related errors are ignored and thus have no impact on the reported results. In other words, the spectra are assumed to be known exactly by both the sinogram-based and joint reconstruction techniques. Meanwhile, a perfect beam-hardening correction function, which fully corrects the nonlinearity of water attenuation under the spectra used for sinogram generation, is assumed for image-based techniques.[7] This simulation study also neglects the effect of scattered radiation for all methods. Additionally,

---

[7]It should be noted that the image-domain methods also require some sort of prior knowledge about the spectrum, which is implicitly embedded in the beam-hardening correction.

in our simulation of these calibration-based methods, the physical density and elemental compositions of calibration materials were assumed to be known exactly. In the clinical setting, uncertainties of the actual composition and density of calibration materials may also impact the performance of calibration-based methods. The more realistic performance achievable in practices will be addressed in the experimental study.

Chapter 6

Experimental implementation of the JSIR-BVM method

In this chapter, we experimentally assess the performance of the JSIR-BVM method using the raw DECT data acquired on a commercial CT scanner. The image-domain Hünemohr-Saito (HS) method was applied to the scanner-reconstructed CT images for comparison.

6.1 Experiment setup

Two customized test phantoms of different sizes (shown in Figure 6.1) were used in our experiments to assess the performance of the proposed JSIR approach. The head-sized phantom has a cylindrical acrylic shell with a diameter of $215\,\mathrm{mm}$ and is filled with water. A separate acrylic body-ring, which is elliptically shaped with a major axis of $350\,\mathrm{mm}$ and a minor axis of $260\,\mathrm{mm}$, was placed around the cylindrical phantom in order to imitate typical pelvic volume. The first phantom setup is referred to as the *head phantom* and the second one is referred to as the *body phantom.*
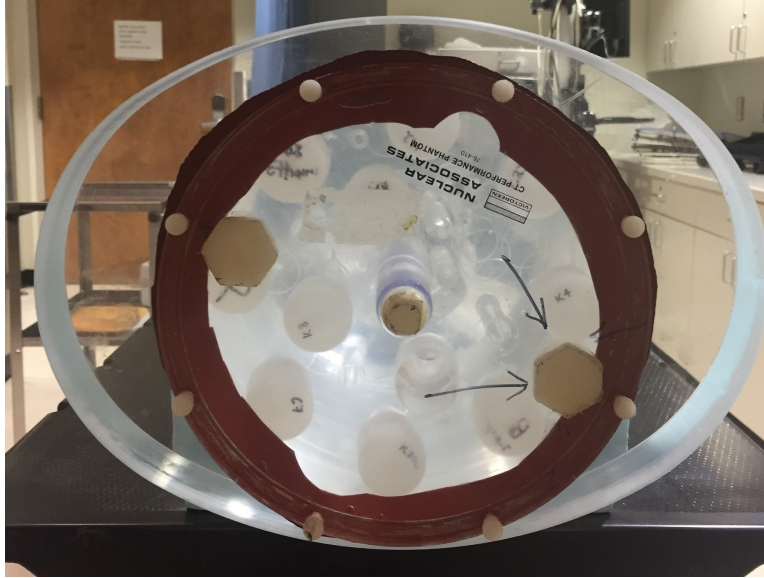
Figure 6.1: Image of the test phantom used in the experiment (front view). The phantom consists of a water-filled cylinder with a removable elliptical body-ring. The photo was taken by Dong Han at Virginia Commonwealth University.

Table 6.1: Properties of investigated phantom materials.

	Material	Composition[†]		ρ (g/mL)	$\rho_e/\rho_{e,\mathrm{w}}$[§]	Z_{eff}	I (eV)	$S_p/S_{p,\mathrm{w}}$[§]
	Water	H_2O		0.998	1.000	7.46	75.3	1.000
	Acetone	C_3H_6O		0.788	0.784	6.34	66.1	0.796
soft	Ethanol	C_2H_5OH		0.789	0.804	6.41	63.1	0.820
	n-Propanol	C_3H_7OH		0.803	0.821	6.22	61.5	0.841
	n-Butanol	C_4H_9OH		0.807	0.826	6.09	60.5	0.848
	CaCl-1	$CaCl_2$	7.20%	1.052	1.045	9.34	80.0	1.037
	CaCl-2	$CaCl_2$	18.24%	1.153	1.130	11.22	87.8	1.110
	CaCl-3	$CaCl_2$	23.07%	1.202	1.171	11.88	91.6	1.144
bony	KP-1	K_2HPO_4	9.37%	1.075	1.066	9.02	80.2	1.058
	KP-2	K_2HPO_4	17.17%	1.149	1.130	9.98	84.5	1.114
	KP-3	K_2HPO_4	29.26%	1.273	1.235	11.19	91.9	1.206
	KP-4	K_2HPO_4	45.21%	1.467	1.397	12.48	103.0	1.346

[†] The concentrations of aqueous solutions are represented by the mass fractions of the salt.

[§] Pure water at 20 °C is used as reference.

Table 6.2: Scan specifications used in the experiment.

Tube potential	90 kVp	140 kVp
Exposure	600 mAs	200 mAs
CTDI$_{vol}$	28.5 mGy	31.6 mGy
Collimation	0.75 mm × 4	

Twelve liquid samples with known compositions were used as the phantom materials in the experiment (see Table 6.1).[1] These samples were contained in plastic bottles with a diameter of 31 mm and then mounted to an out-of-field plate inside the phantom.[2] The phantom materials are divided into two groups: water and organic compounds are considered as soft tissue surrogates, while $CaCl_2$ and K_2HPO_4 aqueous solutions are considered as bony tissue surrogates.

The test phantoms and the Gammex RMI 467 calibration phantom (Gammex, Middleton, WI) were scanned on a Philips Brilliance Big Bore CT scanner (Philips Medical Systems, Cleveland, OH) using an axial pelvis protocol at two different tube potentials (shown in Table 6.2). The narrowest collimation setting that is available on the scanner was used in order to minimize the contamination of scattered radiation.

To implement the image-based HS method, the images were reconstructed by the scanner's standard reconstruction process with a pixel size of 0.9776 mm × 0.9776 mm and a slice thickness of 3 mm.

To implement the JSIR reconstruction, the raw sinograms were exported from the scanner and were pre-processed by the tool provided by the vendor without the beam hardening and bow-tie filter corrections. An air-scan was done under the same scan conditions for each

---

[1]The compositions of aqueous solutions were determined by measuring the mass of the solutes and the volume of the water solvent. The densities were determined by measuring the mass of 50 mL of the samples. The measurement uncertainties of the densities and compositions introduce 0.1% uncertainty into the computed ground-truth SPRs.

[2]A fluorinated ethylene propylene (FEP) bottle was used for the acetone sample. High-density polyethylene (HDPE) bottles were used for all other samples.

tube potential to provide the reference unattenuated in-air profile. The determination of the scanner-specific parameters required in the JSIR reconstruction is discussed in Section 6.2. The pixel size and slice thickness of the reconstructed images were set to be the same as the scanner's reconstruction. The regularization parameters in the DEAM algorithm were set to $\delta = 0.01$, and $\lambda = 15$ and 4 for head and body phantoms, respectively, as a trade-off between noise and resolution that ensures the spatial resolution is slightly higher than the scanner's reconstruction for typical soft tissue contrast (75 HU) [94].

The estimates of the electron density, mean excitation energy, and proton SPR of each test sample were compared to the reference ground-truth values listed in Table 6.1, which are computed from the known compositions and densities. The estimation errors were evaluated for a region of interest (ROI) of 24 mm diameter within each homogeneous test sample. The mean and standard deviation of the estimation errors were computed for each test sample. Additionally, water equivalent path length (WEPL) was computed from the reconstructed SPR images for parallel beams from all directions. The differences between the WEPLs predicted from the two methods were compared.

6.2   Forward modeling of the experimental data

Implementing the proposed JSIR-BVM method on a conventional CT scanner requires the following scanner-specific parameters in the CT forward model (3.13):

- The system matrix of the CT scanner, $h(y|x)$, which was computed as the effective length of the intersection between the beam path y and image pixel x for the known scanner geometry.

- The reference unattenuated in-air profiles, $I_{0,j}(y, E)$, which were experimentally determined via an air-scan done under the same scan conditions of the test object.

- The detector-dependent energy-fluence spectra, $\Psi_j(y, E)$, which were experimentally determined via the equivalent spectrum method as described in the following paragraphs.

- An estimate of the background events presented in the measured data, $\gamma_j(y)$, which were assumed to be zero for the narrow collimation used in our experiment.

Determination of the equivalent energy-fluence spectra

The knowledge of the energy-fluence spectrum, which is the down-stream source spectrum weighted by the detector response function, is required for our JSIR-BVM method. A direct measurement of the source spectrum can be done via spectroscopy using energy-resolving detectors [98–100]. However, direct measurement is not trivial and requires a strict measurement procedure. An alternative way, which is used in our experimental implementation, is to estimate the equivalent spectrum via measuring the narrow-beam transmission of metal filters [74, 101, 102].

As stated in Section 1.2.1, the energy-fluence spectrum is mathematically modeled as

$$\Psi(y, E) = \frac{\Phi_0(E)D(E)\exp\left(-l_F(y)\mu_F(E)\right)}{\int_{E'} \Phi_0(E')D(E')\exp\left(-l_F(y)\mu_F(E')\right)\mathrm{d}E'}, \tag{6.1}$$

where $\Phi_0(E)$ is the incident x-ray spectrum of the source tube, $D(E)$ is the response function of the detector, $l_F(y)$ is the width of the bow-tie filter for beam path y, and $\mu_F(E)$ is the attenuation coefficient of the bow-tie filter material.

The incident x-ray spectrum is mathematically modeled via the semi-empirical Birch-Marshall model [86], which parameterizes the spectrum by the peak energy E_{max} and equivalent aluminum filtration l_{eq} as

$$\Phi_0(E) = \Phi_{\mathrm{BM}}\left(E \,|\, E_{\mathrm{max}}, l_{\mathrm{eq}}\right) = \Phi_{\mathrm{BM}}\left(E \,|\, E_{\mathrm{max}}, 0\right) \exp\left(-\, l_{\mathrm{eq}}\, \mu_{\mathrm{Al}}(E)\right), \tag{6.2}$$

where $\mu_{\mathrm{Al}}(E)$ is the photon linear attenuation coefficient of pure aluminum.[3] Ay *et al.* [103] have shown that the Birch-Marshall model was able to predict the $140\,\mathrm{kVp}$ spectrum for a tungsten target to within 1.1% of the direct measurements.

The detector-response function of the energy-integrating detector is modeled as

$$D(E) = E\left(1 - \exp\left(-\, l_{\mathrm{D}}\, \mu_{\mathrm{D}}(E)\right)\right), \tag{6.3}$$

where $\mu_{\mathrm{D}}(E)$ and l_{D} are the linear attenuation coefficients and thickness of the scintillator in the detector module, respectively.

For each of the two tube potentials used in the experiment, transmission profiles of narrow beams penetrating through stacks of high-purity aluminum (Al) and copper (Cu) filters with varying thickness were measured on the central axis of the scanner. A collimator assembly (shown in Figure 6.2) was used to ensure that the measurements were free from the contamination of scattered radiation. Twenty-one different combinations of Al and Cu filters were measured for each tube potential. The equivalent Birch-Marshall spectra were determined by minimizing the relative square-error between the modeled and measured

---

[3]The original Birch-Marshall model has three parameters: peak energy, equivalent aluminum filtration, and the anode angle for the source tube. The anode angle is a fixed parameter for a given tube, which is known for our scanner.
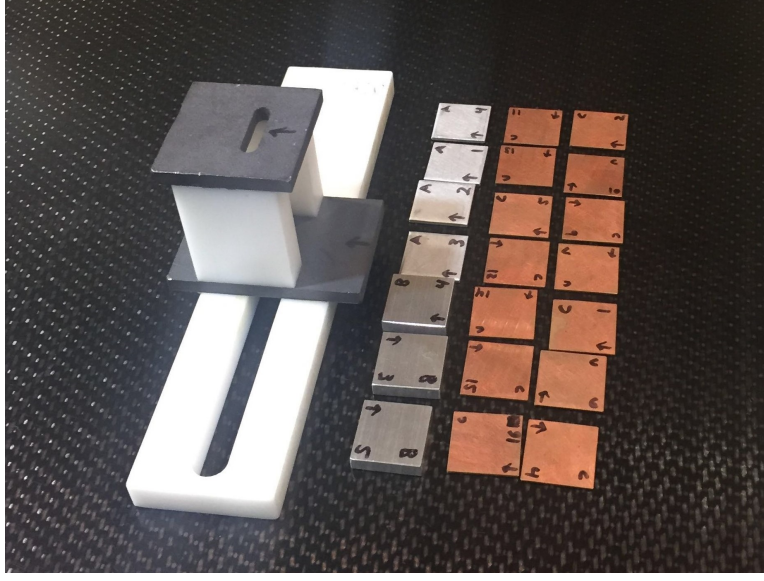
Figure 6.2: The collimator assembly and filters (Al and Cu foils with various thicknesses) used for equivalent spectrum measurement. The photo was taken by Dong Han at Virginia Commonwealth University.

transmissions, i.e.,

$$
\left(\hat{E}_{\mathrm{max}}, \hat{l}_{\mathrm{eq}}\right) = \operatorname*{argmin}_{(E_{\mathrm{max}}, l_{\mathrm{eq}})} \sum_{k} \left(\frac{T_{\mathrm{meas}}^{[k]}}{T_{\mathrm{mdl}}^{[k]}\left(E_{\mathrm{max}}, l_{\mathrm{eq}}\right)} - 1 \right)^{2}, \tag{6.4}
$$

where $T_{\mathrm{meas}}^{[k]}$ is the measured relative transmission of the k-th combination of Al and Cu filters with thicknesses of $l_{\mathrm{Al}}^{[k]}$ and $l_{\mathrm{Cu}}^{[k]}$, respectively, and the expected transmission

$$
\begin{aligned}
& T_{\mathrm{mdl}}^{[k]}\left(E_{\mathrm{max}}, l_{\mathrm{eq}}\right) \\
& = \frac{\sum_{E} \Phi_{\mathrm{BM}}\left(E \,|\, E_{\mathrm{max}}, l_{\mathrm{eq}}\right) D(E) \exp\left(-l_{\mathrm{Al}}^{[k]} \mu_{\mathrm{Al}}(E) - l_{\mathrm{Cu}}^{[k]} \mu_{\mathrm{Cu}}(E) - l_{\mathrm{F}} \mu_{\mathrm{F}}(E)\right)}{\sum_{E} \Phi_{\mathrm{BM}}\left(E \,|\, E_{\mathrm{max}}, l_{\mathrm{eq}}\right) D(E) \exp\left(-l_{\mathrm{F}} \mu_{\mathrm{F}}(E)\right)},
\end{aligned} \tag{6.5}
$$

where $\mu_{\mathrm{F}}(E)$ and l_{F} are the attenuation coefficient and thickness of the Teflon$^{\mathrm{TM}}$ bow-tie filter at the central axis, respectively.
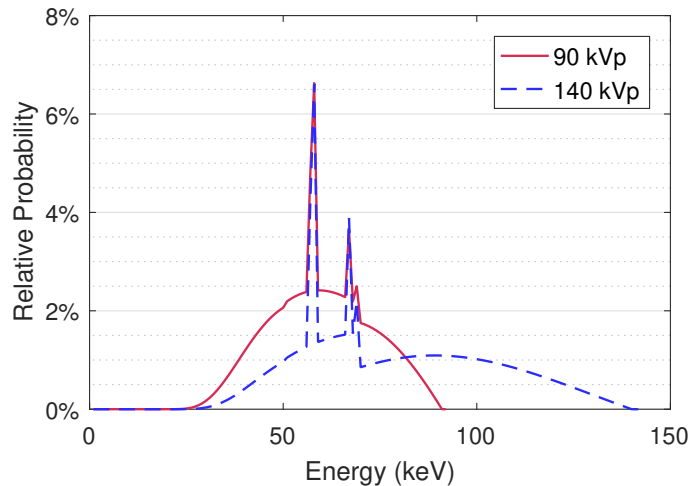
Figure 6.3: The normalized energy-fluence spectra at the central axis of the Philips Brilliance Big Bore CT scanner determined by the equivalent spectrum method.

Table 6.3: The spectrum parameters of the Philips Brilliance Big Bore CT scanner determined by the equivalent spectrum method.

Tube potential	$E_{\max}$ (keV)	l_{eq} (mm)
90 kVp	90	12.1
140 kVp	139	12.9

Then the estimated energy-fluence spectrum is given by

$$
\Psi(y, E) = \frac{\Phi_{\mathrm{BM}}(E|\hat{E}_{\max}, \hat{l}_{\mathrm{eq}})D(E)\exp\left(-l_{\mathrm{F}}(y)\mu_{\mathrm{F}}(E)\right)}{\sum_{E'}\Phi_{\mathrm{BM}}(E'|\hat{E}_{\max}, \hat{l}_{\mathrm{eq}})D(E')\exp\left(-l_{\mathrm{F}}(y)\mu_{\mathrm{F}}(E')\right)} \, . \tag{6.6}
$$

Figure 6.3 shows the experimentally determined energy-fluence spectra of the CT scanner used in our experiment. The fitting parameters of the Birch-Marshall model are shown in Table 6.3.

6.3 Theoretical modeling accuracy

6.3.1 Parameterization of mean excitation energy

Because the elemental compositions of the phantom materials differ from those of typical human tissues, the I-values of the phantom materials deviate from I-value parameterization curves for both the JSIR-BVM method and the image-based HS method (i.e., Figure 3.2 and Figure 2.1, respectively). To minimize the underlying SPR modeling errors due to large differences between compositions of phantom tissue surrogates and actual tissues, phantom-specific I-value parameterizations were generated for both methods using a series of water-alcohol-acetone mixtures and water-$CaCl_2$-K_2HPO_4 mixtures for soft and bony tissue surrogates, respectively.

The parameterization functions were determined to be

$$\ln\left(I/\text{eV}\right) = \begin{cases} -1.746\,r_c + 5.835 & \text{for } r_c \geq 0.75, \\ -0.269\,r_c + 4.551 & \text{for } r_c < 0.75, \end{cases} \tag{6.7}$$

for the JSIR-BVM method and

$$\ln\left(I/\text{eV}\right) = \begin{cases} 0.147\,Z_{\text{eff}} + 3.222 & \text{for } Z_{\text{eff}} \leq 8.5, \\ 0.055\,Z_{\text{eff}} + 3.890 & \text{for } Z_{\text{eff}} > 8.5, \end{cases} \tag{6.8}$$

for the image-based HS method. Figure 6.4 compares the I-value fitting curves derived from the two sets of reference materials (i.e., reference human tissues and mixtures of phantom materials) for the two methods. Figure 6.5 compares the corresponding residual I-value modeling errors predicted using the two sets of fitting curves. The I-values residuals of the phantom-specific parameterization are comparable for the two methods, with the RMS of the
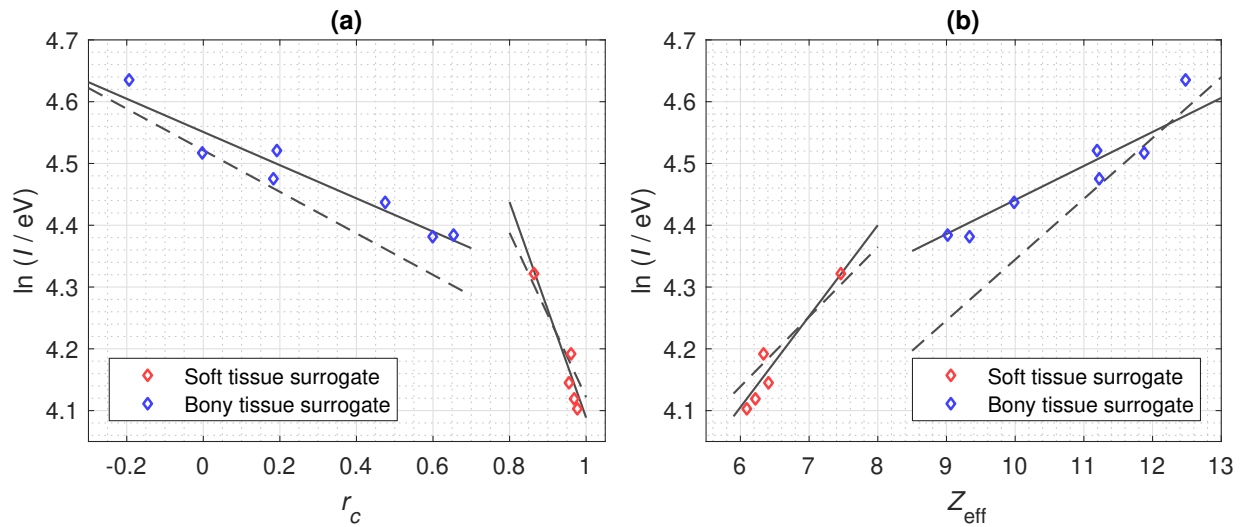
Figure 6.4: *I*-value parameterization curve for (a) JSIR-BVM method and (b) image-based HS method. The solid lines are the phantom-specific parameterization functions that were used in the experiment of tissue-surrogates, while the dashed lines are the tissue-specific parameterization functions generated using reference human tissues.
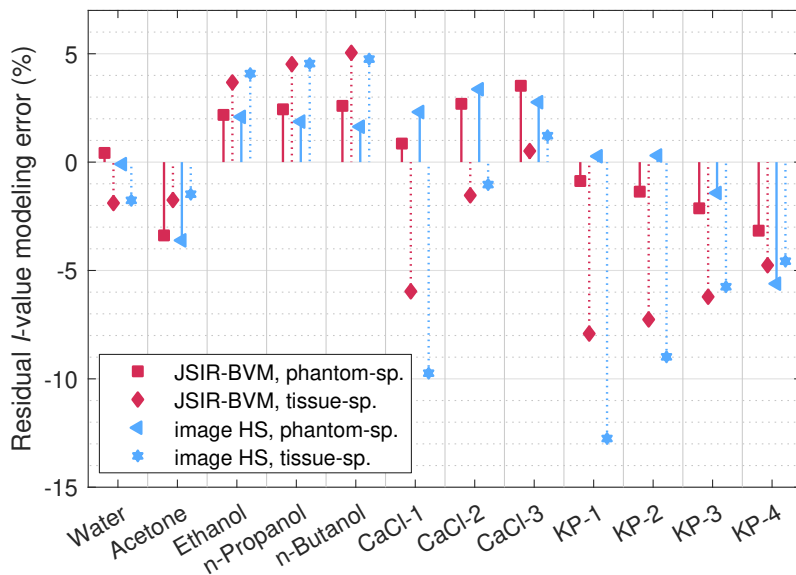
Figure 6.5: Residual *I*-value modeling error for tissue surrogates using phantom- and tissue-specific parameterization functions.

Table 6.4: Residual modeling errors of the two investigated methods.

Material	JSIR-BVM			Image-HS		
	ρ_e (%)	I (%)	S_p (%)	ρ_e (%)	I (%)	S_p (%)
Water	0.12	0.42	0.07	0.00	−0.09	0.01
Acetone	0.02	−3.38	0.42	−0.11	−2.42	0.17
Ethanol	0.00	2.18	−0.25	−0.13	3.26	−0.50
n-Propanol	−0.02	2.43	−0.29	−0.15	3.30	−0.52
n-Butanol	−0.03	2.59	−0.32	−0.16	3.24	−0.53
CaCl-1	0.09	0.86	−0.02	0.00	2.31	−0.28
CaCl-2	0.03	2.69	−0.29	−0.02	3.36	−0.42
CaCl-3	0.00	3.52	−0.42	−0.02	2.76	−0.35
KP-1	0.10	−0.87	0.20	0.00	0.26	−0.03
KP-2	0.08	−1.36	0.25	0.00	0.29	−0.03
KP-3	0.05	−2.13	0.31	0.00	−1.44	0.18
KP-4	0.01	−3.16	0.40	0.00	−5.62	0.71

residual I-value errors being 2.36% and 2.61% for the JSIR-BVM method and the image-based HS method, respectively. On the other hand, the tissue-specific parameterization would result in up to more than 10% of residual I-value errors, with the RMS of 4.84% and 6.19% for the JSIR-BVM method and the image-based HS method, respectively.

6.3.2   SPR modeling error

Table 6.4 shows the intrinsic modeling errors for the JSIR-BVM method and the image-based HS method using theoretically computed CT numbers and BVM component weights. The two methods show comparable modeling accuracy for proton stopping powers of all of the test samples. The recovered electron densities and proton stopping powers are all within 0.2% and 0.8% of the ground truths, respectively. The RMS of SPR modeling error is 0.3% and 0.4% for the JSIR-BVM method and the image-based HS method, respectively.

6.4 Estimation of photon linear attenuation coefficients

Figure 6.6 shows the estimation errors of the photon linear attenuation coefficients reconstructed by the JSIR-BVM method for each test sample within an ROI of 24 mm diameter. Generally, the mean estimation errors decrease with the increasing photon energies. For all samples in both phantom settings, the JSIR-BVM method achieves absolute mean errors of less than 4% for photon energies down to 25 keV. The absolute mean estimation errors for photon energies higher than 50 keV are all less than 1%. The mean predictions are similar for the same sample within the two phantoms of different sizes. The difference is within 1% for photon energies as low as 25 keV.

The 1σ intervals are all within $\pm 2\%$ of the reference values for attenuation coefficients of $E \geq 50$ keV. For lower photon energies, both the mean errors and the standard deviations become larger. For material with relatively low Z_{eff} (i.e., alcohols and acetone in our experiment), the standard deviation is as much as 7% for the photon energy of 25 keV. This result can be explained by the lack of detected low-energy photons.

6.5 Estimation of proton SPR and WEPL

Figure 6.7 and Figure 6.8 shows the SPR images of the head and body phantoms, respectively, reconstructed by the JSIR-BVM method and the image-based HS method. For each test sample, the estimates of ρ_e, I-value, and SPR were evaluated for an ROI of 24 mm diameter and were compared to the ground truth computed from the known compositions and densities. The mean and standard deviation of the estimation errors were computed for each test sample. Additionally, WEPL was computed from the predicted SPR images for
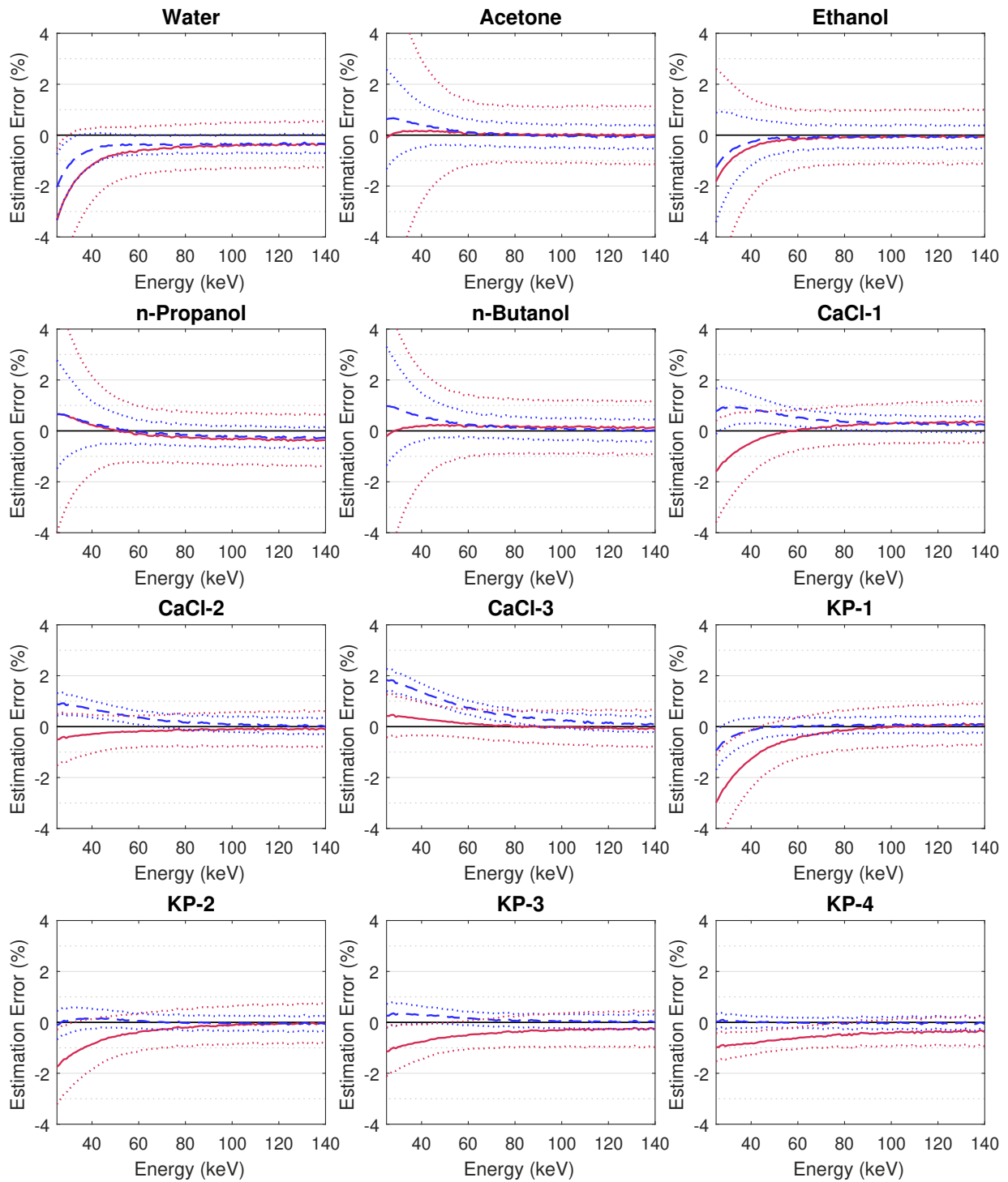
Figure 6.6: The mean estimation error of the linear attenuation coefficients estimated by the JSIR-BVM method for each sample in the head phantom (blue, dashed lines) and the body phantom (red, solid lines). The dotted lines indicate the corresponding standard deviations.
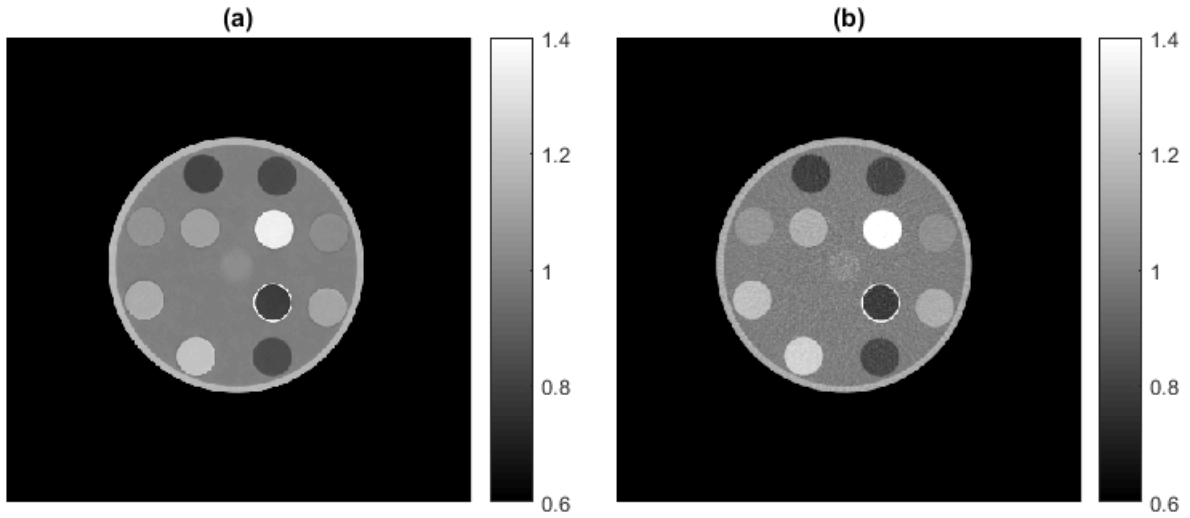
Figure 6.7: The SPR images of the head phantom reconstructed by (a) the JSIR-BVM method and (b) the image-based HS method.
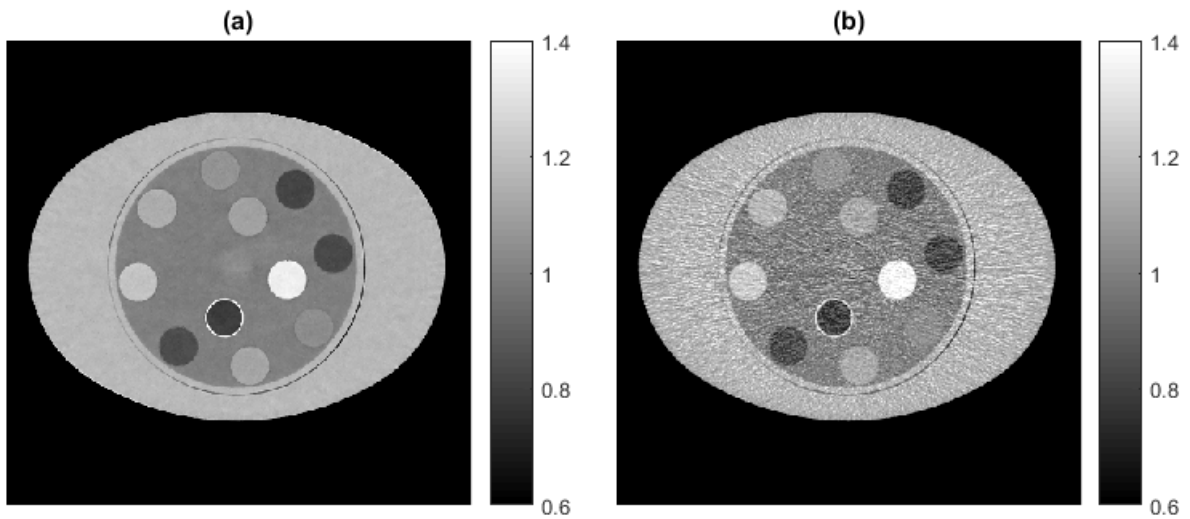
Figure 6.8: The SPR images of the body phantom reconstructed by (a) the JSIR-BVM method and (b) the image-based HS method.

parallel beams from all directions (150 parallel beams with width of 1 mm for every degree). The differences between the WEPLs predicted from the two methods were compared.

Figure 6.9 and Figure 6.10 compare statistics of the estimation errors of the JSIR-BVM method and the image-based HS method for each test sample in the two phantom arrangements.

For the JSIR-BVM method, the mean errors of the estimated electron density and proton SPR are within 0.6% and 0.7% of the theoretically computed ground truth shown in Table 6.1, respectively, for all test samples in both phantom settings, and the mean errors of estimated I-values are all within 1.1% of the modeling residuals. The RMS of the mean estimation errors for electron density and proton SPR are 0.20% and 0.35%, respectively. The accuracy of the JSIR-BVM method on the two different phantom sizes is comparable. The RMS of the mean SPR estimation errors for all test samples in the head and body phantoms are 0.33% and 0.37%, respectively.

In contrast, the image-based HS method exhibits RMS of mean errors of 2.35% and 2.50% for electron density and proton SPR, respectively. The RMS of mean SPR errors for the head and body phantoms are 2.96% and 1.93%, respectively. The image-based method overestimates the electron density for all bony tissue surrogates, which is mainly due to the dependence of CT numbers in the separately reconstructed images on phantom size caused by residual beam hardening effects as shown by the simulation results in Chapter 5. The ρ_e estimation errors can be as much as 5.2% for bony samples in the head phantom, while the maximum ρ_e error is 2.8% for the larger body phantom. The larger error on the smaller head phantom is mainly due to the larger size-difference between the head phantom (215 mm in diameter) and the calibration phantom (330 mm in diameter). The overestimation of ρ_e is the dominant contributor to the overestimation of SPR values up to 5.9% and 3.1% in
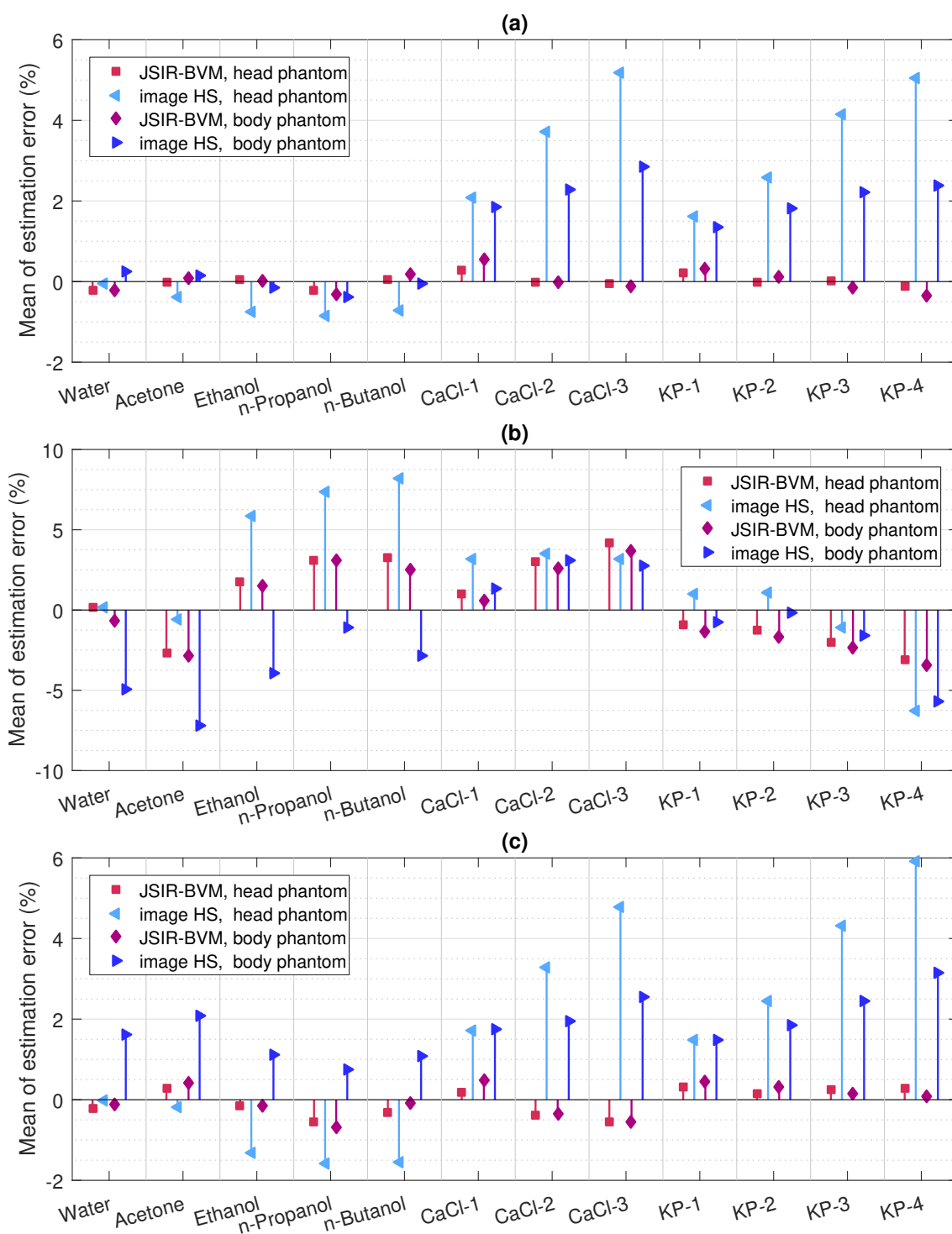
Figure 6.9: Mean estimation errors of (a) electron density, (b) mean excitation energy, and (c) proton SPR for all scanned samples in two phantoms of different sizes.
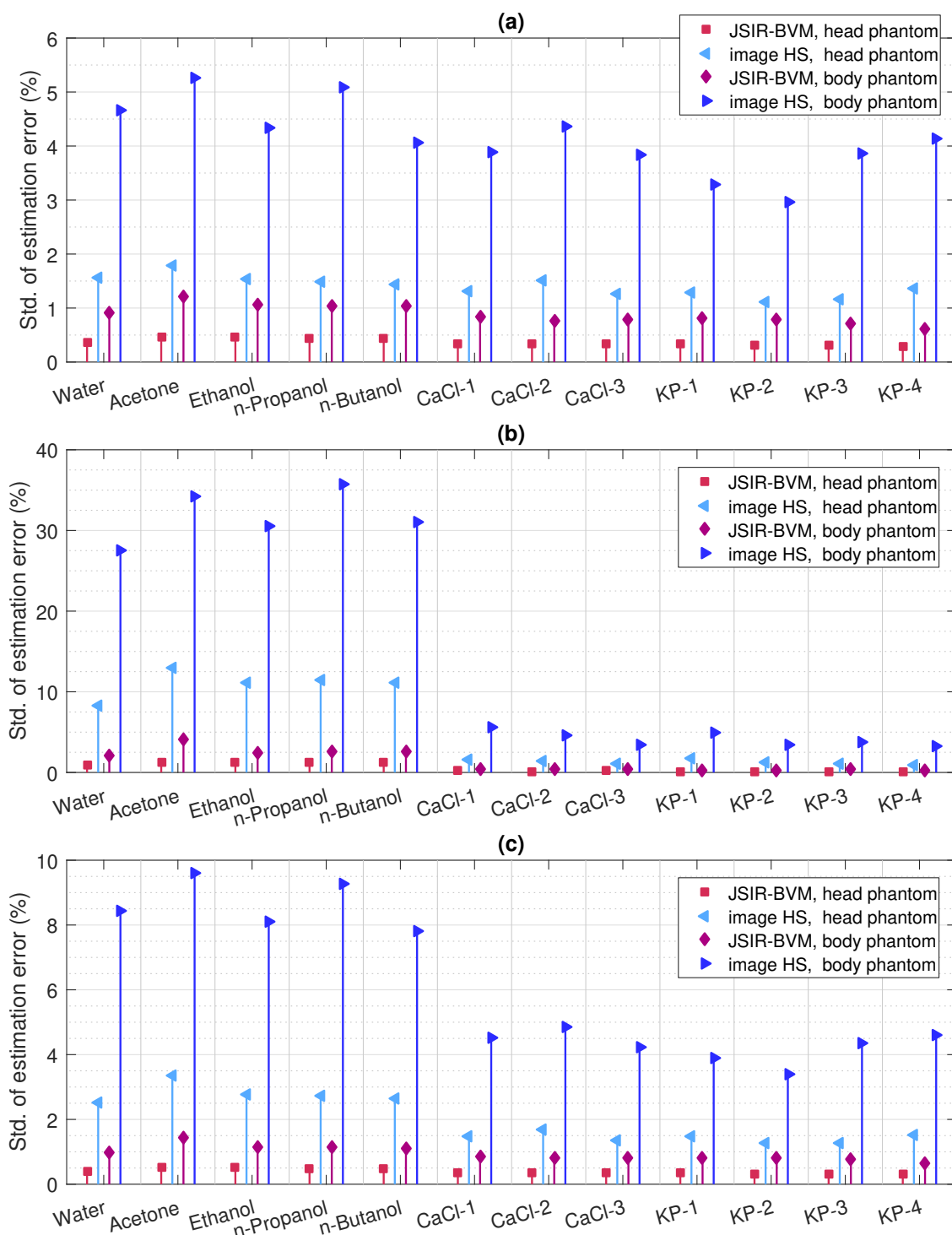
Figure 6.10: Standard deviation (1σ) of estimation errors of (a) electron density, (b) mean excitation energy, and (c) proton SPR for all scanned samples in two phantoms of different sizes.
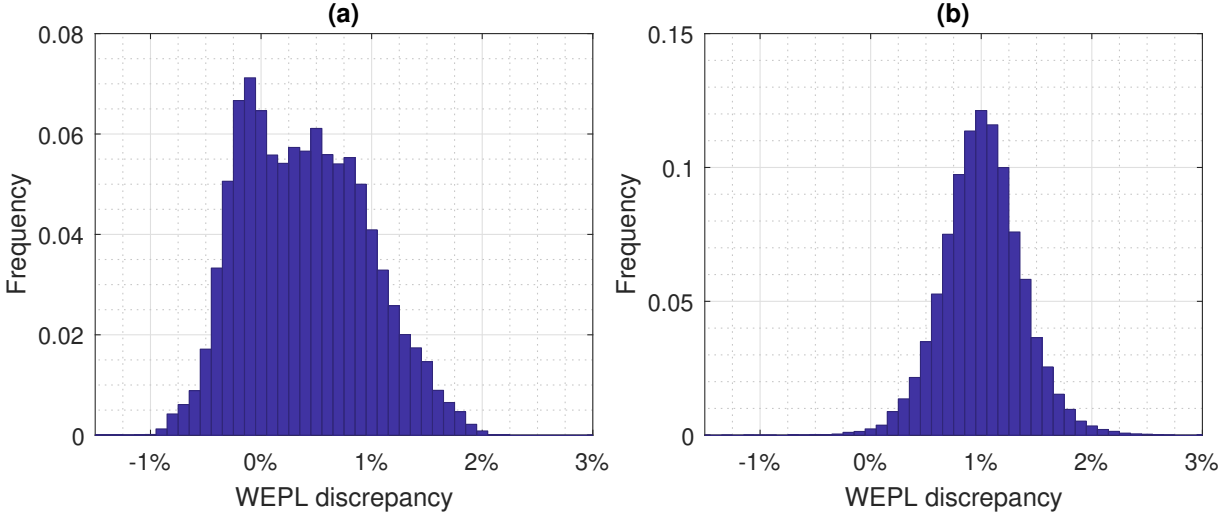
Figure 6.11: The distribution of discrepancy of WEPLs computed from the SPR image estimated by the image-based HS methods versus those estimated by the JSIR-BVM method for (a) the head phantom and (b) the body phantom.

the head and body phantoms, respectively. The largest difference between the mean I-value estimation error and the modeling residual is 6.6% for the image-based HS method.

The JSIR-BVM method also achieves much smaller random errors in SPR values within homogeneous regions. The standard deviation of the SPR estimates is approximately 4-fold to 6-fold less than those of the image-based HS methods for comparable or higher image resolution.

Figure 6.11 compares the difference between the WEPL computed by the two methods. The relative discrepancy was computed as

$$\Delta = 100\% \times \frac{\text{WEPL}_{\text{JSIR-BVM}} - \text{WEPL}_{\text{image-HS}}}{\text{WEPL}_{\text{JSIR-BVM}}} \; . \tag{6.9}$$

The means of absolute discrepancies in WEPL are 0.54% and 1.02% for the head and body phantoms, respectively.

Most of the WEPL values in the body phantom computed from the image-based HS method are larger than those computed from the JSIR-BVM methods, which is consistent with the result that the image-based method overestimates SPRs for all test samples in the body phantom (as shown in Figure 6.9). For the head phantom, there are two peaks of the difference between the two methods, which is due to the overestimation of SPR for bony tissue surrogates and underestimation for alcohols.

6.6 Discussion

6.6.1 Comparison with previous studies

The experimental results show that the proposed JSIR-BVM method is able to achieve accurate proton SPR estimation for various materials and different object sizes from the DECT measurement data. The JSIR-BVM method achieves 0.35% RMS accuracy for all test samples and both phantom settings, which is comparable to the theoretical SPR modeling error. The JSIR-BVM method also achieves more than 4-fold reduction in SPR image noise compared to the image-based method for slightly higher spatial resolution.

On the other hand, although the image-based method can be easily implemented using the scanner-reconstructed images, it would be vulnerable to uncertainties in the scanner-reconstructed CT numbers. Because of the ill-conditioning of the DECT decomposition problem, the random noise and the residual beam hardening effects in the CT images are amplified in the predicted SPR images. The residual beam-hardening effect in separately reconstructed images leads to size- and position-dependence of the reconstructed CT numbers and therefore introduces uncertainties into predicted SPR values [21]. Our implementation of the image-based method overestimates the electron densities and SPRs for the higher

Z_{eff} materials when the test object is much smaller than the calibration phantom, which is consistent with the previous simulation results in Chapter 5. In realistic CT systems, the imperfection of the beam-hardening correction (e.g., the reconstructed HU of a homogeneous water phantom may not uniformly be zero) and other data preprocessing steps also contribute to the CT number variations. Additionally, uncertainties of known compositions and densities of tissue substitutes used in the calibration process may also impact the performance of calibration-based methods. Therefore, for calibration-based methods an accurate determination of density and elemental composition of the calibration phantom should be performed at least once prior to calibration scans to mitigate such uncertainties.

It should be noted that the performance of all DECT methods depends on the scanning protocol. Our experiment used the 90 kVp and 140 kVp energy-pair, which is the maximum spectral separation available on the Philips Brilliance Big Bore CT scanner. Garcia *et al.* [18] presented a 1.9% absolute-mean error on electron density for an 80 kVp and 140 kVp spectrum-pair and a relatively small size-difference, which is similar to our result on the body phantom. Several studies have shown that a larger spectrum separation, which is generally realized via additional $0.4 - 0.8$ mm Sn filters for the high-energy beam, reduces the ill-conditioning of the DECT decomposition problem and improves the estimation accuracy of both image- and sinogram-based methods [26,63,104]. Hünemohr *et al.* [71] and Almeida *et al.* [104] showed the estimation error on electron density of their test samples are all within 1.2% for an 80 kVp and 140 kVp/Sn energy-pair. Li *et al.* [21] showed that under the largest achievable spectrum separation among current commercial DECT scanners (i.e., 80 kVp and 150 kVp/Sn energy-pair), the CT number variations in similar head- and body-sized phantoms can cause 0.9% and 1.8% SPR uncertainties for soft and bony tissues, respectively.

6.6.2 SPR estimation uncertainty of the JSIR-BVM method

As stated in Section 5.6, the overall uncertainty of the estimated SPR are mainly from two sources:

1. The SPR modeling uncertainty, i.e., the estimation error of electron density, mean excitation energy, and SPR from the BVM model using the theoretical BVM component weights, (c_1^*, c_2^*), which are computed as in Section 3.4;

2. The image formation uncertainty, i.e., the uncertainties in the reconstructed BVM component weights from experimental DECT measurements when compared to the theoretical BVM component weights.

These two uncertainty sources are independent of each other and therefore can be considered separately.

The SPR modeling uncertainty has been investigated in Chapter 5, and the results show that the BVM maintains good theoretical modeling accuracy over a wide range of component variations of typical human tissues. It should be noted that throughout this dissertation, we neglect the approximation errors of the reference SPR value computed by the Bethe equation and the reference I-value computed by the Bragg additivity rule, because these approximation errors are not directly related to CT-based approaches.

On the other hand, the uncertainty of the BVM component weights due to the image formation process also leads to uncertainty in the SPR. By combining (1.15), (3.2), (3.3), and (6.7), the estimation of SPR of the phantom materials can be equivalently rewritten in terms

of the BVM component weights as

$$\text{SPR} = \frac{S_p}{S_{p,\text{w}}} = \begin{cases} 1.056\,c_1 + 0.973\,c_2 & \text{for } r_c \geq 0.75, \\ 1.033\,c_1 + 1.154\,c_2 & \text{for } r_c < 0.75. \end{cases} \tag{6.10}$$

Without loss of generality, we write

$$\text{SPR} = \nu_1 c_1 + \nu_2 c_2\,, \tag{6.11}$$

where ν_1 and ν_2 are the corresponding coefficients.

By applying the law of uncertainty propagation [105, 106], the Type A or Type B image-formation uncertainty of SPR, σ_{SPR}, can be written as

$$\sigma_{\text{SPR}}^2 = \begin{bmatrix} \nu_1 & \nu_2 \end{bmatrix} \Sigma_c \begin{bmatrix} \nu_1 \\ \nu_2 \end{bmatrix}\,, \tag{6.12}$$

where

$$\Sigma_c = \begin{bmatrix} \sigma_{c_1}^2 & \text{cov}(c_1, c_2) \\ \text{cov}(c_1, c_2) & \sigma_{c_2}^2 \end{bmatrix} \tag{6.13}$$

is the uncertainty covariance matrix of the reconstructed BVM component weights.

There are two major sources of the image formation uncertainty: the first one is the noise and errors presented in the measurement data, and the second one is the inaccuracy of the CT forward data modeling, i.e., the inaccuracy of the forward-model parameters listed in Section 6.2.

Table 6.5: Bias and standard deviation of the estimated SPR due to the image-formation process in the experiment.

Material	Head phantom		Body phantom	
	$\frac{\Delta_{\mathrm{SPR}}}{\mathrm{SPR}}$ (%)	$\frac{\sigma_{\mathrm{SPR}}}{\mathrm{SPR}}$ (%)	$\frac{\Delta_{\mathrm{SPR}}}{\mathrm{SPR}}$ (%)	$\frac{\sigma_{\mathrm{SPR}}}{\mathrm{SPR}}$ (%)
Water	−0.30	0.40	−0.19	0.99
Acetone	−0.12	0.53	0.00	1.45
Ethanol	0.08	0.51	0.11	1.15
n-Propanol	−0.27	0.47	−0.38	1.13
n-Butanol	−0.00	0.48	0.23	1.10
CaCl-1	0.19	0.34	0.49	0.85
CaCl-2	−0.09	0.34	−0.04	0.80
CaCl-3	−0.13	0.34	−0.14	0.81
KP-1	0.12	0.34	0.26	0.82
KP-2	−0.09	0.32	0.08	0.81
KP-3	−0.06	0.32	−0.17	0.75
KP-4	−0.13	0.31	−0.32	0.63

A full analysis of the Type B image formation uncertainty requires knowledge of uncertainties associated with x-ray source spectra and scattered radiation, which are not currently available and will be addressed in future work. Insight into the impact of Type B uncertainties on estimated SPR can be gained by examining the bias of the reconstructed values for several ROIs. For each ROI, the Type B uncertainties lead to uncertainties in the bias of the reconstructed BVM component weights, and through (6.12) into uncertainties in SPR. Denote the bias of reconstructed BVM component weights by $\Delta c_i = \bar{c}_i - c_i^*$, where c_i^* is the theoretical BVM weight of a single phantom material and $\bar{c}_i$ is the reconstructed BVM component weights averaged over the corresponding ROI of the material. The bias values of BVM component weights for all ROIs in the head and body phantoms are shown in Figure 6.12. The bias in SPR can be found simply as

$$\Delta_{\mathrm{SPR}} = \nu_1 \Delta c_1 + \nu_2 \Delta c_2 \,. \tag{6.14}$$

As shown in Table 6.5, Δ_{SPR} is less than 0.5% for all ROIs in both phantoms.
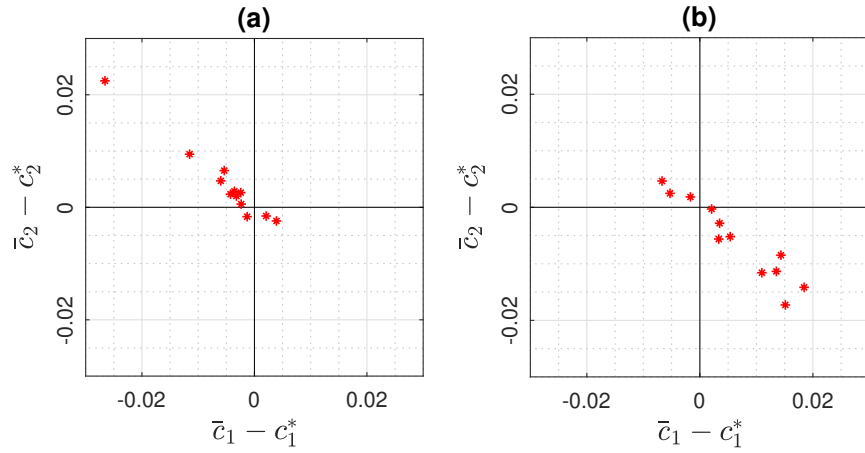
Figure 6.12: The bias of reconstructed BVM component weights relative to the theoretical values for each of the 12 ROIs in the (a) head and (b) body phantom.
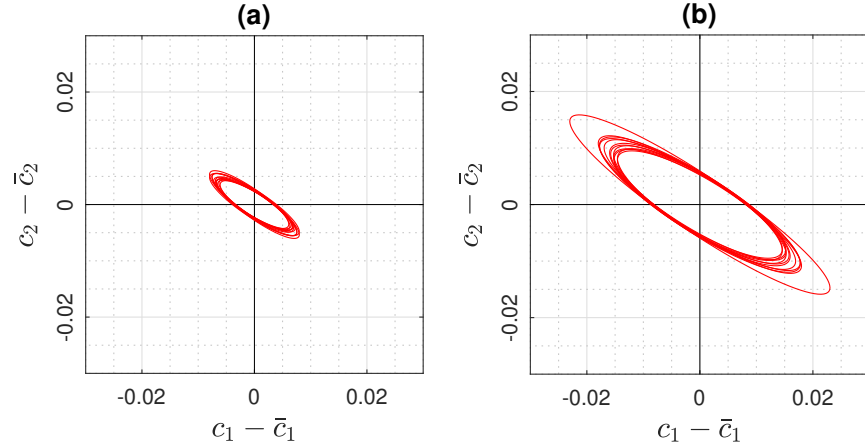
Figure 6.13: The one standard deviation ellipse corresponding to the covariance matrix for each of the 12 ROIs in the (a) head and (b) body phantom.

To estimate Type A image formation uncertainties in our experiment, the covariance matrix of reconstructed BVM component weights is computed for each of the phantom inserts as

$$\Sigma_c = \frac{1}{N} \sum_{x \in R} \begin{bmatrix} (c_1(x) - \bar{c}_1)^2 & (c_1(x) - \bar{c}_1)(c_2(x) - \bar{c}_2) \\ (c_1(x) - \bar{c}_1)(c_2(x) - \bar{c}_2) & (c_2(x) - \bar{c}_2)^2 \end{bmatrix}, \tag{6.15}$$

where R is the ROI of a single material and N is the number of pixels in the ROI. Figure 6.13 graphically illustrates the covariance matrices of all phantom insert ROIs in the head and body phantoms in terms of the one-standard-deviation ellipses.[4] Note that the covariance matrix of BVM component weights would depend on the scanned object and the regularization in the reconstruction, while the covariance matrices of different materials and different locations in the same object are similar. The result indicates the Type A uncertainties of the two BVM component weights at the same image location exhibit high negative correlation. Evaluating (6.12) yields Type A image formation uncertainties around 0.4% and 1.0% for test samples in head and body phantoms, respectively (shown in Table 6.5).

---

[4]The one-standard-deviation ellipse is parameterized as $\begin{bmatrix} c_1 - \bar{c}_1 & c_2 - \bar{c}_2 \end{bmatrix} \Sigma_c^{-1} \begin{bmatrix} c_1 - \bar{c}_1 \\ c_2 - \bar{c}_2 \end{bmatrix} = 1$.

Chapter 7

Conclusions and future work

In this dissertation, we implemented and evaluated a novel DECT approach for proton SPR mapping based on a JSIR algorithm. We integrated both CT image reconstruction and proton stopping power mapping under the same framework of a linear, separable BVM for material characterization. By taking advantage of an accurate polychromatic CT data model and a model-based DECT statistical reconstruction algorithm, the proposed JSIR-BVM method achieves much better accuracy and precision on proton SPR estimation when compared with image- and sinogram-domain decomposition methods in both simulation and experimental settings. To our knowledge, our method is the first application of a statistical reconstruction algorithm that operates simultaneously on two DECT sinograms extracted from a clinical scanner for mapping proton stopping power. The result suggests that the JSIR-BVM method has the potential for better SPR prediction in clinical settings.

We also explored the convergence of the image reconstruction algorithm used in the JSIR-BVM method. We analyzed the major reasons for the slow convergence of the original DE-AM algorithm and proposed modified algorithms to deal with these issues. The modified algorithm achieves approximately the same convergence as the SE-AM algorithm and can be combined with other acceleration strategies that are developed for the SE-AM algorithm.

The result ensures the modified reconstruction algorithm feasible to be further implemented in clinical settings.

To make this study more general and clinically applicable, there are also several problems to be considered in future work.

For all evaluations presented in this dissertation, the reference SPRs of the test samples, which were computed from the known densities and elemental compositions, served as the ground truth. As stated in Section 1.2.4, the impact of the approximating error of the theoretical computation was not addressed in this study because it does not differ between different CT-based approaches. Experimental evaluation that utilizes the directly measured SPRs will be carried out in future work.

In the implemented reconstruction algorithm, the regularization parameters were selected as a trade-off between image noise and image resolution. The selection of the parameters ensures the spatial resolution of the images reconstructed by the regularized DE-AM algorithm is comparable to or slightly higher than the FBP-reconstructed images in the completing methods for typical soft tissue contrast in a piecewise uniform phantom. Optimization of the regularization parameters for different regions of patient body should be addressed in future work.

In the presented experimental phantom study, the scattered radiation was restricted by narrow collimation available on the clinical scanner and was not taken into consideration. Under relatively wide collimation, unaccounted scatter may cause artifacts in the reconstructed images, which can compromise the performance of quantitative DECT. There is ongoing work in investigating the impact and correction of the scattered radiation contamination based on determining the scattered radiation via both Monte Carlo simulation and a beam-block measurement on the scanner.

Towards the application of the proposed method on patient data, a more comprehensive analysis of the SPR estimation uncertainty should be addressed in the future. Such uncertainty analysis requires the quantification of the uncertainties of those quantities required in the JSIR-BVM methods, among which two major ones are the scattered radiation contamination and the equivalent spectrum modeling. To learn about the impact of the uncertainties related to spectrum modeling, one potential way is to study the variation of the experimentally measured transmission data for various materials that are representative of typical tissues.

Appendix A

Reference human tissue properties

This appendix summarizes the compositions of reference human tissues used in the present study, which are taken from [91–93]. The mass densities, electron densities, mean excitation energies (computed via the Bragg additivity rule), and the mass fraction of six major elements are listed. Other elements include Na, Mg, S, Cl, K, Fe and I (only appears in thyroid).

Table A.1: Radiological properties and elemental compositions of reference soft tissues.

Tissue	ρ (g/mL)	$\rho_e/\rho_{e,\text{w}}$	I (eV)	Elemental mass Fraction						
				H	C	N	O	P	Ca	other
adipose 1	0.97	0.97	66.3	11.2	51.7	1.3	35.5			0.3
adipose 2	0.95	0.95	64.8	11.4	59.8	0.7	27.8			0.3
adipose 3	0.93	0.93	63.2	11.6	68.1	0.2	19.8			0.3
adrenal grand	1.03	1.02	71.2	10.6	28.4	2.6	57.8	0.1		0.5
aorta	1.05	1.04	75.2	9.9	14.7	4.2	69.8	0.4	0.4	0.6
bladder, empty	1.04	1.03	75.0	10.5	9.6	2.6	76.1	0.2		1.0
bladder, filled	1.03	1.03	75.7	10.8	3.5	1.5	83.0	0.1		1.1
bladder, urine	1.02	1.02	75.9	11.0	0.5	1.0	86.2	0.1		1.2
blood, erythrocytes	1.09	1.07	74.8	9.5	19.0	5.9	64.6	0.1		0.9
blood, vessels	1.05	1.04	75.1	9.9	14.7	4.2	69.9	0.4		0.9
blood, whole	1.06	1.05	75.2	10.2	11.0	3.3	74.5	0.1		0.9
brain	1.04	1.03	73.9	10.7	14.5	2.2	71.2	0.4		1.0
brain, CSF	1.01	1.01	75.8	11.1			88.0			0.9
brain, gray matter	1.04	1.04	74.8	10.7	9.5	1.8	76.7	0.3		1.0
brain, white matter	1.04	1.03	73.1	10.6	19.4	2.5	66.1	0.4		1.0
breasts	0.97	0.97	66.6	11.1	51.0	1.5	36.1			0.3

Tissue	ρ (g/mL)	$\rho_e/\rho_{e,\mathrm{w}}$	I (eV)	Elemental mass Fraction						
				H	C	N	O	P	Ca	other
mammary gland 1	0.99	0.99	66.9	10.9	50.6	2.3	35.8	0.1		0.3
mammary gland 2	1.02	1.01	70.3	10.6	33.2	3.0	52.7	0.1		0.4
mammary gland 3	1.06	1.05	74.0	10.2	15.8	3.7	69.8	0.1		0.4
cell nucleus	1.00	0.99	75.5	10.6	9.0	3.2	74.2	2.6		0.4
connective tissue	1.12	1.10	74.7	9.4	20.7	6.2	62.2			1.5
eye lens	1.07	1.05	74.3	9.6	19.5	5.7	64.6	0.1		0.5
eyes	1.02	1.02	75.0	10.7	6.9	1.7	80.3	0.1		0.3
gallbladder bile	1.03	1.03	75.2	10.8	6.1	0.1	82.2			0.8
GI tract contents	1.03	1.02	73.9	1.0	22.2	2.2	64.4	0.2	0.1	0.9
small intestine	1.03	1.02	74.3	10.6	11.5	2.2	75.1	0.1		0.5
stomach	1.05	1.04	74.2	10.4	13.9	2.9	72.1	0.1		0.6
heart 1	1.05	1.04	73.8	10.3	17.5	3.1	68.1	0.2		0.8
heart 2	1.05	1.04	74.3	10.4	13.9	2.9	71.8	0.2		0.8
heart 3	1.05	1.04	75.0	10.4	10.3	2.7	75.6	0.2		0.8
heart, blood filled	1.06	1.05	74.8	10.3	12.1	3.2	73.4	0.1		0.9
kidney 1	1.05	1.04	74.3	10.2	16.0	3.4	69.3	0.2	0.1	0.8
kidney 2	1.05	1.04	74.7	10.3	13.2	3.0	72.4	0.2	0.1	0.8
kidney 3	1.05	1.04	75.0	10.4	10.6	2.7	75.2	0.2	0.1	0.8
liver 1	1.05	1.04	74.4	10.3	15.6	2.7	70.1	0.3		1.0
liver 2	1.06	1.05	74.8	10.2	13.9	3.0	71.6	0.3		1.0
liver 3	1.07	1.06	75.2	10.1	12.6	3.3	72.7	0.3		1.0
lung, deflated	0.26	0.26	75.2	10.3	10.5	3.1	74.9	0.2		1.0
lung, inflated	1.05	1.04	75.2	10.3	10.5	3.1	74.9	0.2		1.0
lung, parenchyma	1.05	1.04	75.3	10.3	10.1	2.9	75.5	0.2		1.0
lymph	1.03	1.03	75.5	10.8	4.1	1.1	83.2			0.8
miscellaneous glands	1.05	1.04	74.9	10.5	10.0	2.3	76.3	0.1		0.8
muscle skeletal 1	1.05	1.04	74.3	10.1	17.1	3.6	68.1	0.2		0.9
muscle skeletal 2	1.05	1.04	74.6	10.2	14.3	3.4	71.0	0.2		0.9
muscle skeletal 3	1.05	1.04	75.3	10.2	11.2	3.0	74.5	0.2		0.9
ovary	1.05	1.04	75.0	10.5	9.3	2.4	76.8	0.2		0.8
pancreas	1.04	1.03	73.4	10.6	16.9	2.2	69.4	0.2		0.7
prostate	1.04	1.03	75.0	10.5	8.9	2.5	77.4	0.1		0.6
cartilage	1.10	1.08	78.0	9.6	9.9	2.2	74.4	2.2		1.7
marrow, red	1.03	1.02	69.2	10.5	41.4	3.4	43.9	0.2		0.6
marrow, yellow	0.98	0.98	63.9	11.5	64.4	0.7	23.1			0.3
skin 1	1.09	1.08	72.8	10.0	25.0	4.6	59.4	0.1		0.9
skin 2	1.09	1.08	73.7	10.0	20.4	4.2	64.5	0.1		0.8
skin 3	1.09	1.08	74.4	10.1	15.8	3.7	69.5	0.1		0.8
spleen	1.06	1.05	75.0	10.3	11.3	3.2	74.1	0.3		0.8

148

Tissue	ρ (g/mL)	$\rho_e/\rho_{e,w}$	I (eV)	Elemental mass Fraction						
				H	C	N	O	P	Ca	other
				(continued)						
testis	1.04	1.03	74.7	10.6	9.9	2.0	76.6	0.1		0.8
thyroid	1.05	1.04	74.7	10.4	11.9	2.4	74.5	0.1		0.7
trachea	1.06	1.05	75.0	10.1	13.9	3.3	71.3	0.4		1.0

Table A.2: Radiological properties and elemental compositions of reference bony tissues.

Tissue	ρ (g/mL)	$\rho_e/\rho_{e,w}$	I (eV)	Elemental mass Fraction						
				H	C	N	O	P	Ca	other
cortical bone	1.92	1.78	112.0	3.4	15.5	4.2	43.5	10.3	22.5	0.6
spongiosa	1.18	1.15	78.4	8.5	40.4	2.8	36.7	3.4	7.4	0.8
femur	1.33	1.28	87.0	7.0	34.5	2.8	36.8	5.5	12.9	0.5
– total bone	1.42	1.35	90.5	6.3	33.3	2.9	36.2	6.6	14.3	0.4
– conical troch.	1.36	1.31	86.9	6.9	36.6	2.7	34.7	5.9	12.8	0.4
– cylindrical shaft	1.75	1.64	105.5	4.2	20.4	3.8	41.5	9.3	20.2	0.6
– spherical head	1.33	1.28	85.7	7.1	37.9	2.6	34.2	5.6	12.2	0.4
– whole specimen	1.43	1.36	90.6	6.3	33.1	2.9	36.3	6.6	14.4	0.4
humerus										
– total bone	1.46	1.39	92.5	6.0	31.4	3.1	36.9	7.0	15.2	0.4
– cylindrical shaft	1.49	1.41	93.9	5.8	30.1	3.2	37.4	7.2	15.8	0.5
– spherical head	1.33	1.28	85.7	7.1	37.9	2.6	34.2	5.6	12.2	0.4
– whole specimen	1.39	1.33	88.3	6.7	35.2	2.8	35.2	6.2	13.5	0.4
clavicle (M)	1.46	1.39	92.5	6.0	31.3	3.1	37.0	7.0	15.2	0.4
sternum (M)	1.25	1.21	82.4	7.8	31.6	3.7	43.8	4.0	8.5	0.6
cranium	1.61	1.52	100.0	5.0	21.2	4.0	43.5	8.1	17.6	0.6
mandible	1.68	1.58	102.7	4.6	19.9	4.1	43.5	8.6	18.7	0.6
innominate (F)	1.46	1.39	93.2	6.0	25.0	3.9	43.5	6.6	14.3	0.7
innominate (M)	1.41	1.35	91.1	6.3	26.2	3.9	43.6	6.1	13.2	0.7
sacrum (F)	1.39	1.33	89.6	6.6	27.1	3.8	43.5	5.8	12.5	0.7
sacrum (M)	1.29	1.24	84.6	7.4	30.2	3.7	43.8	4.5	9.8	0.6
rib (M)										
– 10th	1.52	1.44	95.9	5.6	23.5	4.0	43.4	7.2	15.6	0.7
– 2nd/6th	1.41	1.35	90.7	6.4	26.3	3.9	43.6	6.0	13.1	0.7
vertebral (M)										
– C4 ex.	1.42	1.36	91.2	6.3	26.1	3.9	43.6	6.1	13.3	0.7
– C4 in.	1.38	1.32	89.8	6.6	24.3	3.7	47.1	5.7	11.9	0.7
– D6/L3 ex.	1.33	1.28	87.0	7.0	28.7	3.8	43.7	5.1	11.1	0.6
– D6/L3 in.	1.30	1.25	85.8	7.3	26.5	3.6	47.3	4.8	9.8	0.7
– whole column	1.33	1.28	87.0	7.1	25.8	3.6	47.2	5.1	10.5	0.7

Appendix B

Alternating minimization (AM) algorithm

This appendix summarizes the AM algorithm that is originally described in [41] and [42]. The notation used in this appendix is defined in Section 1.3.

The polychromatic CT data are modeled as

$$Q_j(y) = I_{0,j}(y) \sum_E \psi_j(y, E) \exp\Big(-\sum_x h(y|x) \sum_i \mu_i(E) c_i(x)\Big) + \gamma_j(y),\tag{B.1}$$

where $i \in \{1, 2\}$ and $j \in \{\mathrm{L}, \mathrm{H}\}$ for the DECT data modeled by the BVM.

Note that the generalized forward CT data model given above is not limited to the dual-energy, two-bases case used in the proposed JSIR-SPR method. The model can be reduced into monochromatic and polychromatic single-energy cases, or be extended to multi-energy or multi-bases cases. The AM algorithms for all model categories are summarized below in the generalized form.

B.1 AM algorithm

Based on the Poisson statistics, the MLE problem is formulated as minimization of the following I-divergence,

$$g(\mathbf{c}) = d_I \left(\mathbf{d} \parallel \mathbf{Q}\right) = \sum_j \sum_y \left(d_j(y) \ln \frac{d_j(y)}{Q_j(y)} - d_j(y) + Q_j(y)\right), \tag{B.2}$$

subject to the nonnegativity constraint $c_i(x) \geq 0$.

Definition B.1. *The exponential family $\mathcal{E}$ is the set*

$$\mathcal{E} = \left\{ \mathbf{q} : q_j(y, E) = I_{0,j}(y)\psi_j(y, E) \exp\left(-\sum_x h(y|x) \sum_i \mu_i(E) c_i(x)\right) \text{ for } E > 0, \right.$$

$$\left. q_j(y, 0) = \gamma_j(y) \right\}.$$

The exponential family $\mathcal{E}$ defines the CT forward data model, where

$$Q_j(y) = \sum_{E \geq 0} q_j(y, E). \tag{B.3}$$

A dummy energy value $E = 0$ is included to account for the background events. Without loss of generality, in the following all summations over E are assumed to include the dummy variable $E = 0$ with $\mu_i(0) = 0$ for all i.

Definition B.2. *The linear family $\mathcal{L}(\mathbf{d})$ is the set*

$$\mathcal{L}(\mathbf{d}) = \left\{ \mathbf{p} : p_j(y, E) \geq 0, \ \sum_E p_j(y, E) = d_j(y) \right\}.$$

Lemma B.1. *The I-divergence (B.2)*

$$d_I\left(\mathbf{d} \parallel \mathbf{Q}\right) \leq d_I\left(\mathbf{p} \parallel \mathbf{q}\right) \quad \forall \mathbf{p} \in \mathcal{L}(\mathbf{d}),\tag{B.4}$$

where

$$d_I\left(\mathbf{p} \parallel \mathbf{q}\right) = \sum_j \sum_y \sum_E \left(p_j(y, E) \ln \frac{p_j(y, E)}{q_j(y, E)} - p_j(y, E) + q_j(y, E)\right).\tag{B.5}$$

The equality holds if and only if

$$p_j(y, E) = d_j(y) \frac{q_j(y, E)}{\sum_{E'} q_j(y, E')}.\tag{B.6}$$

To prove this lemma, a Lagrange multiplier $\boldsymbol{\nu}$ is introduced to enforce the equality of $\mathbf{p} \in \mathcal{L}(\mathbf{d})$ to get the Lagrangian

$$\begin{aligned} L = \sum_j \sum_y \sum_E & \left(p_j(y, E) \ln \frac{p_j(y, E)}{q_j(y, E)} - p_j(y, E) + q_j(y, E)\right) \\ & + \sum_j \sum_y \nu_j(y) \left(d_j(y) - \sum_E p_j(y, E)\right). \end{aligned}\tag{B.7}$$

Minimizing over $p_j(y, E)$ and solving for $\boldsymbol{\nu}$ to enforce equality yields (B.6). Substituting the result back into the I-divergence yields the equality in the Lemma statement.

For an estimate of $\mathbf{q}$ denoted $\hat{\mathbf{q}}$ with corresponding estimate $\hat{\mathbf{c}}$, let

$$\hat{\mathbf{p}} = \operatorname*{argmin}_{\mathbf{p} \in \mathcal{L}(\mathbf{d})} d_I\left(\mathbf{p} \parallel \hat{\mathbf{q}}\right),\tag{B.8}$$

which is given in closed form as (B.6).

Then original objective function (B.2) is upper-bounded by a surrogate function as

$$
\begin{aligned}
g(\mathbf{c}) &\leq \sum_j \sum_y \sum_E \left[\hat{p}_j(y, E) \ln \frac{\hat{p}_j(y, E)}{q_j(y, E)} - \hat{p}_j(y, E) + q_j(y, E) \right] \\
&= \sum_j \sum_y \sum_E \left[-\hat{p}_j(y, E) \ln \left(q_j(y, E) \right) + q_j(y, E) \right] + C \\
&= \sum_j \sum_y \sum_E \left[-\hat{p}_j(y, E) \left(-\sum_x h(y|x) \sum_i \mu_i(E) c_i(x) \right) + q_j(y, E) \right] + C \\
&= \sum_j \sum_y \sum_E \left[\hat{p}_j(y, E) \left(\sum_x h(y|x) \sum_i \mu_i(E) c_i(x) \right) \right. \\
&\qquad \left. + \hat{q}_j(y, E) \exp \left(-\sum_x h(y|x) \sum_i \mu_i(E) \left(c_i(x) - \hat{c}_i(x) \right) \right) \right] + C \\
&= g^{\mathrm{sur}}(\mathbf{c} : \hat{\mathbf{c}}),
\end{aligned}
\tag{B.9}
$$

where the constant C is independent of $\mathbf{c}$. Moreover, the surrogate function has the same function value and gradient as the original function at $\mathbf{c} = \hat{\mathbf{c}}$, i.e.,

$$
\left. g^{\mathrm{sur}}(\mathbf{c} : \hat{\mathbf{c}}) \right|_{\mathbf{c}=\hat{\mathbf{c}}} = \left. g(\mathbf{c}) \right|_{\mathbf{c}=\hat{\mathbf{c}}}, \tag{B.10}
$$

$$
\left. \nabla g^{\mathrm{sur}}(\mathbf{c} : \hat{\mathbf{c}}) \right|_{\mathbf{c}=\hat{\mathbf{c}}} = \left. \nabla g(\mathbf{c}) \right|_{\mathbf{c}=\hat{\mathbf{c}}}. \tag{B.11}
$$

Because the original objective function $g(\mathbf{c})$ is upper-bounded by the surrogate function $g^{\mathrm{sur}}(\mathbf{c} : \hat{\mathbf{c}})$, any update that decreases $g^{\mathrm{sur}}(\mathbf{c} : \hat{\mathbf{c}})$ essentially ensures decrease of $g(\mathbf{c})$.

The alternative minimization of the surrogate function may also be considered in another way as a double minimization problem formulated as

$$
\min_{\mathbf{q} \in \mathcal{E}} \min_{\mathbf{p} \in \mathcal{L}(\mathbf{d})} d_I \left(\mathbf{p} \| \mathbf{q} \right). \tag{B.12}
$$

The algorithm alternates between the estimation of $\mathbf{p} \in \mathcal{L}(\mathbf{d})$ and $\mathbf{q} \in \mathcal{E}$.

Lemma B.2. *(Convex decomposition lemma) Suppose that f is a convex function defined on a convex cone $\mathcal{D} \subset \mathbb{R}^n$. Given $\boldsymbol{\tau}_k \in \mathcal{D}$,*

$$f\left(\sum_k \boldsymbol{\tau}_k\right) \leq \sum_k r_k f\left(\frac{1}{r_k}\boldsymbol{\tau}_k\right) \tag{B.13}$$

for all $\mathbf{r} \in \mathcal{P} = \{\mathbf{r} : r_k \geq 0, \sum_i r_k = 1\}$. If f is strictly convex, equality holds if and only if $\frac{1}{r_k}\boldsymbol{\tau}_k = \boldsymbol{\tau}$ is independent of k.

The proof follows Jensen's inequality,

$$f\big(\mathbb{E}[\boldsymbol{\tau}]\big) \leq \mathbb{E}\big[f(\boldsymbol{\tau})\big]. \tag{B.14}$$

Moreover, by adding a dummy variable $\boldsymbol{\tau}_0 = \mathbf{0}$, (B.13) becomes

$$f\left(\sum_k \boldsymbol{\tau}_k\right) = f\left(\mathbf{0} + \sum_k \boldsymbol{\tau}_k\right) \leq r_0 f\left(\mathbf{0}\right) + \sum_k r_k f\left(\frac{1}{r_k}\boldsymbol{\tau}_k\right), \tag{B.15}$$

where the constant $r_0 f\left(\mathbf{0}\right)$ is independent of $\boldsymbol{\tau}_k$'s and the constraint is relaxed as $\sum_k r_k \leq 1$.

The alternative surrogate function $g_{\text{sur}}(\mathbf{c} : \hat{\mathbf{c}})$ is convex over $\mathbf{c}$. Applying the convex decomposition lemma (Lemma B.2) yields

$$g^{\text{sur}}(\mathbf{c} : \hat{\mathbf{c}}) \leq \sum_j \sum_y \sum_E \sum_i \sum_x \left[\hat{p}_j(y, E)h(y|x)\mu_i(E)c_i(x) \right.$$
$$\left. + \hat{q}_j(y, E)r(x, i|y, E)\exp\left(-\frac{h(y|x)\mu_i(E)}{r(x, i|y, E)}\big(c_i(x) - \hat{c}_i(x)\big)\right)\right] + C, \tag{B.16}$$

for all $r(x, i|y, E) \geq 0$ such that

$$\sum_x \sum_i r(x, i|y, E) \leq 1 \quad \forall(y, E). \tag{B.17}$$

Note that minor extension of the convex decomposition lemma leads to a different C in the equation. For simplicity, we denote C as all constants that are independent of $\mathbf{c}$.

To derive a minimization algorithm, let

$$r(x, i|y, E) = \frac{h(y|x)\mu_i(E)}{z(i, x)},\tag{B.18}$$

where $z(i, x)$ is usually called the *auxiliary variable*. One choice of $z(i, x)$ that satisfy the constraint (B.17) is given by

$$z(i, x) = z_0 = \left(\max_y \sum_{x'} h(y|x')\right)\left(\max_E \sum_{i'} \mu_{i'}(E)\right).\tag{B.19}$$

The resulting decoupled surrogate function is

$$
\begin{aligned}
g(\mathbf{c}) &\leq g^{\mathrm{sur}}(\mathbf{c} : \hat{\mathbf{c}}) \\
&\leq \sum_j \sum_y \sum_E \sum_i \sum_x \Big[\hat{p}_j(y, E) h(y|x)\mu_i(E)c_i(x) \\
&\quad + \hat{q}_j(y, E)\frac{h(y|x)\mu_i(E)}{z(i, x)} \exp\Big(-z(i, x)\big(c_i(x) - \hat{c}_i(x)\big)\Big)\Big] + C \\
&= \sum_i \sum_x \Bigg[\Big(\sum_y h(y|x)\sum_j \sum_E \hat{p}_j(y, E)\mu_i(E)\Big) c_i(x) \\
&\quad + \frac{1}{z(i, x)}\Big(\sum_y h(y|x)\sum_j \sum_E \hat{q}_j(y, E)\mu_i(E)\Big) \exp\Big(-z(i, x)\big(c_i(x) - \hat{c}_i(x)\big)\Big)\Bigg] + C \\
&= \tilde{g}^{\mathrm{sur}}(\mathbf{c} : \hat{\mathbf{c}}),
\end{aligned}
\tag{B.20}
$$

The decoupled surrogate function $\tilde{g}^{\text{sur}}(\mathbf{c} : \hat{\mathbf{c}})$ is separable for each $c_i(x)$, i.e.,

$$\tilde{g}^{\text{sur}}(\mathbf{c} : \hat{\mathbf{c}}) = \sum_i \sum_x \tilde{g}_{i,x}^{\text{sur}}\left(c_i(x) : \hat{c}_i(x)\right) . \tag{B.21}$$

Each $\tilde{g}_{i,x}^{\text{sur}}$ can be minimized over $c_i(x)$ in closed form as

$$c_i(x) = \max\left(\hat{c}_i(x) - \frac{1}{z(i,x)} \ln \frac{\sum_y h(y|x) \sum_j \sum_E \hat{p}_j(y,E)\mu_i(E)}{\sum_y h(y|x) \sum_j \sum_E \hat{q}_j(y,E)\mu_i(E)}, \; 0 \right) . \tag{B.22}$$

In summary, at iteration k of the alternating minimization algorithm, the original objective function $g(\mathbf{c})$ is decomposed at the current estimate $\hat{\mathbf{c}}^{(k)}$ and the surrogate function $\tilde{g}_{\text{sur}}(\mathbf{c} : \hat{\mathbf{c}}^{(k)})$ is minimized in parallel to get the new estimate $\hat{\mathbf{c}}^{(k+1)}$.

The pseudo-code of the algorithm is shown below.

Algorithm 3: AM algorithm

Pre-compute $z(i,x) = \left(\max_y \sum_{x'} h(y|x') \right) \left(\max_E \sum_{i'} \mu_{i'}(E) \right) \ \forall (i,x)$

Initialize $\hat{c}_i^{(0)}(x)$

for $k = 0, 1, 2, \ldots$ **do**

    foreach $y,\ j,\ E$ **do**

        $\hat{q}_j^{(k)}(y, E) = I_{0,j}(y)\psi_j(y, E) \exp\left(-\sum_x h(y|x) \sum_i \mu_i(E) c_i^{(k)}(x) \right)$

        $\hat{p}_j^{(k)}(y, E) = d_j(y) \dfrac{\hat{q}_j^{(k)}(y, E)}{\sum_{E'} \hat{q}_j^{(k)}(y, E')}$

    end

    foreach $i,\ x$ **do**

        $\tilde{b}_i^{(k)}(x) = \sum_y h(y|x) \sum_j \sum_E \hat{p}_j^{(k)}(y, E)\mu_i(E)$

        $\hat{b}_i^{(k)}(x) = \sum_y h(y|x) \sum_j \sum_E \hat{q}_j^{(k)}(y, E)\mu_i(E)$

        $\hat{c}_i^{(k+1)}(x) = \max\left(\hat{c}_i^{(k)}(x) - \dfrac{1}{z(i,x)} \ln \dfrac{\tilde{b}_i^{(k)}(x)}{\hat{b}_i^{(k)}(x)},\ 0 \right)$

    end

end

B.2 Regularized AM algorithm

To trade off the image smoothness and data fitting, a spatial penalty function is employed in the objective function, which is formulated as

$$R(\mathbf{c}) = \sum_i \sum_x \sum_{x' \in \mathcal{N}(x)} w_{x,x'} \phi\big(c_i(x) - c_i(x') \big), \tag{B.23}$$

where $\mathcal{N}(x)$ is the neighborhood of x and $w_{x,x'}$ is the spatial weighting for pixel-pair (x, x'). $\phi(t)$ is a convex potential function that satisfies $\phi(t) = \phi(-t)$. The overall objective function

is given by

$$g^{\text{reg}}(\mathbf{c}) = g(\mathbf{c}) + \lambda R(\mathbf{c}). \tag{B.24}$$

In the regularization term, the $c_i(x)$'s are coupled and cannot be updated in parallel as in the unregularized AM algorithm. To derive the regularized AM algorithm, Lemma B.2 is used to decompose the penalty function as

$$
\begin{aligned}
R(\mathbf{c}) &= \sum_i \sum_x \sum_{x' \in \mathcal{N}(x)} w_{x,x'} \phi \left(\frac{2c_i(x) - \hat{c}_i(x) - \hat{c}_i(x')}{2} + \frac{-2c_i(x') + \hat{c}_i(x) + \hat{c}_i(x')}{2} \right) \\
&\leq \sum_i \sum_x \sum_{x' \in \mathcal{N}(x)} w_{x,x'} \left[\frac{1}{2}\phi \Big(2c_i(x) - \hat{c}_i(x) - \hat{c}_i(x') \Big) + \frac{1}{2}\phi \Big(-2c_i(x') + \hat{c}_i(x) + \hat{c}_i(x') \Big) \right] \\
&= \sum_i \sum_x \sum_{x' \in \mathcal{N}(x)} w_{x,x'} \left[\frac{1}{2}\phi \Big(2c_i(x) - \hat{c}_i(x) - \hat{c}_i(x') \Big) + \frac{1}{2}\phi \Big(2c_i(x') - \hat{c}_i(x) - \hat{c}_i(x') \Big) \right] \\
&= \sum_i \sum_x \sum_{x' \in \mathcal{N}(x)} w_{x,x'} \phi \Big(2c_i(x) - \hat{c}_i(x) - \hat{c}_i(x') \Big) \\
&= \tilde{R}(\mathbf{c} : \hat{\mathbf{c}}).
\end{aligned}
\tag{B.25}
$$

At each iteration, the algorithm alternatively minimizes the regularized surrogate function

$$\tilde{g}^{\text{sur, reg}}(\mathbf{c} : \hat{\mathbf{c}}^{(k)}) = \tilde{g}^{\text{sur}}(\mathbf{c} : \hat{\mathbf{c}}^{(k)}) + \lambda \tilde{R}(\mathbf{c} : \hat{\mathbf{c}}^{(k)}), \tag{B.26}$$

which is separable for each individual $c_i(x)$.

The pseudo-code of the regularized AM algorithm is shown below.

Algorithm 4: Regularized AM algorithm

Pre-compute $z(i,x) = \left(\max_y \sum_{x'} h(y|x') \right) \left(\max_E \sum_{i'} \mu_{i'}(E) \right) \ \forall (i,x)$

Initialize $\hat{c}_i^{(0)}(x)$

for $k = 0, 1, 2, \ldots$ **do**

    foreach $y, \ j, \ E$ **do**

        $\hat{q}_j^{(k)}(y, E) = I_{0,j}(y)\psi_j(y, E) \exp\left(-\sum_x h(y|x) \sum_i \mu_i(E)c_i^{(k)}(x) \right)$

        $\hat{p}_j^{(k)}(y, E) = d_j(y) \frac{\hat{q}_j^{(k)}(y,E)}{\sum_{E'} \hat{q}_j^{(k)}(y,E')}$

    end

    foreach $i, \ x$ **do**

        $\tilde{b}_i^{(k)}(x) = \sum_y h(y|x) \sum_j \sum_E \hat{p}_j^{(k)}(y, E)\mu_i(E)$

        $\hat{b}_i^{(k)}(x) = \sum_y h(y|x) \sum_j \sum_E \hat{q}_j^{(k)}(y, E)\mu_i(E)$

        $\hat{c}_i^{(k+1)}(x) = \underset{\tau \geq 0}{\operatorname{argmin}} \left[\tilde{b}_i^{(k)}(x)\left(\tau - \hat{c}_i^{(k)}(x) \right) + \frac{\hat{b}_i^{(k)}(x)}{z(i,x)} \exp\left(-z(i,x)\left(\tau - \hat{c}_i^{(k)}(x) \right) \right) \right.$

        $\left. + \lambda \sum_{x' \in \mathcal{N}(x)} w_{x,z}\phi\left(2\tau - \hat{c}_i^{(k)}(x) - \hat{c}_i^{(k)}(x') \right) \right]$

    end

end

B.3   Acceleration via ordered subsets

Subset methods [78–82] are range-based decomposition techniques that are widely used in CT image reconstruction to increase the convergence speed by using a subset of data in each sub-iteration.

In the ordered subset method, the data are partitioned into M balanced and disjoint subsets. At the m-th sub-iteration, only the data in the m-th subset are considered in the data-fitting term. One full iteration is composed of M sub-iterations in sequence in order to cover all the

data. The acceleration rate is approximately proportional to the number of subsets when it's relatively far away from the optimal point. However, there is no converge guarantee.

Empirically, we dynamically changed the number of subsets in each iteration. A larger number of subsets is used in early iterations to provide faster decrease of the objective function, while in later iterations, the number of subsets is reduced as the iterations proceed and finally drops down to 1 in order to get close to the optimal point.

Denote the full data space by $\mathcal{Y}$. Let $\mathcal{Y}_{m/M}$ be the m-th subset in the M-subsets partition, where $\mathcal{Y} = \bigcup_{m=1}^{M} \mathcal{Y}_{m/M}$ and $\mathcal{Y}_{m/M} \cap \mathcal{Y}_{m'/M} = \emptyset$ if $m \neq m'$.

The pseudo code of the regularized AM algorithm with ordered subsets is shown below.

Algorithm 5: Regularized AM algorithm with ordered subsets

Pre-compute $z(i,x) = \left(\max_y \sum_{x'} h(y|x') \right) \left(\max_E \sum_{i'} \mu_{i'}(E) \right) \; \forall (i,x)$

Select $\{M_k\}_{k=0,1,2,\dots}$ as the number of subsets for each iteration.

Initialize $\hat{c}_i^{(0,0)}(x)$

for $k = 0, 1, 2, \dots$ **do**

    for $m = 0, 1, 2, \dots, (M_k - 1)$ **do**

        foreach $y \in \mathcal{Y}_{m/M_k}$, j, E **do**

$$\hat{q}_j^{(k,m)}(y,E) = I_{0,j}(y)\psi_j(y,E)\exp\left(-\sum_x h(y|x)\sum_i \mu_i(E)\hat{c}_i^{(k,m)}(x) \right)$$

$$\hat{p}_j^{(k,m)}(y,E) = d_j(y)\frac{\hat{q}_j^{(k,m)}(y,E)}{\sum_{E'}\hat{q}_j^{(k,m)}(y,E')}$$

        end

        foreach i, x **do**

$$\tilde{b}_i^{(k,m)}(x) = \sum_{y\in\mathcal{Y}_{m/M_k}} h(y|x)\sum_j\sum_E \hat{p}_j^{(k,m)}(y,E)\mu_i(E)$$

$$\hat{b}_i^{(k,m)}(x) = \sum_{y\in\mathcal{Y}_{m/M_k}} h(y|x)\sum_j\sum_E \hat{q}_j^{(k,m)}(y,E)\mu_i(E)$$

$$\hat{c}_i^{(k,m+1)}(x) =$$

$$\operatorname*{argmin}_{\tau\geq 0}\left[\tilde{b}_i^{(k,m)}(x)\left(\tau - \hat{c}_i^{(k,m)}(x)\right) + \frac{\hat{b}_i^{(k,m)}(x)}{z(i,x)}\exp\left(-z(i,x)\left(\tau - \hat{c}_i^{(k,m)}(x)\right)\right)\right.$$

$$\left. + \frac{\lambda}{M_k}\sum_{x\in\mathcal{N}(x)} w_{x,x'}\phi\left(2\tau - \hat{c}_i^{(k,m)}(x) - \hat{c}_i^{(k,m)}(x')\right)\right]$$

        end

    end

    foreach i, x **do**

$$\hat{c}_i^{(k+1,0)}(x) = \hat{c}_i^{(k,M_k)}(x)$$

    end

end

Bibliography

[1] J. E. Munzenrider and N. J. Liebsch, "Proton therapy for tumors of the skull base," *Strahlentherapie und Onkologie*, vol. 175, no. 2, pp. 57–63, 1999.

[2] A. J. Lomax, T. Boehringer, A. Coray, E. Egger, G. Goitein, M. Grossmann, P. Juelke, S. Lin, E. Pedroni, B. Rohrer, W. Roser, B. Rossi, B. Siegenthaler, O. Stadelmann, H. Stauble, C. Vetter, and L. Wisser, "Intensity modulated proton therapy: A clinical example," *Med Phys*, vol. 28, no. 3, pp. 317–324, 2001.

[3] J. D. Slater, C. J. Rossi, L. T. Yonemoto, D. A. Bush, B. R. Jabola, R. P. Levy, R. I. Grove, W. Preston, and J. M. Slater, "Proton therapy for prostate cancer: The initial Loma Linda University experience," *Int J Rad Oncol Biol*, vol. 59, no. 2, pp. 348–352, 2004.

[4] J. Y. Chang, X. Zhang, X. Wang, Y. Kang, B. Riley, S. Bilton, R. Mohan, R. Komaki, and J. D. Cox, "Significant reduction of normal tissue dose by proton radiotherapy compared with three-dimensional conformal or intensity-modulated radiation therapy in stage I or stage III non-small-cell lung cancer," *Int J Rad Oncol Biol*, vol. 65, no. 4, pp. 1087–1096, 2006.

[5] J.-M. Li, J.-M. Yu, S.-W. Liu, Q. Chen, X.-K. Mu, Q.-A. Jiang, M.-H. Zhao, and J.-H. Zhang, "Dose distributions of proton beam therapy for hepatocellular carcinoma: A comparative study of treatment planning with 3D-conformal radiation therapy or intensity-modulated radiation therapy," *Zhonghua Yi Xue Za Zhi*, vol. 89, no. 45, pp. 3201–3206, 2009.

[6] R. C. Nichols, S. N. Huh, R. H. Henderson, N. P. Mendenhall, S. Flampouri, Z. Li, H. J. D'Agostino, J. D. Cury, D. C. Pham, and B. S. Hoppe, "Proton radiation therapy offers reduced normal lung and bone marrow exposure for patients receiving dose-escalated radiation therapy for unresectable stage III non-small-cell lung cancer: A dosimetric study," *Clin Lung Cancer*, vol. 12, no. 4, pp. 252–257, 2011.

[7] N. P. Brodin, P. Munck af Rosenschöld, M. Blomstrand, A. Kiil-Berthlesen, C. Hollensen, I. R. Vogelius, B. Lannering, S. M. Bentzen, and T. Björk-Eriksson, "Hippocampal sparing radiotherapy for pediatric medulloblastoma: Impact of treatment margins and treatment technique," *Neuro-Oncol*, vol. 16, no. 4, pp. 594–602, 2014.

[8] M. F. Moyers, D. W. Miller, D. A. Bush, and D. J. Slater, "Methodologies and tools for proton beam design for lung tumors," *Int J Rad Oncol Biol*, vol. 49, no. 5, pp. 1429–1438, 2001.

[9] H. Paganetti, "Range uncertainties in proton therapy and the role of Monte Carlo simulations," *Phys Med Biol*, vol. 57, no. 11, pp. R99–R117, 2012.

[10] P. C. Park, X. R. Zhu, A. K. Lee, N. Sahoo, A. D. Melancon, L. Zhang, and L. Dong, "A beam-specific planning target volume (PTV) design for proton therapy to account for setup and range uncertainties," *Int J Rad Oncol Biol*, vol. 82, no. 2, pp. e329–336, 2012.

[11] M. Yang, G. Virshup, J. E. Clayton, X. R. Zhu, R. Mohan, and L. Dong, "Theoretical variance analysis of single- and dual-energy computed tomography methods for calculating proton stopping power ratios of biological tissues," *Phys Med Biol*, vol. 55, no. 5, pp. 1343–1362, 2010.

[12] M. Yang, X. R. Zhu, P. C. Park, U. Titt, R. Mohan, G. Virshup, J. E. Clayton, and L. Dong, "Comprehensive analysis of proton range uncertainties related to patient stopping-power-ratio estimation using the stoichiometric calibration," *Phys Med Biol*, vol. 57, no. 13, pp. 4095–4115, 2012.

[13] E. Bär, A. Lalonde, G. Royle, H.-M. Lu, and H. Bouchard, "The potential of dual-energy CT to reduce proton beam range uncertainties," *Med Phys*, vol. 44, no. 6, pp. 2332–2344, 2017.

[14] N. Hünemohr, H. Paganetti, S. Greilich, O. Jäkel, and J. Seco, "Tissue decomposition from dual energy CT data for MC based dose calculation in particle therapy," *Med Phys*, vol. 41, no. 6, p. 061714, 2014.

[15] A. E. Bourque, J.-F. Carrier, and H. Bouchard, "A stoichiometric calibration method for dual energy computed tomography," *Phys Med Biol*, vol. 59, no. 8, pp. 2059–2088, 2014.

[16] J.-É. Tremblay, S. Bedwani, and H. Bouchard, "A theoretical comparison of tissue parameter extraction methods for dual energy computed tomography: Comparison of tissue parameter extraction methods for DECT," *Med Phys*, vol. 41, no. 8, p. 081905, 2014.

[17] J. K. van Abbema, M.-J. van Goethem, M. J. W. Greuter, A. van der Schaaf, S. Brandenburg, and E. R. van der Graaf, "Relative electron density determination using a physics based parameterization of photon interactions in medical DECT," *Phys Med Biol*, vol. 60, no. 9, pp. 3825–3846, 2015.

[18] L. I. R. Garcia, J. F. P. Azorin, and J. F. Almansa, "A new method to measure electron density and effective atomic number using dual-energy CT images," *Phys Med Biol*, vol. 61, no. 1, pp. 265–279, 2016.

[19] A. Lalonde and H. Bouchard, "A general method to derive tissue parameters for Monte Carlo dose calculation with multi-energy CT," *Phys Med Biol*, vol. 61, no. 22, pp. 8044–8069, 2016.

[20] M. Saito and S. Sagara, "Simplified derivation of stopping power ratio in the human body from dual-energy CT data," *Med Phys*, vol. 44, no. 8, pp. 4179–4187, 2017.

[21] B. Li, H. C. Lee, X. Duan, C. Shen, L. Zhou, X. Jia, and M. Yang, "Comprehensive analysis of proton range uncertainties related to stopping-power-ratio estimation using dual-energy CT imaging," *Phys Med Biol*, vol. 62, no. 17, pp. 7056–7074, 2017.

[22] N. Kanematsu, T. Inaniwa, and Y. Koba, "Relationship between electron density and effective densities of body tissues for stopping, scattering, and nuclear interactions of proton and ion beams," *Med Phys*, vol. 39, no. 2, pp. 1016–1020, 2012.

[23] P. Farace, "Experimental verification of ion stopping power prediction from dual energy CT data in tissue surrogates," *Phys Med Biol*, vol. 59, no. 22, pp. 7081–7084, 2014.

[24] V. T. Taasti, J. B. B. Petersen, L. P. Muren, J. Thygesen, and D. C. Hansen, "A robust empirical parametrization of proton stopping power using dual energy CT," *Med Phys*, vol. 43, no. 10, pp. 5547–5560, 2016.

[25] G. Vilches-Freixas, V. T. Taasti, L. P. Muren, J. B. B. Petersen, J. M. Létang, D. C. Hansen, and S. Rit, "Comparison of projection- and image-based methods for proton stopping power estimation using dual energy CT," *Phys Imaging Radiat Oncol*, vol. 3, pp. 28–36, 2017.

[26] M. Saito, "Potential of dual-energy subtraction for converting CT numbers to electron density based on a single linear relationship," *Med Phys*, vol. 39, no. 4, pp. 2021–2030, 2012.

[27] R. A. Brooks and G. D. Chiro, "Beam hardening in x-ray reconstructive tomography," *Phys Med Biol*, vol. 21, no. 3, pp. 390–398, 1976.

[28] W. D. McDavid, R. G. Waggener, W. H. Payne, and M. J. Dennis, "Correction for spectral artifacts in cross-sectional reconstruction from X rays," *Med Phys*, vol. 4, no. 1, pp. 54–57, 1977.

[29] G. T. Herman, "Correction for beam hardening in computed tomography," *Phys Med Biol*, vol. 24, no. 1, pp. 81–106, 1979.

[30] G. T. Herman and S. S. Trivedi, "A comparative study of two postreconstruction beam hardening correction methods," *IEEE Trans Med Imag*, vol. 2, no. 3, pp. 128–135, 1983.

[31] P. M. Joseph and R. D. Spital, "A method for correcting bone induced artifacts in computed tomography scanners," *J Comput Assist Tomogr*, vol. 2, no. 1, pp. 100–108, 1978.

[32] P. M. Joseph and C. Ruth, "A method for simultaneous correction of spectrum hardening artifacts in CT images containing both bone and iodine," *Med Phys*, vol. 24, no. 10, pp. 1629–1634, 1997.

[33] J. Hsieh, R. C. Molthen, C. A. Dawson, and R. H. Johnson, "An iterative approach to the beam hardening correction in cone beam CT," *Med Phys*, vol. 27, no. 1, pp. 23–29, 2000.

[34] L. Fu, T.-C. Lee, S. M. Kim, A. M. Alessio, P. E. Kinahan, Z. Chang, K. Sauer, M. K. Kalra, and B. De Man, "Comparison between pre-log and post-log statistical models in ultra-low-dose CT reconstruction," *IEEE Trans Med Imag*, vol. 36, no. 3, pp. 707–720, 2017.

[35] B. R. Whiting, "Signal statistics in x-ray computed tomography," in *Medical Imaging 2002: Physics of Medical Imaging*.   San Diego, CA: SPIE, 2002, vol. 4682, pp. 53–61.

[36] G. M. Lasio, B. R. Whiting, and J. F. Williamson, "Statistical reconstruction for x-ray computed tomography using energy-integrating detectors," *Phys Med Biol*, vol. 52, no. 8, pp. 2247–2266, 2007.

[37] K. Lange and R. Carson, "EM reconstruction algorithms for emission and transmission tomography," *J Comput Assist Tomogr*, vol. 8, no. 2, pp. 306–316, 1984.

[38] H. Erdoğan and J. A. Fessler, "Monotonic algorithms for transmission tomography," *IEEE Trans Med Imag*, vol. 18, no. 9, pp. 801–814, 1999.

[39] B. De Man, J. Nuyts, P. Dupont, G. Marchal, and P. Suetens, "An iterative maximum-likelihood polychromatic algorithm for CT," *IEEE Trans Med Imag*, vol. 20, no. 10, pp. 999–1008, 2001.

[40] I. A. Elbakri and J. A. Fessler, "Statistical image reconstruction for polyenergetic x-ray computed tomography," *IEEE Trans Med Imag*, vol. 21, no. 2, pp. 89–99, 2002.

[41] J. A. O'Sullivan, J. Benac, and J. F. Williamson, "Alternating minimization algorithm for dual energy x-ray CT," in *IEEE Int Symp Biomed Imaging*.   Arlington, VA: IEEE, 2004, pp. 579–582.

[42] J. A. O'Sullivan and J. Benac, "Alternating minimization algorithms for transmission tomography," *IEEE Trans Med Imag*, vol. 26, no. 3, pp. 283–297, 2007.

[43] K. Sauer and C. Bouman, "A local update strategy for iterative reconstruction from projections," *IEEE Trans Signal Process*, vol. 41, no. 2, pp. 534–548, 1993.

[44] B. De Man, S. Basu, J. B. Thibault, J. Hsieh, J. A. Fessier, C. Bouman, and K. Sauer, "A study of four minimization approaches for iterative reconstruction in x-ray CT," in *IEEE Nucl Sci Symp Conf Rec*, vol. 5, 2005, pp. 2708–2710.

[45] J. Wang, T. Li, H. Lu, and Z. Liang, "Penalized weighted least-squares approach to sinogram noise reduction and image reconstruction for low-dose x-ray computed tomography," *IEEE Trans Med Imag*, vol. 25, no. 10, pp. 1272–1283, 2006.

[46] Z. Yu, J. B. Thibault, C. A. Bouman, K. D. Sauer, and J. Hsieh, "Fast Model-Based X-Ray CT Reconstruction Using Spatially Nonhomogeneous ICD Optimization," *IEEE Trans Imag Process*, vol. 20, no. 1, pp. 161–175, 2011.

[47] J. Fornaro, S. Leschka, D. Hibbeln, A. Butler, N. Anderson, G. Pache, H. Scheffel, S. Wildermuth, H. Alkadhi, and P. Stolzmann, "Dual-and multi-energy CT: approach to functional imaging," *Insights Imaging*, vol. 2, no. 2, pp. 149–159, 2011.

[48] C. H. McCollough, S. Leng, L. Yu, and J. G. Fletcher, "Dual-and multi-energy CT: principles, technical approaches, and clinical applications," *Radiology*, vol. 276, no. 3, pp. 637–653, 2015.

[49] U. Schneider, E. Pedroni, and A. Lomax, "The calibration of CT Hounsfield units for radiotherapy treatment planning," *Phys Med Biol*, vol. 41, no. 1, pp. 111–124, 1996.

[50] R. A. Rutherford, B. R. Pullan, and I. Isherwood, "Measurement of effective atomic number and electron density using an EMI scanner," *Neuroradiology*, vol. 11, no. 1, pp. 15–21, 1976.

[51] H. Bethe, "Zur theorie des durchgangs schneller korpuskularstrahlen durch materie," *Ann Phys (Berlin)*, vol. 397, no. 3, pp. 325–400, 1930.

[52] D. Han, J. V. Siebers, and J. F. Williamson, "A linear, separable two-parameter model for dual energy CT imaging of proton stopping power computation," *Med Phys*, vol. 43, no. 1, pp. 600–612, 2016.

[53] ICRU, "Stopping powers for electrons and positrons," International Commission on Radiation Units and Measurements, Bethesda, MD, ICRU Report 37, 1984.

[54] M. Berger, J. Hubbell, S. Seltzer, J. Chang, J. Coursey, R. Sukumar, D. Zucker, and K. Olsen, "XCOM: Photon cross section database (version 1.5)," National Institute of Standards and Technology, Gaithersburg, MD, NIST Standard Reference Database 8, 2010.

[55] F. W. Spiers, "Effective atomic number and energy absorption in tissues," *Br J Radiol*, vol. 19, no. 218, pp. 52–63, 1946.

[56] R. E. Alvarez and A. Macovski, "Energy-selective reconstructions in x-ray computerised tomography," *Phys Med Biol*, vol. 21, no. 5, pp. 733–744, 1976.

[57] M. Torikoshi, T. Tsunoo, M. Sasaki, M. Endo, Y. Noda, Y. Ohno, T. Kohno, K. Hyodo, K. Uesugi, and N. Yagi, "Electron density measurement with dual-energy x-ray CT using synchrotron radiation," *Phys Med Biol*, vol. 48, no. 5, pp. 673–685, 2003.

[58] W. Mayneord, "The significance of the roentgen," *Acta Int Union Against Cancer*, vol. 2, p. 271, 1937.

[59] D. Han, "Advances in dual-energy computed tomography imaging of radiological properties," Ph.D. dissertation, Virginia Commonwealth University, 2018.

[60] J. P. Schlomka, E. Roessl, R. Dorscheid, S. Dill, G. Martens, T. Istel, C. Bäumer, C. Herrmann, R. Steadman, G. Zeitler, A. Livne, and R. Proksa, "Experimental feasibility of multi-energy photon-counting K-edge imaging in pre-clinical computed tomography," *Phys Med Biol*, vol. 53, no. 15, pp. 4031–4047, 2008.

[61] W. Huh and J. A. Fessler, "Iterative image reconstruction for dual-energy x-ray CT using regularized material sinogram estimates," in *IEEE Int Symp Biomed Imaging*. Chicago, IL: IEEE, 2011, pp. 1512–1515.

[62] C. O. Schirra, E. Roessl, T. Koehler, B. Brendel, A. Thran, D. Pan, M. A. Anastasio, and R. Proksa, "Statistical reconstruction of material decomposed data in spectral CT," *IEEE Trans Med Imag*, vol. 32, no. 7, pp. 1249–1257, 2013.

[63] G. Vilches-Freixas, J. M. Létang, N. Ducros, and S. Rit, "Optimization of dual-energy CT acquisitions for proton therapy using projection-based decomposition," *Med Phys*, vol. 44, no. 9, pp. 4548–4558, 2017.

[64] L. A. Lehmann, R. E. Alvarez, A. Macovski, W. R. Brody, N. J. Pelc, S. J. Riederer, and A. L. Hall, "Generalized image combinations in dual KVP digital radiography," *Med Phys*, vol. 8, no. 5, pp. 659–667, 1981.

[65] K.-S. Chuang and H. K. Huang, "Comparison of four dual energy image decomposition methods," *Phys Med Biol*, vol. 33, no. 4, pp. 455–466, 1988.

[66] C. H. Yan, R. T. Whalen, G. S. Beaupré, S. Y. Yen, and S. Napel, "Reconstruction algorithm for polychromatic CT imaging: Application to beam hardening correction," *IEEE Trans Med Imag*, vol. 19, no. 1, pp. 1–11, 2000.

[67] B. Heismann and M. Balda, "Quantitative image-based spectral reconstruction for computed tomography," *Med Phys*, vol. 36, no. 10, pp. 4471–4485, 2009.

[68] V. I. Ivakhnenko, "A novel quasi-linearization method for CT image reconstruction in scanners with a multi-energy detector system," *IEEE Trans Nucl Sci*, vol. 57, no. 2, pp. 870–879, 2010.

[69] P. Sukovic and N. H. Clinthorne, "Penalized weighted least-squares image reconstruction for dual energy x-ray transmission tomography," *IEEE Trans Med Imag*, vol. 19, no. 11, pp. 1075–1081, 2000.

[70] W. Huh, J. A. Fessler, A. M. Alessio, and P. E. Kinahan, "Fast kVp-switching dual energy CT for PET attenuation correction," in *IEEE Nucl Sci Symp Conf Rec*. Orlando, FL: IEEE, 2009, pp. 2510–2515.

[71] N. Hünemohr, B. Krauss, C. Tremmel, B. Ackermann, O. Jäkel, and S. Greilich, "Experimental verification of ion stopping power prediction from dual energy CT data in tissue surrogates," *Phys Med Biol*, vol. 59, no. 1, pp. 83–96, 2014.

[72] D. Han, M. A. Porras-Chaverri, J. A. O'Sullivan, D. G. Politte, and J. F. Williamson, "On the accuracy of parametric two-parameter photon cross-section models in dual-energy CT applications," *Med Phys*, vol. 44, no. 6, pp. 2438–2446, 2017.

[73] J. F. Williamson, S. Li, S. Devic, B. R. Whiting, and F. A. Lerma, "On two-parameter models of photon cross sections: Application to dual-energy CT imaging," *Med Phys*, vol. 33, no. 11, pp. 4115–4129, 2006.

[74] J. D. Evans, B. R. Whiting, D. G. Politte, J. A. O'Sullivan, P. F. Klahr, and J. F. Williamson, "Experimental implementation of a polyenergetic statistical reconstruction algorithm for a commercial fan-beam CT scanner," *Physica Medica*, vol. 29, no. 5, pp. 500–512, 2013.

[75] I. Csiszár, "Why least squares and maximum entropy? An axiomatic approach to inference for linear inverse problems," *Ann Stat*, vol. 19, no. 4, pp. 2032–2066, 1991.

[76] R. Stevenson and E. Delp, "Fitting curves with discontinuities," in *the First International Workshop on Robust Computer Vision*, 1990, pp. 127–136.

[77] Y. Chen, "Alternating minimization algorithms for dual-energy x-ray CT imaging and information optimization," Ph.D. dissertation, Washington University in St. Louis, 2014.

[78] H. M. Hudson and R. S. Larkin, "Accelerated image reconstruction using ordered subsets of projection data," *IEEE Trans Med Imag*, vol. 13, no. 4, pp. 601–609, 1994.

[79] H. Erdogan and J. A. Fessler, "Ordered subsets algorithms for transmission tomography," *Phys Med Biol*, vol. 44, no. 11, pp. 2835–2851, 1999.

[80] S. Ahn, J. F. Fessler, D. Blatt, and A. O. Hero, "Convergent incremental optimization transfer algorithms: Application to tomography," *IEEE Trans Med Imag*, vol. 25, no. 3, pp. 283–296, 2006.

[81] S. Degirmenci, D. G. Politte, C. Bosch, N. Tricha, and J. A. O'Sullivan, "Acceleration of iterative image reconstruction for x-ray imaging for security applications," in *Computational Imaging XIII*. San Francisco, CA: SPIE, 2015, vol. 9401, p. 94010C.

[82] S. Degirmenci, "A general framework of large-scale convex optimization using Jensen surrogates and acceleration techniques," Ph.D. dissertation, Washington University in St. Louis, 2016.

[83] Y. Nesterov, "A method for unconstrained convex minimization problem with the rate of convergence O$(1/k^2)$," in *Doklady AN USSR*, vol. 269, 1983, pp. 543–547.

[84] S. Boyd and L. Vandenberghe, "Convex optimization." New York, NY: Cambridge University Press, 2004, pp. 463–466.

[85] S. Zhang, D. Han, D. G. Politte, J. F. Williamson, and J. A. O'Sullivan, "Impact of joint statistical dual-energy CT reconstruction of proton stopping power images: Comparison to image- and sinogram-domain material decomposition approaches," *Med Phys*, vol. 45, no. 5, pp. 2129–2142, 2018.

[86] R. Birch and M. Marshall, "Computation of bremsstrahlung x-ray spectra and comparison with spectra measured with a Ge(Li) detector," *Phys Med Biol*, vol. 24, no. 3, pp. 505–517, 1979.

[87] E. Bär, A. Lalonde, R. Zhang, K.-W. Jee, K. Yang, G. Sharp, B. Liu, G. Royle, H. Bouchard, and H.-M. Lu, "Experimental validation of two dual-energy CT methods for proton therapy using heterogeneous tissue samples," *Med Phys*, vol. 45, no. 1, pp. 48–59, 2018.

[88] ICRU, "Photon, electron, proton, and neutron interaction data for body tissues," International Commission on Radiation Units and Measurements, Bethesda, MD, ICRU Report 46, 1992.

[89] M. Cristy, "Active bone marrow distribution as a function of age in humans," *Phys Med Biol*, vol. 26, no. 3, pp. 389–400, 1981.

[90] M. Y. Dju, K. E. Mason, and L. J. Filer, "Vitamin E (tocopherol) in human tissues from birth to old age," *Am J Clin Nutr*, vol. 6, no. 1, pp. 50–60, 1958.

[91] H. Q. Woodard and D. R. White, "The composition of body tissues," *Br J Radiol*, vol. 59, no. 708, pp. 1209–1218, 1986.

[92] D. R. White, H. Q. Woodard, and S. M. Hammond, "Average soft-tissue and bone models for use in radiation dosimetry," *Br J Radiol*, vol. 60, no. 717, pp. 907–913, 1987.

[93] ICRU, "Tissue substitutes in radiation dosimetry and measurement," International Commission on Radiation Units and Measurements, Bethesda, MD, ICRU Report 44, 1989.

[94] J. D. Evans, D. G. Politte, B. R. Whiting, J. A. O'Sullivan, and J. F. Williamson, "Noise-resolution tradeoffs in x-ray CT imaging: A comparison of penalized alternating minimization and filtered backprojection algorithms," *Med Phys*, vol. 38, no. 3, pp. 1444–1458, 2011.

[95] ICRP, "Adult reference computational phantoms. ICRP publication 110," *Ann ICRP*, vol. 39, no. 2, 2009.

[96] M. Yang, G. Virshup, J. E. Clayton, X. R. Zhu, R. Mohan, and L. Dong, "Does kV–MV dual-energy computed tomography have an advantage in determining proton stopping power ratios in patients?" *Phys Med Biol*, vol. 56, no. 14, pp. 4499–4515, 2011.

[97] Y. Chen, J. A. O'Sullivan, D. G. Politte, J. D. Evans, D. Han, B. R. Whiting, and J. F. Williamson, "Line integral alternating minimization algorithm for dual-energy x-ray CT image reconstruction," *IEEE Trans Med Imag*, vol. 35, no. 2, pp. 685–698, 2016.

[98] G. Matscheko and R. Ribberfors, "A Compton scattering spectrometer for determining x-ray photon energy spectra," *Phys Med Biol*, vol. 32, no. 5, pp. 577–594, 1987.

[99] M. Bhat, J. Pattison, G. Bibbo, and M. Caon, "Diagnostic x-ray spectra: A comparison of spectra generated by different computational methods with a measured spectrum," *Med Phys*, vol. 25, no. 1, pp. 114–120, 1998.

[100] S. Miyajima, "Thin CdTe detector in diagnostic x-ray spectroscopy," *Med Phys*, vol. 30, no. 5, pp. 771–777, 2003.

[101] J. M. Boone, "Equivalent spectra as a measure of beam quality," *Med Phys*, vol. 13, no. 6, pp. 861–868, 1986.

[102] ——, "The three parameter equivalent spectra as an index of beam quality," *Med Phys*, vol. 15, no. 3, pp. 304–310, 1988.

[103] M. R. Ay, S. Sarkar, M. Shahriari, D. Sardari, and H. Zaidi, "Assessment of different computational models for generation of x-ray spectra in diagnostic radiology and mammography: Comparison of x-ray spectra prediction models," *Med Phys*, vol. 32, no. 6, pp. 1660–1675, 2005.

[104] I. P. Almeida, L. E. J. R. Schyns, M. C. Öllers, W. van Elmpt, K. Parodi, G. Landry, and F. Verhaegen, "Dual-energy CT quantitative imaging: A comparison study between twin-beam and dual-source CT scanners," *Med Phys*, vol. 44, no. 1, pp. 171–179, 2017.

[105] B. N. Taylor and C. E. Kuyatt, "Guidelines for evaluating and expressing the uncertainty of NIST measurement results," U.S. Government Printing Office, Washington, DC, NIST Technical Note 1297, 1994.

[106] JCGM, "Evaluation of measurement data: Guide for the expression of uncertainty in measurement," BIPM Joint Committee for Guides in Metrology, Paris, JCGM 100, 2008.

Vita

Shuangyue Zhang

Degrees

Ph.D.   Electrical Engineering, Washington University in St. Louis, Missouri, U.S., December 2018

M.S.   Electrical Engineering, Washington University in St. Louis, Missouri, U.S., December 2018

M.S.   Control Science and Engineering, Tsinghua University, Beijing, China, July 2014

B.S.   Automation, Tsinghua University, Beijing, China, July 2011

Publications

<u>Journal Publications:</u>

S. Zhang, D. Han, J. F. Williamson, T. Zhao, D. G. Politte, B. R. Whiting, and J. A. O'Sullivan, "Experimental implementation of a joint statistical image reconstruction method for proton stopping power mapping from dual-energy CT data," to appear in *Medical Physics*.

S. Zhang, R. Liu, T. Zhao, "Mapping radiation distribution on ground based on the measurement using an unmanned aerial vehicle," *Journal of Environmental Radioactivity*, vol. 193, pp. 44–56, 2018.

S. Zhang, D. Han, D. G. Politte, J. F. Williamson, and J. A. O'Sullivan, "Impact of joint statistical dual-energy CT reconstruction of proton stopping power images: Comparison to image- and sinogram-domain material decomposition approaches," *Medical Physics*, vol. 45, no. 5, pp. 2129–2142, 2018.

S. Zhang, S. Li, H. Wang, S. Yang, "Study on chain-based BIST architecture of LUTs in FPGA," *Computer Science (China)*, vol. 41, no. 5, pp. 37–40, 2014.

S. Zhang, H. Wang, S. Yang, X. Hu, "Contradiction in service mapping of IEC61850 and its solutions," *Electric Power Automation Equipment (China)*, vol. 33, no. 3, pp. 141–146, 2013.

Conference Publications:

D. Han, **S. Zhang**, P. Klahr, B. R. Whiting, J. F. Williamson, and J. A. O'Sullivan, "On deriving x-ray CT spectra from beam hardening correction polynomials," presented at *the 60th AAPM annual meeting*, Nashville, TN, 2018.

Y. Hao, D. Han, **S. Zhang**, R. Liu, B. Sun, T. Zhang, and T. Zhao, "Dual-energy computed tomography for breast patient with implants," presented at *the 60th AAPM annual meeting*, Nashville, TN, 2018.

S. Zhang, D. Han, D. G. Politte, J. F. Williamson, and J. A. O'Sullivan, "Comparison of integrated and post-reconstruction dual-energy CT proton stopping power ratio estimation approaches," presented at *the 59th AAPM annual meeting*, Denver, CO, 2017.

S. Zhang, D. Han, D. G. Politte, M. A. Porras-Chaverri, B. R. Whiting, J. F. Williamson, and J. A. O'Sullivan, "Basis vector model based method for proton stopping power estimation from experimental dual energy CT data," presented at *the 58th AAPM annual meeting*, Washington, D.C., 2016.

S. Zhang, F. Lin, C.-K. Hsu, K.-T. Cheng, H. Wang, "Joint virtual probe: Joint exploration of multiple test items' spatial patterns for efficient silicon characterization and test prediction," in *the Conference on Design, Automation, and Test in Europe (DATE)*, Dresden, Germany, 2014.

Awards

Imaging Science Pathway Graduate Student Fellowship, Division of Biology and Biomedical Sciences (DBBS), Washington University in St. Louis, 2015-2017

Donald F. Wann Fellowship, Preston M. Green Department of Electrical and Systems Engineering, Washington University in St. Louis, 2015

December 2018